

**Ice Sublimation During Star and Planet Formation:
A Laboratory Characterization of CO and N₂ Binding Energies**

Jodi S. Balfé

Supervised by Prof. Karin I. Öberg

A thesis presented to the Department of Astronomy
in partial fulfillment of the requirements for the degree of Bachelor of Arts

Harvard College
April 11, 2015

Abstract

Millimeter observations show that abundances of gaseous molecular tracers CO and N₂H⁺ anti-correlate with each other, implying a process of relative chemical differentiation. These molecules have been applied to probe a wide range of astrophysical contexts, but their utility depends on understanding their chemical behavior. In turn, the distribution and evolution of molecules critically hinges on their sublimation processes. The anti-correlation can be reproduced by current astrochemical models only by assuming that the ratio of the binding energies, the kinetic parameter that constrains relative desorption behavior, between N₂ and CO is approximately $R_B = E_{B,N_2}(N_2 - N_2)/E_{B,CO}(CO - CO) = 0.60$. However, previous laboratory studies have shown that the difference between the CO and N₂ binding energies is small, with a binding energy ratio lower bound of 0.936 ± 0.03 , contradicting modeling assumptions. A proposed explanation for this discrepancy is that the H₂O present in interstellar ices affects the relative desorption of CO and N₂H⁺, contributing to a lower binding energy ratio in astrophysical contexts. To assess this possibility, we present Temperature Programmed Desorption (TPD) experiments of CO and N₂ ices in pure, layered, and mixed morphologies over a range of surface coverages and H₂O substrate structures. To understand the experimental data, we construct a four-phase kinetic model consisting of zeroth-order multilayer desorption and first-order monolayer desorption. The values of the binding energies are then extracted from the generative model via Markov Chain Monte Carlo (MCMC) fitting algorithms. We find that the the binding energy ratio, defined as $R_B = E_{B,N_2}(N_2 - H_2O)/E_{B,CO}(CO - H_2O)$ ranges from 0.758 ± 0.027 to 0.964 ± 0.035 . The lowest binding energy ratio was observed in a sub-monolayer mixed ice environment deposited on a highly porous amorphous H₂O substrate. This implies that the sublimation processes of CO and N₂ are different in astrophysically relevant conditions; importantly, in star and planet forming regions.

Acknowledgements

I would like to thank my advisor, Professor Karin I. Öberg, for all of her tremendous mentorship and support for both my Junior and Senior Theses at Harvard. She has provided critical guidance as I start scientific research, and has taught me so much more than astrochemistry. I would also like to thank Professor Edo Berger for mentoring me as my undergraduate academic advisor at Harvard, and Professor Charles Alcock for supervising the Undergraduate Senior Thesis Tutorial. Furthermore, I would also like to thank all of the members of the Öberg Astrochemistry Group, who provided numerous comments and discussions throughout the research process. Special thank you to Ian Czekala and Ana-Maria Piso for teaching me about computer modeling. Additionally, thank you to Dr. Edith Fayolle, Dr. Mahesh Rajappan, and Jennifer Bergner for teaching me about astrochemistry laboratory experimentation and for providing advice which greatly improved the quality of this thesis. Thank you to the Department of Astronomy and the Harvard-Smithsonian Center for Astrophysics for providing so many opportunities to learn and research. Lastly, thank you to my parents, family, and friends for their infinite support and love throughout my undergraduate time at Harvard.

Contents

1	Introduction	4
1.1	Ice Sublimation in Protoplanetary Disk Chemistry	4
1.2	Molecular Probes of Young Stellar and Planetary Systems	6
1.2.1	Prestellar Cores	7
1.2.2	Protostellar Cores	8
1.2.3	Protoplanetary Disks	10
1.3	The Role of CO and N ₂ as Molecular Probes	10
1.3.1	Interrelated Chemistries of CO and N ₂	13
1.3.2	Determining Relative Desorption Behavior	18
1.4	Existing Constraints on Relative Desorption Behavior	19
1.4.1	Theoretical X-H ₂ O Bond Energy Calculations	19
1.4.2	Laboratory Temperature Programmed Desorption Experiments	21
1.5	Consequences of Inferred R_B	22
1.5.1	Prestellar Cores	22
1.5.2	Protostellar Cores	23
1.5.3	Protoplanetary Disks	23
1.6	Motivation for this Project	25
2	Ice Desorption Theory	27
2.1	Analytical Modeling	27
2.2	Reaction Order	31
2.2.1	Zeroth-Order Kinetics of Multilayer Desorption	31
2.2.2	First-Order Kinetics of Monolayer Desorption	33
2.2.3	Combining Kinetics of Different Reaction Order	34
2.3	Computational Simulations of Desorption	37
3	Ice Desorption Theory	45
3.1	Experimental Methods	45
3.1.1	Experimental Set-Up	45
3.1.2	Experimental Procedure	48
3.2	Experimental Design	52
3.2.1	Ice Morphologies	53
3.2.2	Surface Coverages	55
3.2.3	H ₂ O Substrate Structures	55
3.3	Experimental Results	58
3.3.1	Pure CO and N ₂ Ices	58

3.3.2	Layered CO/H ₂ O and N ₂ /H ₂ O Ices	59
3.3.3	Mixed CO : N ₂ /H ₂ O Ices	60
4	Model Parameter Estimation	65
4.1	Model Parameters	65
4.2	Markov Chain Monte Carlo (MCMC) Numerical Fitting	67
4.2.1	Bayesian Inference Overview	68
4.2.2	Choice of MCMC Algorithm	69
4.2.3	Comparison to Previous Methods	73
4.2.4	MCMC Sampling Implementation	74
4.3	Parameter Estimation Results	77
4.3.1	Binding Energy Ratio Calculation	88
5	Conclusion	90
5.1	Binding Energy Ratio Results	90
5.2	Astrophysical Implications	91
5.2.1	Desorption Kinetics	91
5.2.2	Protoplanetary Disk Chemistry	91
5.2.3	Molecular Probes of Young Stellar and Planetary Systems	93
5.3	Summary	94
6	References	96

Chapter 1

Introduction

1.1 Ice Sublimation in Protoplanetary Disk Chemistry

Planetary systems evolve from the dust and gas in circumstellar protoplanetary disks surrounding pre-main-sequence stars. Consequently, the elemental compositions of formed planets depend on the astrochemical nature of the parent protoplanetary disk itself. Disks have evolving radial and vertical temperature gradients, as the surface layers of the disk are relatively warm due to interstellar radiation and the midplane temperature decreases further from the central protostar (Aikawa et al. 2002). These temperature gradients determine the overall chemical structure of a protoplanetary disk via the combination of surface layer photochemistry and ice sublimation in the cold, dense region sufficiently far from the central star.

The sublimation of ices in protoplanetary disks is a *desorption* process, in which the molecules accreted onto interstellar ice grains are released from the surface, entering the gas phase. The reciprocal process is *adsorption*, or *freeze-out*, in which gas phase molecules condense to the surface of interstellar ice grains and enter the solid state. Desorption occurs when the temperature is sufficiently high to overcome the reaction barrier, and freeze-out conversely occurs at lower temperatures. The dependence of desorption and freeze-out on temperature results in ice sublimation tracing the radial and vertical temperature gradients of the parent protoplanetary disk, as desorption occurs closer to the protostar and the disk surface layers and freeze-out occurs at further distances in the cold regions of the mid-plane. The boundary of

desorption and freeze-out are marked by a *snowline*, or the disk radius where the mid-plane dust temperature is cold enough for the gas-phase volatile in question to condense onto solid-state ice grains.

Consequently, the evolution of a volatile species in protoplanetary disks is dependent on its relative desorption behavior. Within its snowline, a molecular species will be present in the gas phase and will be able to participate in gas phase chemistry. Conversely, the gas phase abundance of a molecule will decrease and its solid state abundance will increase beyond the snowline as the molecular species will be condensed onto grains, and the volatile will participate in solid state chemistry. The relationship between desorption and adsorption and their snowline separation is shown in Figure 1.1.

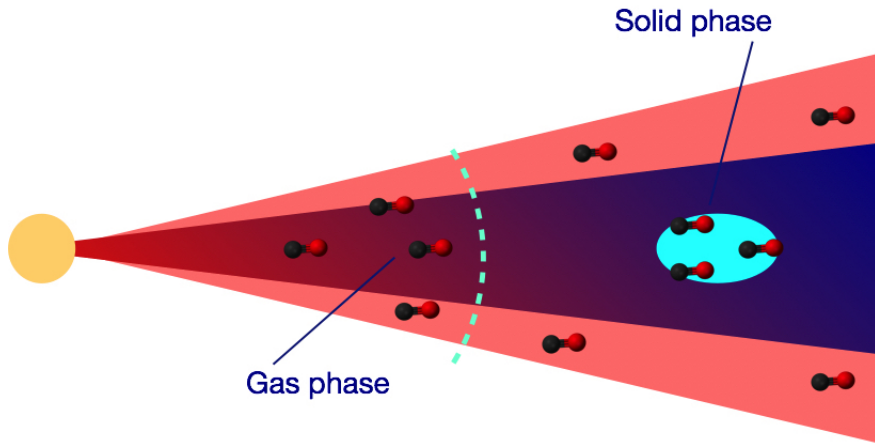


Figure 1.1: *Ice Sublimation in Protoplanetary Disks*: The temperature structure of a protoplanetary disk is characterized by radial and vertical gradients. Closer to the surface layers of the disk, shown in light pink, the temperature is warmer due to external heating from interstellar radiation. In the midplane of the disk, the temperature decreases with radial distance from the central protostar. The snowline, shown by the dotted line, is the boundary between desorption from the solid phase into the gas phase and adsorption from the gas phase onto ice grains.

Understanding of the molecular evolution of volatiles in protoplanetary disk is important constraining the chemistry of planet formation. Firstly, the radial chemical composition constrains the elemental composition of the planetary systems formed therein. In particular, the distribution of organics in protoplanetary disks constrains the abundances of organics present in young planets. Secondly, the disk chemical composition can survive quite intactly in icy planetesimals, e.g. comets (Mumma & Charnley 2011). Subsequently, these icy planetesimals

may have been the means by which water and organic molecules were ferried to Earth, linking protoplanetary disk chemistry to the origins of life (Qi et al. 2013). A diversity of molecular species, including CO, NH₃, and HCN, have been detected in comet Hyakutake and comet Hale-Bopp (Crovisier 1998), and statistical studies of the molecular composition of comets has reveals significant compositional clustering of comets based on formation site.

Predicting the elemental compositions, particularly the distribution of organic species, of young planetary systems and planetesimals requires understanding of the composition of the parent protoplanetary disk itself. In turn, the solid state and gas phase abundances of molecular species throughout the disk is determined by the sublimation behavior of each species. Therefore, understanding the relative desorption and freeze-out processes for volatiles is critical in probing protoplanetary disk chemistry.

1.2 Molecular Probes of Young Stellar and Planetary Systems

Observations of molecular species have the potential to be effective probes of the physical and dynamical states of the origins of star and planetary systems. The environments of young stellar objects are characterized by large amounts of cold gas and dust, and is subject to the coupled dynamical and chemical evolution of gas in the core formation and collapse phases. Since the most abundant molecule in molecular clouds, H₂, is unobservable at the cold temperatures, the fundamental properties of material distribution and volatile physics have been determined almost exclusively from observations of rarer tracer molecules in the gas phase (Bergin et al. 2002). However, the utility of secondary tracers is constrained by our astrochemical understanding of the evolution and distribution of these species in a dynamic environment. Molecular probes have been utilized in observational studies of prestellar cores, protostellar cores, and protoplanetary disks, but the interplay between the gas phase and solid state chemistry is not well understood. Since both early star and planet forming stages are characterized by the presence of both cold, dense gas and icy grain mantles, the chemistry of gas tracers needs to be understood across the different chemical phases and at their interfaces. In particular, molecular species have varying sensitivities to temperature and density gradients, resulting in differential depletions

as molecules enter and leave the gas phase. Consequently, choosing a molecular probe requires understanding how the abundance of the species will change with evolving physical properties. Relying on a depleted gas phase molecule that has frozen out onto an icy grain as a probe opens up the possibility that the astrophysical target, such as distributed material, a prestellar core, or a snow line, evades detection. Meanwhile, the proper choice of molecular probe provides powerful astrophysical insight into physical, chemical, and dynamical properties, such as temperature structures, density distributions, time indicators, energetics, and kinematic profiles. Therefore, determining the desorption behavior of molecular species between the gas phase and solid state and contextualizing relative abundances within an astrochemical network is critical in utilizing molecular probes.

1.2.1 Prestellar Cores

Dense molecular clouds and the prestellar cores embedded within them represent the earliest stage of star formation. These molecular clouds evolve towards cold (≤ 10 K), centrally concentrated cores, which then collapse into protostars. Therefore, understanding of their physical and chemical properties is fundamentally important in understanding and constraining the processes of star formation and evolution. Molecular line observations are the primary means of deriving core physical properties, and have yielded valuable astrochemical insight, especially when coupled with analysis of line intensity ratios and morphologies. The use of molecular probes enables us to observe prestellar core in realtime and thus approximate initial conditions before the formation of a protostar and construct kinematic profiles, in contrast with other methods of tracing material. However, the use of this analysis is contingent on theoretical understanding of molecular abundance evolution. Since the core interior is dense ($\sim 10^5 - 10^6 \text{ cm}^{-3}$, Alves et al. 2001) and cold ($\sim 5 - 10$ K, Bergin et al. 2006), molecular species freeze-out on dust grains further from the envelope edges heated by external interstellar radiation. This results in strong chemical differentiation, as the warmer outer layers remain relatively undepleted and the central cold regions are characterized by the reduction of the abundances of heavy species. For instance, L1517B, a prestellar core located in the Taurus-Auriga complex, exhibited a reduction in CO by 2 – 3 orders of magnitude in the core center (Maret et al. 2013). Furthermore, the

freeze-out is selective, as different chemical species desorb differentially due to their chemical properties.

If well understood, molecular probes can delineate gas temperature and kinematics profiles for prestellar cores. However, the presence of differential depletions can undermine the use of probes as a tracer for star formation kinematics, as measured abundances could possibly be a result of both kinematics and desorption. Meanwhile, a careful choice of tracers with known desorption behavior can provide a means of reconstructing the radial profile of kinematical motions deeper into star-forming regions.

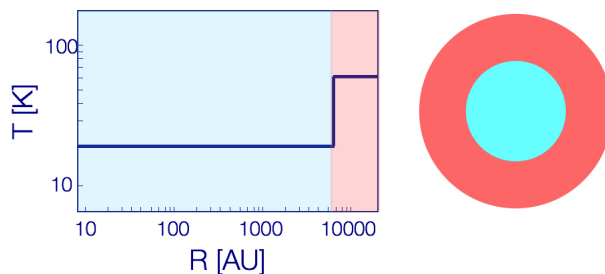
1.2.2 Protostellar Cores

In the protostellar stages, the dense prestellar core has collapsed, forming a central protostar surrounded by collapsing envelope material. The chemistry in both prestellar and protostellar stages of star formation is significantly influenced by the freeze-out of molecules onto dust grains, later affecting the thermal evolution of the central cores. This is evidenced by similar depletion holes found in prestellar cores also observed in more evolved protostars. However, the protostellar energy structure critically differs from its prestellar predecessor due to the presence of the centrally radiating protostar, as schematically shown in Figure 1.2.

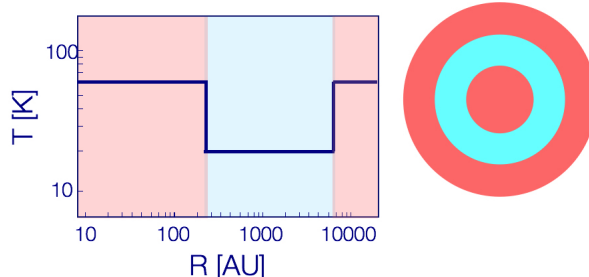
In the prestellar stages, the thermal balance is dominated by the external interstellar radiation field, which generally does not heat the material to temperatures higher than ≈ 15 K (Jørgensen et al. 2005). The interstellar radiation heats the edges of the prestellar envelope, which then evolve towards a cold center. Due to this low temperature, most molecules gradually freeze-out, with longer timescales toward the exterior, potentially longer than the age of the core, and at very short timescales at the innermost dense regions, potentially shorter than the collapse time.

Conversely, in the protostellar stages, the thermal balance is dominated by the newly formed central protostar, introducing a steep temperature gradient toward the core center. Radiative transfer modeling of dust continuum emission reveals that characteristic temperatures can rise to several hundred Kelvin in the innermost regions (Jørgensen et al. 2002). While molecules freeze out into the solid state from the edges of the envelope heated by in-

terstellar radiation, the central protostar enables desorption back into the gas phase towards the center. Significant depletions are still observed in the protostellar stage, implying that a substantial fraction of the envelope material in between the radiated outer layers and heated core surroundings remains at sufficiently low temperatures, resulting in a shell-like temperature structure. However, the progressive return of a molecular species into the gas phase towards the centrally radiating protostar from the intermediate freeze-out zone enables gas probes to trace current and past temperature profiles of the protostar and link the respective time scales of the prestellar and protostellar stages of star formation.



(a) Prestellar Core



(b) Protostellar Core

Figure 1.2: Ice Sublimation in Young Stellar Objects: The proposed chemical evolutionary sequence for prestellar and protostellar objects is shown, with freeze-out regions (gas to solid) shown in blue and desorption regions (solid to gas) shown in red. The left column gives the abundance structure of a molecular species, and there with column gives the depletion signature going from the outside to the inside of the object. For prestellar cores, gas phase abundances are high at the outer edges of the envelope due to heating from external interstellar radiation, but then depletion occurs closer to the central core as temperatures drop and density increases. For protostellar cores, gas phase abundances are high at the outer edges, heated by external radiation, and also towards the central protostar, and the intermediate cold region is characterized by freeze-out.

1.2.3 Protoplanetary Disks

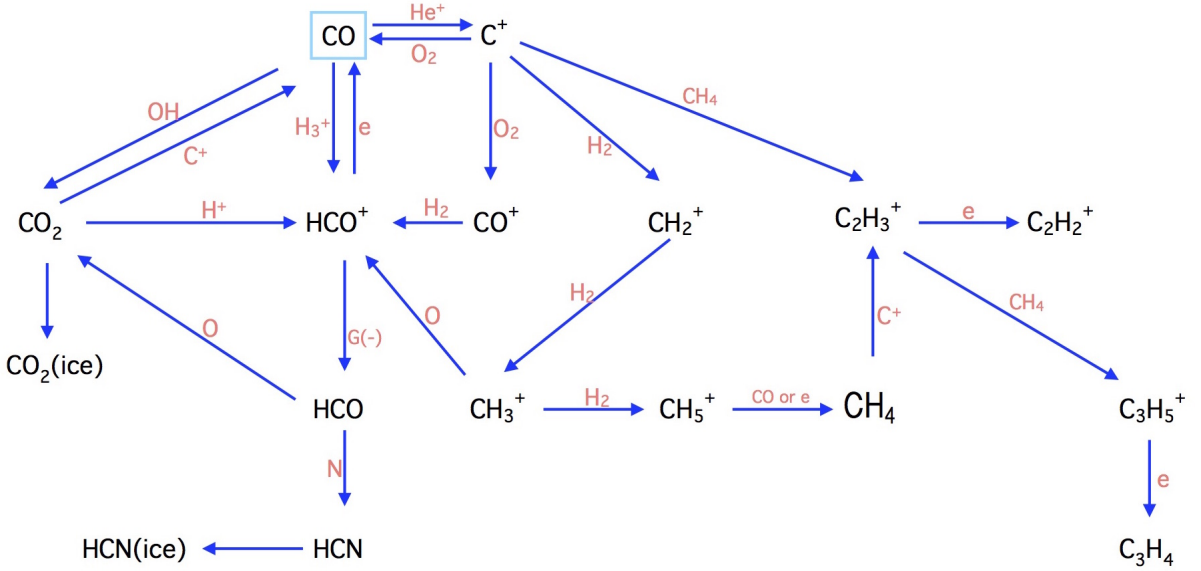
In addition to being the origins of young planetary systems, protoplanetary disks serve as accretion disks for the protostars they surround. A protostar grows to main sequence stellar mass as material infalls from the inner edges of the circumstellar protoplanetary disks onto the protostellar surface. Therefore, molecular tracing of disk chemistry by gas probes yields information on both star and planet formation. Molecular abundances in both the solid and gas phases are sensitive to the physical and chemical conditions of the specific disk region. Consequently, molecular emission lines can probe disk characteristics, such as density, thermal history, ionization fraction, and atmospheric composition, generally inaccessible to other means of observation. In turn, tracing these fundamental properties constrains the initial conditions and processes of nascent planetary system formation and protostellar evolution.

Therefore, understanding of in addition to determining the elemental compositions of young planets and icy planetesimals, the distribution of molecules in the protoplanetary disk constrains the processes of young planet and star formation. However, the utility of molecular tracers of protoplanetary disk chemistry requires understanding of the distribution of the probe throughout the disk, which in turn depends on the relative desorption and adsorption processes.

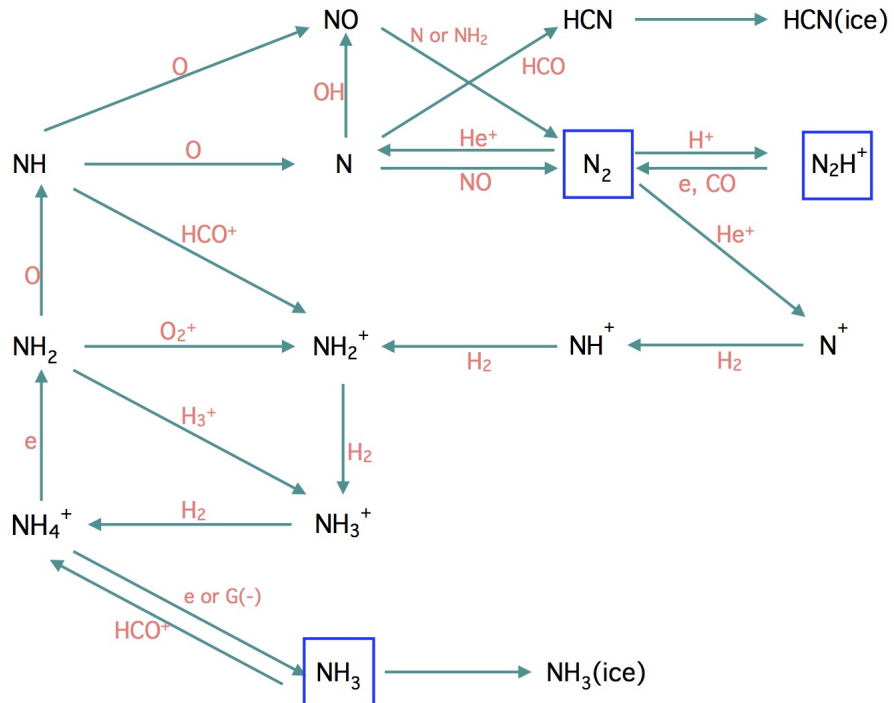
1.3 The Role of CO and N₂ as Molecular Probes

Carbon monoxide (CO) and molecular nitrogen (N₂) are immediate choices of gas phase tracers since both are highly abundant in interstellar molecular clouds and are also carriers of critical elements C, N, and O. The gaseous CO abundance has been recorded in warm regions as high as 2.7×10^{-4} with respect to H₂, indicating that CO contains most of the carbon not locked up in refractory material (Lacy et al. 1994). While the solid CO abundance is more variable between sources, the relative abundance has been measured on the order of 10^{-4} with respect to H₂ in very cold cores (Pontoppidan et al. 2005). The sub-millimeter line and continuum data measurements of the amount of CO frozen out in prestellar cores indirectly suggest more than 90% of the CO is removed from the gas phase, consistent with these high measured solid-state abundances (Jørgensen et al. 2005). Meanwhile, since N₂ does not have a

permanent dipole moment, the species cannot be directly detected and its gas phase abundance is typically inferred from the presence of daughter species N_2H^+ . Inferred gas phase abundances have been measured on the order of $10^{-6} - 10^{-5}$ with respect to H_2 in star-forming regions, or approximately 10% of the total nitrogen abundance (van Dishoeck et al. 1992). More recently, the gas phase abundance of N_2 in dark cores has been estimated as $1 - 2 \times 10^{-5}$ with respect to H_2 (Bergin et al. 2002). Furthermore, millimeter N_2H^+ data suggests that approximately 50% of N_2 freezes out onto grains in dense cores. The chemical networks of major reactions involving carbon and nitrogen are shown in Figure 1.3. CO has been used to accurately trace the distribution of material in molecular clouds, enabling us to construct kinematic profiles. However, the abundance of CO has been shown to significantly decrease at lower temperatures characteristic of cold, dense regions, which has been attributed to the freezing of gas-phase CO onto the surfaces of cold grains. As such, the utility of CO as a tracer is limited closer to prestellar cores, in the intermediate cold region of protostellar cores, and in the cold mid-plane region separated from the warm center and surface layers of protoplanetary disks. Meanwhile, millimeter observations have revealed that an increase in the abundance of N_2H^+ (the protonated daughter of N_2) has been observed to coincide with CO depletion in both prestellar and protostellar cores (Bergin et al. 2002, Belloche & Andre 2004). This indicates that N_2H^+ remains in the gas phase at colder temperatures than CO, implying that this molecule could probe more deeply into cold, dense regions where CO has already condensed onto interstellar ices. Alternatively, understanding the difference in desorption behavior between N_2 and CO could provide an opportunity to utilize N_2H^+ as a molecular tracer in environments where CO is not present in the gas phase.



(a) Carbon-based reactions



(b) Nitrogen-based reactions

Figure 1.3: *Major reactions in star-forming regions:* The molecular species that link the carbon and nitrogen families are boxed. Astrophysical species of interest, namely CO and N₂, have interrelated chemistries determined by relative abundances, despite being of different elemental families. The grain-surface recombinations are denoted by “G(-)”.

1.3.1 Interrelated Chemistries of CO and N₂

The anti-correlation in the gas phase abundances of N₂H⁺ can be understood by examining the interrelated chemistries of these species. Despite the fact that CO and N₂ belong to different elemental families, the chemistries of these molecules are inextricably linked through an abundance-dependent chemical network. Specifically, two alternative chemical scenarios can occur, depending on gas-phase abundance of CO, as shown in Figure 1.4.

Standard CO Abundance Network

In the general case of a “standard” undepleted CO abundance of [CO/H₂] $\sim 10^{-4}$, CO and N₂ form daughter molecules HCO and N₂H⁺ through protonation reactions with H₃⁺, i.e.:



where the main formation route of H₂⁺ is through cosmic ray ionization of H₂:



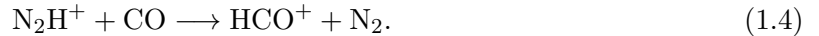
It is worth noting that HCO⁺ is important in chemical models of prestellar and protostellar environments, as it is the primary molecular ion and thus regulator of the electron density/ionization structure (Caselli et al. 2002), and a critical destroyer of other molecules (Bergin and Langer 1997). The correlation between HCO⁺ and parent species CO has been derived by Jørgensen et al. (2003) to be linear, approximately as:

$$[\text{HCO}^+] = (7.4 \times 10^{-5}) \times [\text{CO}]$$

or alternatively, a standard CO abundance corresponds to an HCO^+ abundance of 7.4×10^{-9} . In this general case of standard CO abundance, Equation (1.1)(a) is the dominant destruction mechanism of H_3^+ . Meanwhile, both HCO^+ and N_2H^+ are destroyed via dissociative recombination, resulting in parallel reactions:



Both the formation and dissociative recombination reactions occur at a similar rate for both CO and N_2 , so the measure of the measure of the $\text{HCO}^+/\text{N}_2\text{H}^+$ abundance ratio is directly related to the CO/ N_2 abundance ratio. However, while dissociative recombination is the main destruction mechanism for HCO^+ in the general case, the main removal pathway for N_2H^+ is via an additional destruction reaction with CO:



This destruction pathway does not have an analogous HCO^+ counterpart, and dominates over the dissociative recombination removal of N_2H^+ that is paralleled by HCO^+ . Therefore, at standard abundances, CO becomes the primary destroyer of N_2H^+ in the gas phase.

We can now quantify the anti-correlation between CO and N_2H^+ in the general case of standard CO abundance. We introduce the rate coefficients for each reaction, with k_{HCO^+} , $k_{\text{N}_2\text{H}^+}$, and k_{CO} being the rate coefficients for Equations (1.1)(a), (1.1)(b), and (1.3)(a), respectively, and k_{N_2} and k'_{N_2} being the rate coefficients for Equations (1.3)(b) and (1.4), respectively. Assuming steady state, the HCO^+ destruction and formation balances such that:

$$k_{\text{HCO}^+} n_{\text{H}_3^+} n_{\text{CO}} = k_{\text{CO}} n_{\text{HCO}^+} n_{\text{e}} \quad (1.5)$$

where n_{HCO^+} , $n_{\text{H}_3^+}$, n_{CO} , and n_{e} are the densities of HCO^+ , H_3^+ , CO, and electrons, respectively.

At standard CO abundances on the order of $\sim 10^{-4}$, the main removal mechanism for H_3^+ is Equation (1.1)(a), hence equating the formation and destruction rate for H_3^+ yields:

$$\zeta n_{\text{H}_2} = k_{\text{HCO}^+} n_{\text{H}_3^+} n_{\text{CO}} \quad (1.6)$$

where ζ is the cosmic ray ionization rate and n_{H_2} the H_2 density. We assumed that each H_2^+ molecular ion produced in Equation (1.2) immediately reacts with H_2 to form H_3^+ . Thus, from Eqs. (1.5) and (1.6), we can write:

$$\zeta n_{\text{H}_2} = k_{\text{CO}} n_{\text{HCO}^+} n_e. \quad (1.7)$$

We can now divide Equation (1.7) by $n_{\text{H}_2}^2$, introduce the abundances $[X] = n_X / n_{[\text{N}_2]}$, and isolate $[\text{HCO}^+]$, yielding:

$$[\text{HCO}^+] = \frac{\zeta / n_{\text{H}_2}}{k_{\text{CO}} [e]}. \quad (1.8)$$

Similarly, we can equate the formation, Equation (1.1)(b) and destruction (both via dissociative recombination and via CO), Equations (1.3)(b) and(1.4) rates for N_2H^+ :

$$k_{\text{N}_2\text{H}^+} n_{\text{H}_3^+} n_{\text{N}_2} = k'_{\text{N}_2\text{H}^+} n_{\text{N}_2\text{H}^+} n_{\text{CO}}. \quad (1.9)$$

Using Equation (1.6), we can substitute in for $n_{\text{H}_3^+}$:

$$k_{\text{N}_2\text{H}^+} n_{\text{N}_2} \frac{\zeta n_{\text{H}_2}}{k_{\text{HCO}^+} n_{\text{CO}}} = k'_{\text{N}_2\text{H}^+} n_{\text{N}_2\text{H}^+} n_{\text{CO}}, \quad (1.10)$$

allowing us to derive an expression for the N_2H^+ abundance:

$$[\text{N}_2\text{H}^+] = \frac{[\text{N}_2]}{[\text{CO}]^2} \frac{k_{\text{N}_2\text{H}^+}}{k'_{\text{N}_2} k_{\text{HCO}^+}} \zeta / n_{\text{H}_2}. \quad (1.11)$$

We see that the abundance of N_2H^+ is inversely proportional to the squared abundance of CO, implying that the abundance of N_2H^+ will rapidly decline as CO desorbs into the gas phase and will rapidly increase as CO freezes out into the solid state.

Depleted CO Abundance Network

When CO condenses onto icy grains and leaves the gas phase, the chemical network remains the same, except the N_2H^+ destruction via CO, Equation 1.4, is removed. In this case of depleted CO abundance, the dissociative recombination reactions are the main destruction mechanisms for both HCO^+ and N_2H^+ . Consequently, when CO is depleted, the abundance of N_2H^+ increases as its primary gas phase destroyer freezes out, providing the chemical basis for anti-correlation between N_2H^+ and CO.

We can quantify the effects of CO freeze-out by determining the N_2H^+ abundance, but in this case with the removal of the removal pathway via CO (Equation (1.4)) in the depleted CO scenario. In this low [CO] limit, the main removal mechanism, Equation (1.1)(b) becomes more important than Equation (1.1)(a) in the removal of H_3^+ , so we instead write for the formation and destruction balance for H_3^+ :

$$\zeta n_{\text{H}_2} = k_{\text{N}_2\text{H}^+} n_{\text{H}_3^+} n_{\text{N}_2}, \quad (1.12)$$

replacing Equation 1.6 in this scenario. From Equations (1.5) and (1.12), we can then eliminate n_{HCO^+} :

$$\begin{aligned} n_{\text{HCO}^+} &= n_{\text{CO}} \frac{k_{\text{HCO}^+}}{k_{\text{CO}}} \frac{n_{\text{H}_3^+}}{n_e} \\ &= n_{\text{CO}} \frac{k_{\text{HCO}^+}}{k_{\text{CO}}} \frac{\zeta n_{\text{H}_2}}{n_e k_{\text{N}_2\text{H}^+} n_{\text{N}_2}}, \end{aligned} \quad (1.13)$$

or alternatively in terms of abundances:

$$[\text{HCO}^+] = \frac{k_{\text{HCO}^+}}{k_{\text{CO}} k_{\text{N}_2\text{H}^+}} \frac{\zeta / n_{\text{H}_2}}{[e][\text{N}_2]} [\text{CO}]. \quad (1.14)$$

quantifying the linear proportionality between the HCO^+ and CO abundances. We see that the abundance of HCO^+ is linearly proportional to the CO abundance when CO is depleted, while at higher abundances, the abundance of HCO does not depend on ([CO]) since the formation and destruction pathways are balanced.

Additionally, in this low [CO] limit, the destruction of N_2H^+ is not via CO but is by dissociative recombination, Equation (1.3)(b), hence the formation and destruction balance for N_2H^+ can be written as:

$$k_{\text{N}_2\text{H}^+} n_{\text{H}_3^+} n_{\text{N}_2} = k_{\text{N}_2} n_e n_{\text{N}_2\text{H}^+}. \quad (1.15)$$

It follows again from eliminating $n_{\text{H}_3^+}$ using Equation (1.6) and rewriting the expression in terms of abundances that:

$$[\text{N}_2\text{H}^+] = \frac{\zeta/n_{\text{H}_2}}{k_{\text{N}_2} [\text{e}]}. \quad (1.16)$$

Therefore, in the low [CO] limit, the abundance of N_2H^+ is constant. In summary, we see that at standard CO abundances, the HCO^+ abundance does not depend on the CO abundance, whereas the N_2H^+ abundance declines quickly as $[\text{CO}]^{-2}$. In the low [CO] limit, however, the HCO^+ abundance is linearly proportional to the CO abundance, whereas the N_2H^+ abundance is constant. Consequently, the chemical outcome critically depends on the relative abundances of CO and N_2 , which in turn depends on the relative desorption behavior of CO and N_2 .

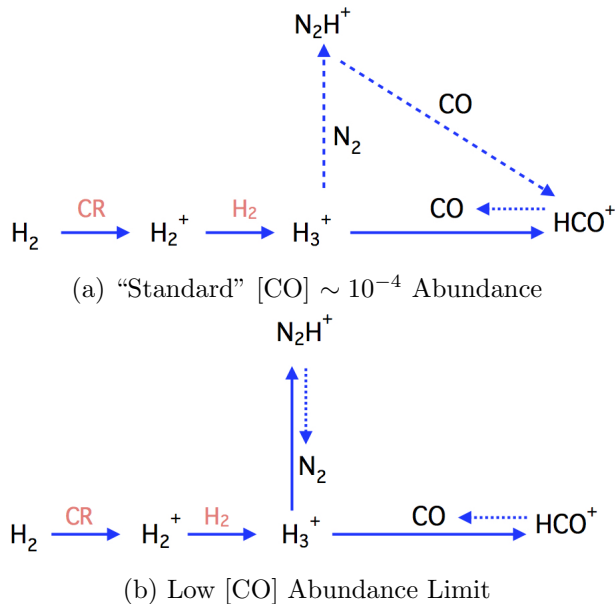


Figure 1.4: *[CO]-Regulated Chemical Network*: The chemical networks as a function of CO abundance are given for undepleted and depleted scenarios. The dominant reactions are indicated by solid arrows and secondary reactions by dashed arrows. Where dissociative recombination is the main destruction pathway for a molecule (i.e. N_2H^+ or HCO^+), a dotted arrow has been used.

1.3.2 Determining Relative Desorption Behavior

The system of formation and destruction described above depends on the relative abundances of CO and N₂, which in turn are determined by the balance of freezeout timescales (primarily dependent on density) and desorption timescales (dependent on grain temperature, binding energies, and desorption kinetics). The thermal desorption rate ξ and freeze-out rate λ (both in units of s⁻¹) can be written as:

$$\xi(M) = \nu(M) \exp\left(\frac{-E_b(M)}{kT_d}\right), \quad (1.17)$$

$$\lambda(M) = 4.55 \times 10^{-18} \left(\frac{T_g}{m(M)}\right)^{0.5} n_H, \quad (1.18)$$

where $\nu(M)$ is the vibrational frequency of molecular species M in its binding sites, T_d and T_g the dust and gas temperatures, respectively, $m(M)$ the molecular weight, n_H the total hydrogen density, and $E_b(M)$ the binding energy of the molecule depending on the ice mantle composition. The desorption and freeze-out timescales are then defined as $1/\xi(M)$ and $1/\lambda(M)$, respectively. Models reasonably assume that at grain temperatures less than 14 K, all sticking probabilities are close to 1 for molecules with the same masses, such as N₂ and CO, so the freezeout timescales are identical for a given grain density (Bisschop et al. 2005). Thus, the relative abundances are critically hinged on the relative desorption behaviors of CO and N₂. The critical parameter in determining desorption behavior is the binding energy onto the grain surface. Most molecules are believed to be weakly adsorbed or physisorbed onto the surfaces of grains. For the adsorbed species, the binding energy varies depending on the surface species and is proportional to the polarizability of the adsorbed and dominant species (Bergin and Langer 1997). In gas-grain models, the anti-correlation is explained by assuming that the difference between the desorption rates of CO and N₂ is a direct function of the ratio between their binding energies:

$$R_B = \frac{E_{B, \text{N}_2}}{E_{B, \text{CO}}}. \quad (1.19)$$

The anti-correlation is quantitatively reproduced in astrochemical models by taking R_B to be between 0.5 and 0.75.

1.4 Existing Constraints on Relative Desorption Behavior

The critical parameter determining the relative desorption behavior, and in turn the molecular abundances, of CO and N₂ through their linked chemical network is the binding energy ratio between the two species. Consequently, chemical understanding of CO and N₂ and the applicability of these molecules as tracers is contingent upon accurate calculation of the binding energy ratio, denoted as R_B . Historically, R_B has been extrapolated from surface/adsorbate theory and matched to observed abundances. However, recent laboratory advances have enabled R_B to be measured in controlled, astrophysically relevant experiments.

1.4.1 Theoretical X-H₂O Bond Energy Calculations

Sadlej et al. (1994) theoretically investigated the H₂O…H₂, H₂O…N₂, and H₂O…CO complexes by comparing *ab initio* calculations to experimental results for gaseous adsorbates (H₂, N₂, and CO) on icy surfaces. Weak intermolecular interactions are difficult to calculate accurately, and *ab initio* calculations computations are generally limited to gaining qualitative understanding of interaction potentials. Weak bonding induces frequency changes in the vibrational spectra of molecules, and mapping of the frequency changes of monomers provides an understanding of local environments of molecules in matrices, solutions, clusters, and on surfaces. Typically, simple phenomenological models for dependence of the potential on monomer vibrational coordinates are used to calculate frequency shifts. For instance, the intermolecular potential can be modeled as the sum of interatomic distances; subsequently, the frequency shifts are assumed to solely depend on the distortion of the monomer by such interatomic terms. Alternatively, monomer frequency shifts are assumed to be dominated by a particular intermolecular interaction (*e.g.*, induced dipole-permanent dipole, induced dipole-induced dipole), then the asymptotic long range formula is used for these interactions as the vibrational dependence is integrated via the polarizability or dipole with respect to vibrational coordinates. Moreover,

in addition to frequency shifts, the effects of weak bonding can also be seen in changes in infrared intensities paired with monomer frequency shifts; therefore, intensity shifts were also calculated in the weakly bonded complexes. The full set of calculations included optimization of geometries, decompositions (electrostatic, exchange, and dispersion) of the intermolecular interactions, and calculation of the harmonic vibrational frequencies. The vibrational frequencies and infrared intensities across all components for two minima structures of $\text{H}_2\text{O}\cdots\text{N}_2$ (H-bonded minimum and O-bonded T-shaped) and for three minima structures of $\text{H}_2\text{O}\cdots\text{CO}$ (H-bonded $\text{OC}\cdots\text{H}_2\text{O}$, H-bonded $\text{CO}\cdots\text{H}_2\text{O}$, and O-bonded T-shaped) were calculated. The minimum energies for $\text{H}_2\text{O}\cdots\text{N}_2$ and $\text{H}_2\text{O}\cdots\text{CO}$ were found to be -403 and -616cm^{-1} , respectively. These results were connected to experimental data on infrared spectra of ice surface/adsorbate systems, reproducing several notable experimental effects, namely: ¹. blueshift in CO frequency upon formation of the weak OH \cdots CO bond, and ². small effects of bonding to H_2O on the N_2 frequency.

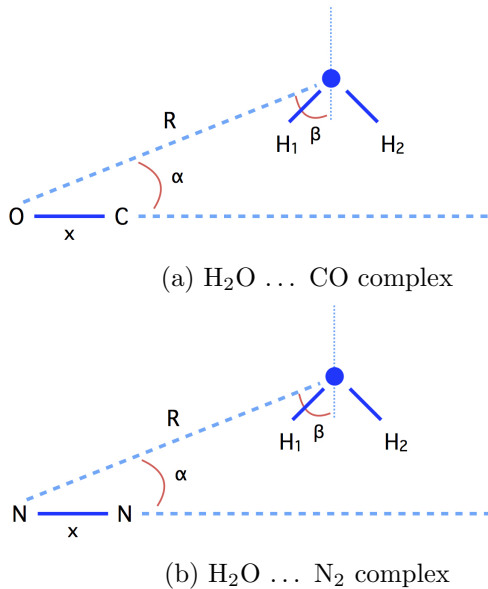


Figure 1.5: *Dimer H_2O Complexes:* The H_2O complexes analyzed to obtain *ab initio* calculations of the vibrational spectra are shown (Sadlej et al. 1995). Global geometry optimization yields the equilibrium structures above, in which the diatomic is bonded to a H atom of water in an approximately collinear configuration. The in-plane parameters include the intermolecular distance R , midpoint of the diatomics x , and angles α and β measuring the rotations of the monomers with respect to the intermolecular axis

The results of theoretical study and observed difference in bond interactions justified

the assumption implemented in astrochemical models of a binding energy ratio of $R_B \approx 0.60$, which in turn was required to explain the observed anti-correlation of CO and N₂H⁺ in young star and planet forming regions. However, the quantitative comparability is limited between the calculated spectra of dimers, schematically visualized in Figure 1.5, and the experimental spectra of many body adsorbate/surface systems. Furthermore, while such phenomenological models work for local and constrained systems, the fundamental causes of these frequencies and extrapolation beyond the dimer level is not yet well understood.

1.4.2 Laboratory Temperature Programmed Desorption Experiments

Until 2005, the *ab initio* cluster calculations justified assuming a lower binding energy of N₂ relative to CO to interstellar grains in astrochemical models to reproduce the observed anti-correlation. However, the binding energies of CO and N₂ were precisely measured in Öberg et al. (2005) and Bisschop et al. (2006). In these laboratory studies, the desorption curves of CO and N₂ from pure, layered, and mixed ice morphologies were across various ice thicknesses and abundance ratios were measured. These experiments were carried out in ultrahigh vacuum laboratory conditions via Temperature Programmed Desorption (TPD) experiments at temperatures astrophysically relevant to cold, dense regions. Additionally, a kinetic model was developed to constrain the binding energies of CO and N₂ in both pure and mixed environments and to derive the desorption, mixing, and segregation kinetics, particularly reaction order. The ratio of binding energies was experimentally found to be $R_B = 0.936 \pm 0.03$ in pure ices and virtually unity in mixed ice fractions, and the results were reproduced by the kinetic model applied to astrophysical relevant conditions for cold prestellar cores and protostars. Furthermore, the sticking probabilities for CO–CO, N₂–CO, and N₂–N₂ at 14 K were found to have the same lower limit of 0.87 ± 0.05 . As such, the combined results from the desorption experiments, the kinetic model, and the sticking probability data imply that the solid-state processes and desorption behavior of CO and N₂ are very similar under astrophysical relevant conditions. In particular, the binding energy ratio R_B is experimentally calculated to be significantly closer to 1.0 than assumed in astrochemical models reproducing the observed anti-correlation.

1.5 Consequences of Inferred R_B

1.5.1 Prestellar Cores

Bergin and Langer (1997) developed a chemical model of forming and collapsing low-mass protostellar cores which investigates the effect of the competition between grain surface molecular depletion and desorption on the gas phase chemistry. Three desorption mechanisms that remove species from the solid state were incorporated: thermal evaporation, cosmic ray induced desorption, and photo evaporation. Moreover, two different surfaces were modeled: a grain mantle dominated by CO ice and a surface composed of H₂O ice. Based on the cluster calculations of Sadlej et al. (2005), the binding energy ratio was taken as $R_B = 0.65$ and $E_b(\text{CO} - \text{CO}) = 960$ K. Consequently, the high volatility of parent molecule N₂ allowed for the various desorption mechanisms to maintain a significant abundance of N₂, and in turn N₂H⁺ abundance, in the gas phase at high densities. As a result of the low relative binding energy adopted for N₂, the model reveals little depletion for gas phase N₂H⁺, even in a strongly binding environment. However, this study examines the hypothetical case when the binding energy of N₂ is equal to that of CO, which resulted in similar depletions for both N₂H⁺ and CO in the strongly binding H₂O ice environment.

The anti-correlative depletion pattern between CO and N₂H⁺ is confirmed in a later observational study of the Northern streamer of the IC 5146 cloud (Bergin et al. 2001). Subsequently, Bergin et al. (2002) extended the chemical model of Bergin and Langer (1997) to reproduce the observations of N₂H⁺ in dark globule B68. Molecular line observations of CO and N₂H⁺ revealed widespread CO depletion throughout the centrally condensed core of the prestellar dark B68 cloud and N₂H⁺ peaks inside the much larger CO depletion hole. The anti-correlation and high density center holes in B68 are quantitatively reproduced with initial values $E_B(\text{CO} - \text{CO})$ and $E_B(\text{N}_2 - \text{N}_2)$ of 1210 and 750 K, respectively ($R_B = 0.62$). However, the best fit to the observed emission is produced with an increase in $E_B(\text{N}_2 - \text{N}_2)$ to 900 K ($R_B = 0.75$).

1.5.2 Protostellar Cores

In addition to the studies of prestellar cores, Jørgensen et al. (2004) examined the molecular inventories and chemical evolution of low-mass protostars, which are objects that have formed a central protostar, but are still deeply embedded in their envelopes and represent the first stage after the collapse of the dark cloud cores. An empirical chemical network was constructed on the basis of correlations of the abundances of various species. Notably, the linear correlation between HCO^+ and CO abundances is observed, both increasing with decreasing envelope mass, confirming that the main formation route of HCO^+ is via reactions between CO and H_3^+ . Importantly, the rapid decline of N_2H^+ with higher CO abundances is observed in the sample of low-mass protostars. A subsequent observational study of deeply embedded low-mass protostar L483-mm revealed that mapped N_2H^+ emission was strongest at two lobes, with N_2H^+ being absent from the gas-phase close to the central protostar (Jørgensen 2004). In contrast, CO is mainly seen very closely confined to the region around the central protostar, reflecting the destruction of N_2H^+ via reactions with CO. This supports the conclusion that CO abundances peak towards the central regions where CO has desorbed from the grain mantles, whereas N_2H^+ abundances peak away from the central continuum position where CO is frozen out.

1.5.3 Protoplanetary Disks

As described earlier, molecular abundances are also relevant in our understanding and study of protoplanetary disks, particularly in constraining the properties and states of planetesimal formation processes and the elemental compositions of primitive bodies. In current disk chemistry models, such as the one proposed by Aikawa et al. (2002), the sequential freeze-out of molecules of molecules in the disk interior is coupled with photochemistry on the disk surface, reflecting both the vertical and radial temperature gradients. Analogously to desorption patterns in dense cores, CO is predicted to deplete from the gas phase at $T < 20 - 25$ K at typical mid-plane densities, in turn accompanied by an increase in the N_2H^+ abundance under the assumption of a binding energy ratio of $R_B = 0.60$. In disk models, this anti-correlation is manifested in a sharp increase in the N_2H^+ column density at the CO snow line. Therefore, N_2H^+ can

be used as a CO snowline tracer. In our Solar System, we often consider the H₂O snow line, which divides the rocky planets and gas giants. The CO snow line is of particular interest, since gas phase CO may augment planet formation in the outer ring by providing additional solid matter and by inducing planet traps, and could subsequently affect the molecular composition of exterior gas giants. Additionally, CO ice is needed to form methanol, which is a building block of more complex organic molecules essential to life. Meanwhile, since CO is more volatile ($T_{freezeout} = 20$ K) relative to H₂O, the CO snow line should be much further from the central star and thus easier to observe.

Meanwhile, H₂CO formation in the solid state has been theoretically and experimentally shown to form readily from CO-ice hydrogenation (Watanabe et al. 2003), thus solid state formation should increase with CO freeze-out. If this is the dominant formation pathway of solid state H₂CO, then gas phase H₂CO should coincide with the jump in N₂H⁺ exterior to the CO snow line. Furthermore, H₂CO and N₂H⁺ have been detected toward multiple protoplanetary disks, predominantly toward T Tauri stars with massive disks and less so toward luminous Herbig Ae stars. This implies that H₂CO and N₂H⁺ should be primarily abundant in disks with large reservoirs of cold, dense gas - where CO freeze-out is expected to occur.

Qi et al. (2013) tested existing understanding of the protoplanetary disk chemistry by analyzing the distributions of H₂CO and N₂H⁺ emission, which is strong in millimeter observations, in relation to CO in the protoplanetary disks surrounding T Tauri star TW Hya and the Herbig Ae star HD 163296 using Submillimeter Array (SMA) data. The H₂CO and N₂H⁺ emission toward HD 163296 was found to be offset from the continuum peak at a size scale consistent with a CO snow line at 160 AU, and is matched by a ring model in which H₂CO is present only in regions of CO freeze-out. Additionally, the H₂CO excitation temperature was found to be below ~ 20 K, again consistent with the hypothesis that H₂CO should be most abundant in regions of CO freeze out. Lastly, the H₂CO and N₂H⁺ emission was correlated across the disk sample, in accordance with the theoretical prediction that both should co-exist beyond the CO snow line in regions of gas phase CO depletion. This study revealed that the CO snow line can be constrained by trace species that appear where CO has begun to freeze out, and H₂CO and N₂H⁺ are potential candidate probes for CO snow lines in other disks.

However, this process of constraining the CO snow line is contingent upon understanding the relative desorption behavior of the molecular probes in relation to the volatile snow line species.

Additionally, Ceccarelli and Dominik (2005) studied the implications of CO and N₂ desorption behavior on deuterated species in protoplanetary disks. The effect of having N₂ in the gas phase where CO molecules are depleted influences the abundances of H₃⁺ and its isotopomers, causing an additional term of H₃⁺ (consequently H₂D⁺ and HD₂⁺) destruction. As such, observations of H₂D⁺ in protoplanetary disks should correlate with large relative depletions of CO and N₂ (Ceccarelli and Dominik 2005).

In summary, N₂H⁺ has been used to trace the CO snowline under the assumption that the binding energy ratio $R_B < 1.0$. This binding energy differential allows N₂H⁺ to remain in the gas phase longer while CO freezes out, so it can experience an increase in abundance as its primary gas phase destroyer is removed. In turn, we can observe this increase in N₂H⁺ abundance, and use it to localize the CO snowline in protoplanetary disks. However, if the binding energy ratio R_B is closer to 1.0, the desorption behavior between N₂H⁺ and CO should not be very different, and that the two molecules should have very similar snowlines.

1.6 Motivation for this Project

Gas phase molecular probes have the potential to yield valuable astrophysical insight into young star and planet forming regions. Understanding the radial distribution of molecules, as marked by snowlines, in protoplanetary disks not only constrains the elemental composition of young planets and planetesimals formed therein, but also provides information on the conditions of planet formation. Moreover, molecular probes of prestellar and protostellar cores can trace material distribution and volatile physics in prestellar and protostellar cores. In particular, CO and N₂ are primary candidates for molecular tracers, as they are highly abundant in interstellar clouds; are carriers of C, N, and O; and are observationally accessible. However, current usage of these gas phase tracers is limited by the uncertainty regarding their relative desorption behavior. The discrepancy between the experimental binding energy ratio and previous modeling assumptions made to match observations has been suggested to be due to the presence of H₂O

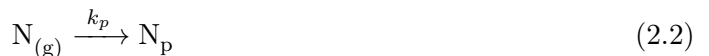
contamination in interstellar ices. The strong dipole moment of H₂O could result in preferential binding to CO, which does have permanent dipole polarity, over N₂, which has no dipole moment. While H₂O is present in interstellar ices, laboratory work has previously considered various morphologies of pure CO and N₂ ices. Therefore, it is possible that the binding energy ratio needed by astrochemical models to explain observations of $R_B \approx 0.60$ reflects the differential effect of H₂O in interstellar ices, which was not examined in a laboratory setting. Motivated by the possible effects of H₂O on the measured binding energy ratio between N₂ and CO, and in turn relative desorption behavior, this thesis involves a series of laboratory experiments to directly measure the desorption curves of CO and N₂ in scenarios with H₂O ices. Based on the experimental evidence, we determine the likelihood and under which characteristics CO and N₂ desorption energies differ significantly, and discuss the implications in astrophysical environments.

Chapter 2

Ice Desorption Theory

2.1 Analytical Modeling

An analytical model was constructed to gain a clearer qualitative and quantitative understanding of the desorption behavior of various ice scenarios. The aims of the model are twofold: to model and reproduce the experimental data, and to use the model parameters to predict the kinetic behavior of CO and N₂ in astrophysical ices. To model the kinetics of ice desorption, we consider the following reaction scheme for an element N desorbing into the gas phase, then being pumped out by the experimental apparatus:



where k_d is the desorption rate constant, k_p is the pumping rate constant, and $N_{(x)}$ represents the number of molecules in state x , equivalent to the state concentration. Mathematically, we construct an analytical model for this chemical scenario by writing differential equations for each the concentration of molecules in each state over a temperature range. The rate of desorption, denoted R , is given by Fraser et al. (2001) as:

$$R = \frac{-dN_{(s)}}{dt} = k_d[N_{(s)}]^i, \quad (2.3)$$

where $N_{(s)}$ is the number of solid state molecules evaporating from the substrate into the gas phase, t is time in seconds, $[N_{(s)}]$ is the number of molecules adsorbed molecules of element N on the surface in units of molecules cm^{-2} , i is the order of the reaction, and k_d is the rate constant, given by

$$k_d = v_i \exp(-E/k_B T), \quad (2.4)$$

where v_i is a pre-exponential factor that measures attempt frequency, E is the binding energy (reaction barrier) in joules, k_B is the Boltzmann constant, and T is the temperature in kelvin. For convenience, in this thesis the surface binding energies are expressed as $E_B = E/k_B$, i.e. in kelvin. The units of v_i are determined by the reaction order and k_d : i.e. for $i = 1$, v_1 is expressed in s^{-1} ; and where $i = 0$, v_0 is expressed in molecules $\text{cm}^{-2}\text{s}^{-1}$. Reflecting this notation, Equation (2.4) can then be rewritten as:

$$k_d = v_i \exp(-E_B/T). \quad (2.5)$$

We want to express the desorption rate as a function of temperature, or $R = R(T)$. To do this, we expand the derivative as:

$$R = -\frac{dN_{(s)}}{dt} = -\left(\frac{dN_{(s)}}{dT}\right)\left(\frac{dT}{dt}\right).$$

The second term on the right hand side of Equation (2.6) is the heating rate, an experimental parameter denoted by $dT/dt = \beta$. For this set of experiments, we apply a linear heating ramp of $\beta = 1\text{K min}^{-1} \approx 0.02 \text{ K s}^{-1}$. Therefore, we can express the change in solid phase concentration over temperature (molecules $\text{cm}^{-2} \text{ K}^{-1}$) instead of time as:

$$\begin{aligned} R &= -\frac{dN_{(s)}}{dt} \\ &= -\left(\frac{dN_{(s)}}{dT}\right)(\beta) \end{aligned} \quad (2.6)$$

We can now combine Equations (2.5) and (2.6) to reflect the TPD signal that is actually measured during the experiment:

$$-\frac{dN_{(s)}^i}{dT} = k_d \left(\frac{N_{(s)}^i}{\beta} \right). \quad (2.7)$$

Now we can separate the variables and substitute Equation (2.5) in for $k_d = k_d(T)$ to yield a differential equation for $N_{(s)}$ over temperature:

$$\begin{aligned} \frac{dN_{(s)}^i}{dT} &= - \left(\frac{k_d(T)}{\beta} \right) [N_{(s)}^i] dT \\ &= - \left(\frac{v_i}{\beta} \right) [N_{(s)}^i] \exp(-E_B/T) \end{aligned} \quad (2.8)$$

Separating the variables and integrating this, we obtain an expression for the concentration element N in the solid state as a function of temperature, or $[N_{(s)}] = [N_{(s)}(T)]$. Once we obtain the solid state concentration, we can obtain the desorption rate as a function of temperature since $R(T) = k_d(T)N_{(s)}(T)$.

By definition of desorption, the gas phase concentration is a result of molecules leaving the solid state:

$$\begin{aligned} \frac{dN_{(g)}}{dT} &= - \frac{dN_{(s)}^i}{dT} \\ &= \left(\frac{k_d(T)}{\beta} \right) dT \\ &= \left(\frac{v_i}{\beta} \right) \exp(-E_B/T) \end{aligned} \quad (2.9)$$

Additionally, at each time step of the experiment, a fraction of the molecules that have evaporated into the gas phase will be removed by the pump; subtracting this rate from the desorption into the gas phase will reproduce the experimental conditions. The pump rate is given by:

$$R_p = \frac{dN_{pump}}{dt} = \frac{-dN_{(g)}}{dt} = v_p N_{(g)} \quad (2.10)$$

in which v_{pump} is the pump constant in s^{-1} and $N_{(g)}$ is the number of molecules entering the gas phase having desorbed from a unit surface area (molecules cm^{-2}). Technically, being pumped out of the experimental system is not a chemical state (i.e. solid or gas phase), but since it is a distinct outcome of the system we express the pumped gas with a separate differential equation for comprehensiveness. Meanwhile, we differentiate in notation between experimental and chemical state by not including the pumping subscript p in parentheses. We can use a similar conversion again to obtain the pumped gas as a function of temperature:

$$\begin{aligned}\frac{dN_p}{dt} &= - \left(\frac{dN_{(g)}}{dT} \right) \left(\frac{dT}{dt} \right) \\ &= - \left(\frac{dN_{(g)}}{dT} \right) (\beta)\end{aligned}\quad (2.11)$$

where dT/dt is once again the heating rate, β . Therefore, the final number of molecules in the gas phase of element N in a TPD experiment, $N_{(g)}$ is given as the combination of Equations (2.9) and (2.10):

$$\begin{aligned}\frac{dN_{(g)}}{dT} &= - \frac{dN_{(s)}^i}{dT} - \frac{dN_p}{dT} \\ &= \left(\frac{v_i}{\beta} \right) \exp(-E_B/T) - \left(\frac{v_p}{\beta} \right) N_{(g)}\end{aligned}\quad (2.12)$$

The recorded TPD signal, corresponding to maximum $N_{(g)}$, peaks at some temperature T_d , which in turn corresponds to the point at which the desorption rate from the surface is at a maximum, i.e. $d^2N_{(s)}^i/dt^2 = 0$. To a first approximation, the surface binding energy, E_B , can then be calculated directly by differentiating Equation (2.8) and equating to zero:

$$\frac{E_B^2}{T_d} = \frac{v_i}{\beta} (i) [N_{(s)}]^{i-1} \exp(-E_B/T_d), \quad (2.13)$$

provided that the pre-exponential factor v_i can be estimated. For a first-order reaction, where $i = 1$, v_1 is assumed to be approximately the lattice vibrational frequency of the weak bond

between the adsorbate molecule and the surface ($10^{11} - 10^{13}$ s $^{-1}$), or the attempt frequency. For a zeroth-order reaction, where $i = 0$, the pre-exponential factor is a product of the attempt frequency and the surface density of molecules (of the order 10^{15} molecules cm $^{-2}$). Additionally, it is possible to evaluate the order of the reaction from the TPD peak shape and peak maximum provided that the binding energy and pre-exponential factor remain constant as a function of surface coverage. In practice, however, desorption does not necessarily occur in a single step, the surface binding energy can vary across binding sites on the surface or with surface coverage, and the pre-exponential factor can vary significantly. Therefore, we discuss obtaining the parameter values by modeling the desorption system below and using numerical fitting methods (see Chapter 4) to evaluate the values of v_i and E_B .

2.2 Reaction Order

The model of desorption behavior described above depends on the order of the reaction, which has thus far been denoted with superscript i . Depending on the type of reaction and kinetic process, the reaction order can vary, taking positive, negative, and any non-integer real value. In general, desorption kinetics are not required to have an exact integer value. For instance, the multilayer desorption of CH₃OH on highly oriented pyrolytic graphite has a desorption order of 0.35 (Bolina et al. 2005). In most cases, however, desorption kinetics will approach either zeroth or first order (Bisschop et al. 2005).

2.2.1 Zeroth-Order Kinetics of Multilayer Desorption

In a zeroth-order reaction, the rate of desorption does not depend on the concentration of molecules partaking in the reaction, $[N_{(s)}]$. This is reflected in $i = 0$ substituted into the system described above. Firstly, the desorption rate $R_{i=0}$ is purely an exponential function with no dependence on $[N_{(s)}]$.

$$R_{i=0} = \frac{dN_{(s)}^{i=0}}{dt} = k_d[N_{(s)}]^{i=0} = k_d = v_0 \exp(-E_B/T). \quad (2.14)$$

For a zeroth-order reaction, the pre-exponential factor v_0 is a product of the lattice

vibrational frequency (typically of the order $10^{11} - 10^{13} \text{ s}^{-1}$) and the surface density of molecules (of the order $10^{15} \text{ molecules cm}^{-2}$).

As done above in the general case, we can now solve for the specific reaction rate equation system for molecules undergoing zeroth-order desorption. Again using the conversation to temperature:

$$R_{i=0} = \frac{dN_{(s)}^{i=0}}{dt} = \left(\frac{dN_{(s)}^{i=0}}{dT} \right) \left(\frac{dT}{dt} \right) = \left(\frac{dN_{(s)}^{i=0}}{dT} \right) (\beta) = k_d$$

where $\beta = 0.02 \text{ K s}^{-1}$ is again the heating rate. We do not have to integrate to find the desorption rate, since we can simply express $k_d = v_0 \exp(E_B/T)$ as a function of temperature. We can substitute this into Equation (2.14) to obtain an expression for the TPD signal:

$$-\frac{dN_{(s)}}{dT} = -\left(\frac{v_0}{\beta} \right) \exp(-E_B/T). \quad (2.15)$$

In this case, integrating is relative straightforward since this equation is separable, i.e.:

$$N_{(s)} = - \int \left(\frac{v_0}{\beta} \right) \exp(-E_B/T) dT$$

Meanwhile, to calculate the gas phase concentration, we integrate in order to incorporate the pumping effects, which are independent of reaction order:

$$\begin{aligned} \frac{dN_p}{dt} &= v_p N_{(g)} = - \left(\frac{dN_{(g)}}{dT} \right) \left(\frac{dT}{dt} \right) \\ &= - \left(\frac{dN_{(g)}}{dT} \right) (\beta). \end{aligned} \quad (2.16)$$

As explained in the general model above, the change in number of gas phase molecules $N_{(g)}$ over temperature is the difference been the change in solid state molecules and pumped gas, but we now account for the zeroth-order behavior:

$$\begin{aligned}\frac{dN_{(g)}^{i=0}}{dT} &= -\frac{dN_{(s)}^{i=0}}{dT} - \frac{dN_p^{i=0}}{dT} \\ &= \left(\frac{v_0}{\beta}\right) \exp(-E_B/T) - \left(\frac{v_p}{\beta}\right) N_{(g)}^{i=0}.\end{aligned}\quad (2.17)$$

Integrating Equation (2.17) yields the number of molecules in the gas phase of element $N_{(g)} = N_{(g)}(T)$ undergoing zeroth-order desorption. As the differential equation for desorption rate (Equation (2.14)) and number of gas phase molecules (Equation (2.17)) reflect, the desorption behavior is independent of the initial concentration of solid state molecules on the substrate.

2.2.2 First-Order Kinetics of Monolayer Desorption

In a first-order reaction, the desorption behavior depends on the concentration of molecules on the surface, in contrast with zeroth-order kinetics. In this case, the equations are given as those above in the general case, but with $i = 1$. The rate of desorption, $R_{i=1}$ depends linearly on the solid state concentration:

$$R_{i=1} = \frac{dN_{(s)}^{i=1}}{dt} = k_d[N_{(s)}]^{i=1} = k_d[N_{(s)}] = v_1[N_{(s)}] \exp(-E_B/T). \quad (2.18)$$

The solid state abundance, $N_{(s)}^{i=1}$ is a function of its initial concentration:

$$\begin{aligned}-\frac{dN_{(s)}^{i=1}}{dT} &= k_d \left(\frac{[N_{(s)}]^{i=1}}{\beta} \right) \\ &= -\left(\frac{v_1}{\beta}\right) [N_{(s)}]^{i=1} \exp(-E_B/T) dT\end{aligned}\quad (2.19)$$

which we in turn separate and integrate to obtain $N_{(s)}^{i=1}$. The pumping is again independent of reaction order, and is the same as in the zeroth-order case (Equation (2.16)). As such, the number of molecules in the gas phase undergoing first-order desorption is given as:

$$\begin{aligned}\frac{dN_{(g)}^{i=1}}{dT} &= -\frac{dN_{(s)}^{i=1}}{dT} - \frac{dN_p}{dT} \\ &= \left(\frac{v_1}{\beta}\right) [N_{(s)}^{i=1}] \exp(-E_B/T) - \left(\frac{v_p}{\beta}\right) N_{(g)}^{i=1}.\end{aligned}\quad (2.20)$$

2.2.3 Combining Kinetics of Different Reaction Order

Chemical models often consider ice desorption to be a first order process; however, desorption has been experimentally found to be a zeroth-order process with respect to total ice abundance for ices thicker than one monolayer (Bisschop et al. 2006). Moreover, if the entire ice is assumed to undergo first-order desorption in respect to the total solid state concentration, this implies that all molecules at all points in the ice are allowed to desorb simultaneously, which is non-physical (Fraser et al. 2001; Bisschop et al. 2006). Therefore, we first consider the three-phase model of astrophysical ices, first introduced by Hasegawa & Herbst (1993). This three-phase model treats the bulk and surface (outermost layer of accreted material) of the ice as separate phases in addition to the gas phase. Previous models treated all layers of the ice as the surface and were assumed to be indistinguishable regarding reactivity. In the three-phase model, molecules are only allowed to desorb from the surface, which is continuously replenished by molecules coming from the top mantle layer below, and the unexposed mantle is otherwise non-reactive. As such, the rate of desorption should not depend on the concentration of surface molecules, since the evaporated molecules are immediately replaced, until the bottom layer is reached. A family of three-phase models has been applied to several ice desorption laboratory experiments, namely Pontoppidan et al. (2003) and Pontoppidan et al. (2005) for CO ice desorption and by Collings et al. (2005), and has accurately reproduced zeroth-order desorption behavior for ices thicker than one monolayer.

In this thesis, we extend the three-phase model to four phases, motivated by conceptual understanding of ice desorption at low surface coverages. In addition to the gas phase, we distinguish between the surface, mantle, and final monolayer in the solid state, resulting in four distinct desorption phases. This four-phase model is conceptually represented in Figure

2.1. As with the three-phase model, we consider a multilayer ice sample to undergo zeroth-order desorption with a reactive surface phase and a non-reactive mantle, which continuously replaces evaporated molecules. This molecule replacement process continues throughout the ice mantle until the final monolayer is reached. At the final monolayer, we diverge from previous models and consider monolayer ice desorption to be first-order, resulting in a distinct phase. This change in reaction order is because there are no molecules underneath the final monolayer to replace evaporated molecules, hence the reaction is constrained by the concentration of molecules in the solid state. In other words, the desorption rate will decrease as the number of molecules in the solid state involved in the desorption reaction decrease and are not replaced in the monolayer.

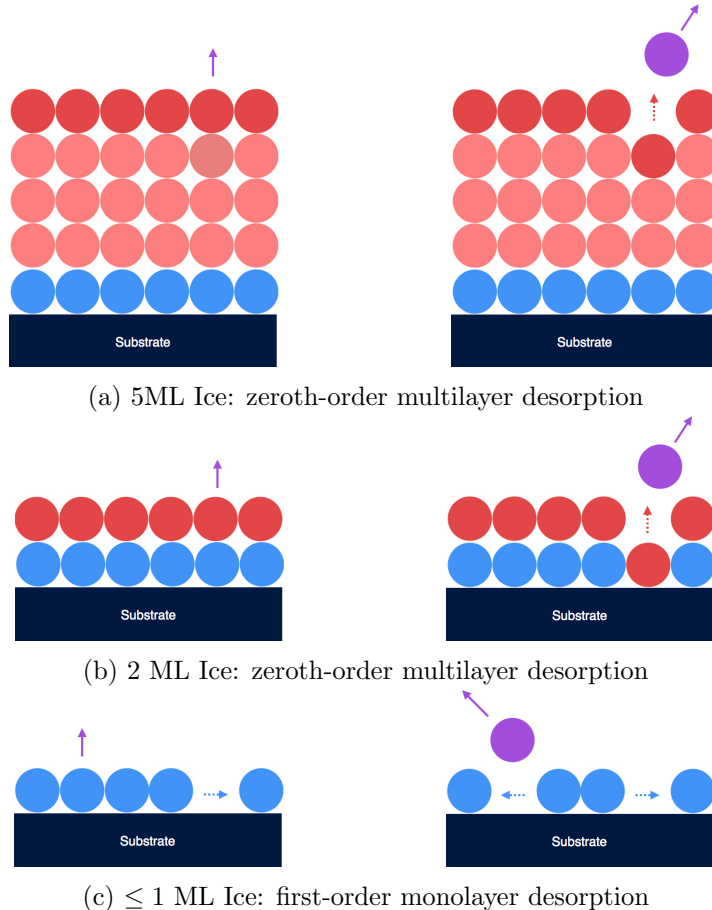


Figure 2.1: *Four-Phase Chemical Model of Ice Desorption*: To illustrate the chemical model, we consider an example of a 5 ML ice. The four phases are as follows: ¹. a reactive surface of 1 ML (shown in dark pink), ². a non-reactive mantle of 3 ML (shown in light pink), ³. an eventually reactive, initially non-reactive, monolayer of 1 ML (shown in light blue), and ⁴. desorbed molecules in the gas state (shown in purple). The left figures of (a), (b), and (c) represent the ice before the desorption event, and the corresponding right figures represent the ice immediately after the desorption event of the molecule in gas state. When the ice is 5 ML before desorption (left (a)), only the surface layer is reactive. When a molecule desorbs (right (a)), it is immediately replaced by the molecule directly below it on the exposed mantle, which in turn becomes part of the reactive surface. This replenishment process continues throughout the mantle, implying that the desorption rate is independent of the number of molecules initially on the solid surface, hence resulting in zeroth-order kinetics. When the ice has a coverage of 2 ML (left (b)), there is no non-reactive mantle and only a reactive surface and a monolayer. This is the last stage at which the desorbed molecule replenishment process can occur, as shown in (right (b)), and thus is the end of zeroth-order kinetics. When the ice is a monolayer or less (left (c)), the final molecules become reactive. However, since there are no molecules to replace desorbed molecules from the monolayer (right (c)), the rate of desorption becomes dependent on how many molecules there are left on the surface, or the solid state concentration, implying first-order kinetics.

With this model, the solid state ice consists of both the multilayer (consisting of both the reactive surface and the non-reactive mantle) and the monolayer:

$$[N_{(s)}] = [N_{(s)}]^{ice} + [N_{(s)}]^{ml} \quad (2.21)$$

where the *ice* superscripts denote the multilayer and the *ml* subscripts denote the monolayer.

It follows that:

$$\begin{aligned} \frac{dN_{(s)}}{dT} &= \frac{dN_{(s)}^{ice}}{dT} + \frac{dN_{(s)}^{ml}}{dT}, \\ &= -\left(\frac{v_0^{ice}}{\beta}\right) \exp(E_B^{ice}/T) - \left(\frac{v_i^{ml}}{\beta}\right) [N_{(s)}^{ml}] \exp(-E_B^{ml}/T), \end{aligned} \quad (2.22)$$

reflecting the zeroth-order desorption of the multilayer and the first-order desorption of the monolayer. Substituting this into Equation (2.9), we obtain:

$$\begin{aligned} \frac{dN_{(g)}}{dT} &= -\frac{dN_{(s)}}{dT} - \frac{dN_p^{i=0}}{dT}, \\ &= -\frac{dN_{(s)}^{ice}}{dT} - \frac{dN_{(s)}^{ml}}{dT}, \\ &= \left(\frac{v_0^{ice}}{\beta}\right) \exp(E_B^{ice}/T) + \left(\frac{v_i^{ml}}{\beta}\right) [N_{(s)}^{ml}] \exp(-E_B^{ml}/T) - \left(\frac{v_p}{\beta}\right) N_{(g)}. \end{aligned} \quad (2.23)$$

As the coupled differential equation system is evolved through temperature, the desorption behavior is sequential: i.e. we solve the zeroth-order multilayer differential equation until the bottom layer is reached, then we switch to solving the first-order monolayer differential equation. The reactions and their corresponding rate equations are given in Table 2.1.

2.3 Computational Simulations of Desorption

To simulate desorption under the four-phase chemical model described above, integration of the coupled differential equation system above was done using the Python `odeint` function from

Description	Reaction	Rate Equation	i
Multilayer Desorption	$N_{(s)}^{ice} \rightarrow N_{(g)}$	$v_0^{ice} \exp(-E_B^{ice}/T)$	0
Monolayer Desorption	$N_{(s)}^{ml} \rightarrow N_{(g)}$	$v_1^{ml} [N_{(s)}^{ml}] \exp(-E_B^{ml}/T)$	1
Pumped Gas	$N_{(g)} \rightarrow N_p$	$v_p [N_{(g)}]$	1

Table 2.1: *Experimental Desorption Model*: The rate equations for the desorption of the multilayer, desorption of the monolayer, and removal of gas via pumping are given for their corresponding reactions. The reaction order, i , is denoted in the last column.

the `spicy.integrate` module. The TPD curve is generated as the temporal evolution of these coupled differential equations as the system temperature is raised in a linear manner. The required inputs to the computer model are the temperature range, thickness of the ice, the binding energies, and pre-exponential factors. The temperature range is an experimental parameter, in this thesis ranging from 15 to 60 K, and can be adjusted to the TPD range of interest. The surface coverage inputted into the model as an initial condition of the differential equation system. We allow for the binding energy and the pre-exponential factor to differ between the multilayer E_B^{ice} , v_0^{ice} and the monolayer E_B^{ml} , v_1^{ml} (i.e. four separate parameters), to more accurately reflect the changes in kinetic behavior between the two phases distinctly considered by our model and observed in laboratory experiments. The computer model evolves the coupled differential equation system through an increasing temperature range under zeroth-order desorption kinetics until the final monolayer is reached, upon which the differential equation system is evolved under first-order desorption kinetics until all of the initial solid state ice has been evaporated and there is no material left. Figure 2.2 shows the kinetic characteristics of zeroth-order desorption, as produced by the computer model. The upper left panel, Figure 2.2a mirrors the upper right panel, Figure 2.2b, displaying the evaporation of the solid ice into the gas phase. In particular, the upper right panel of gas phase concentration over temperature shows an exponentially decreasing leading edge followed by a sharp drop off as the gas is pumped out of the system, a characteristic of zeroth-order desorption where the gas phase concentration is an exponential function independent of solid state concentration (Equation (2.17)). The decline in gas phase

concentration is in turn explained by the gas pumped out of the experimental chamber, as shown in Figure 2.2c. Meanwhile, the desorption rate, shown in Figure 2.2d equals the rate constant in zeroth-order desorption, and is similarly an exponential independent of the solid state concentration.

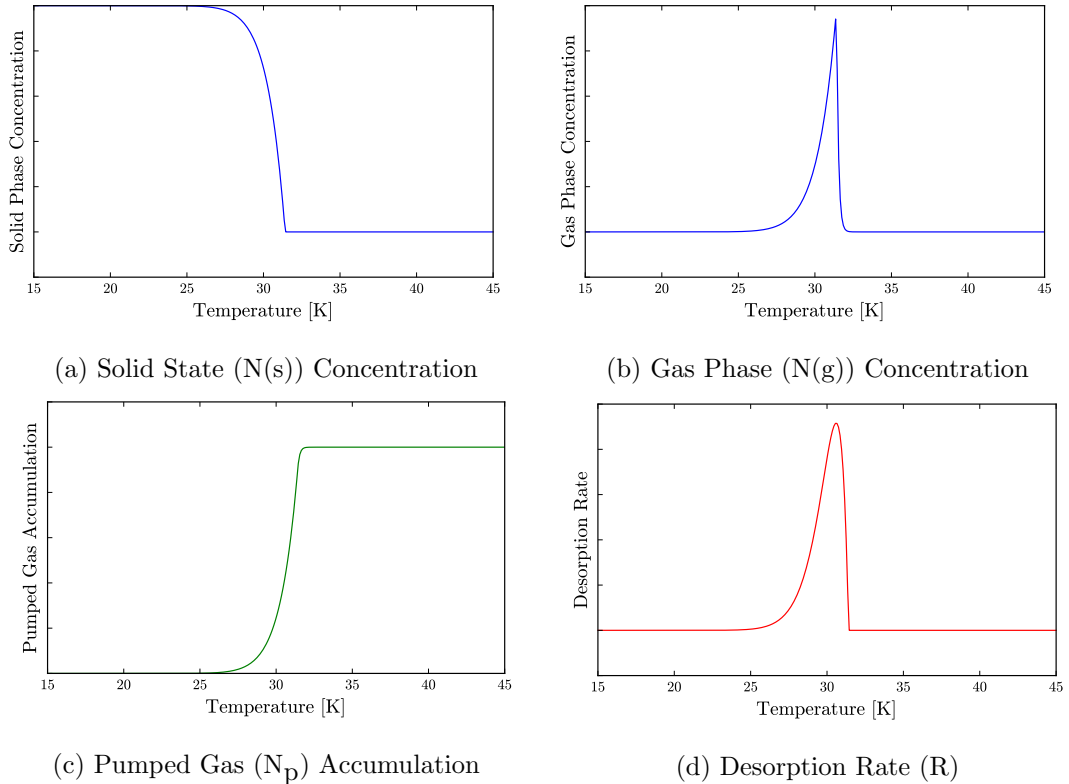


Figure 2.2: *Modeling Zeroth-Order Desorption*: In the upper left panel, we see the decline in the solid phase concentration as molecules evaporate into the gas phase. This corresponds to the exponential increase in the gas phase concentration with the onset of desorption, as shown in the upper right panel. The sharply exponential leading edge is characteristic of a zeroth-order desorption profile, reflecting the functional and kinetic independence from the solid state concentration. The gas phase concentration decreases as the pump removes gas from the experimental system, as shown in the lower left panel. The desorption rate, similarly exponential and independent of the solid state concentration, is shown in the lower right panel.

Figure 2.3 shows the desorption kinetics of the general case of a multilayer on top of a monolayer of ice, as produced by the computer model. The upper left panel, Figure 2.3a, shows desorption curves of ices of surface coverages of 10 ML, 5 ML, and 2 ML. We see that the multilayer desorbs first, exhibiting the sharp exponential profile characteristic of zeroth-order desorption. In particular, we see that the leading edges align between the desorption curves

of the multilayer, suggesting that desorption occurs at a rate independent of surface coverage, consistent with zeroth-order desorption. Additionally, we see the distinct desorption of the monolayer following the multilayer desorption curve. The monolayer desorption curves are more rounded, and the leading edges do not align. To examine first-order monolayer desorption more closely, we modeled the desorption of monolayer, 1 ML and sub-monolayer 0.5 ML and 0.25 ML ices in Figure 2.3b. In contrast to multilayer desorption, we see that the onset of desorption shifts with decreasing surface coverage, and the leading edges do not align, resulting in a distinct first-order desorption curve morphology. This suggests that the desorption rate increases with increasing ice thickness, consistent with first-order kinetics. Moreover, the peaks of the desorption curves all align in first-order desorption, in contrast with zeroth-order desorption. In Figure 2.3c, we examine a 5 ML ice as the values of the binding energies increase in magnitude, while the binding energy differential $\Delta E_B = E_B^{ml} - E_B^{ice}$ is kept constant at 200 K. The multilayer binding energy is the binding energy of the molecule to itself, $E_B^{ice} = E_B^{ice}(\text{CO} - \text{CO})$ or $E_B^{ice} = E_B^{ice} = (\text{N}_2 - \text{N}_2)$, whereas the monolayer binding energy is the binding energy of the molecule to the substrate, $E_B^{ml} = E_B^{ml}(\text{CO} - \text{H}_2\text{O})$ or $E_B^{ml} = E_B^{ml} = (\text{N}_2 - \text{H}_2\text{O})$. Consequently, the binding energy of the monolayer captures the effect of substrate changes. We see that with increasing binding energy values, the curves shift to higher temperatures, consistent with our understanding of binding energy as a reaction barrier. The temperature difference between the multilayer and monolayer peaks does not change, consistent with the constant binding energy differential. In Figure 2.3d, we vary the pump rate for a 5 ML ice to examine how sensitive the gas concentration and desorption timescale are to the experimental parameter.

The overall desorption behavior of the ice sample is determined by the relative effects of zeroth- and first-order reactions, which in turn depends both on the difference in the reaction barriers (i.e. binding energies) of the desorption processes and the thickness of the multilayer relative to the monolayer. The binding energy of the monolayer, E_B^{ml} molecules to the substrate is generally greater than the binding energy of the multilayer molecules, E_B^{ice} to molecules of the same species due to the direct contact and lack of competition for the binding sites on the substrate for weakly interacting species such as CO and N₂. As the binding energy of the monolayer increases relative to the multilayer, desorption will be delayed until the higher

reaction barrier is reached with increasing temperature, resulting in a bifurcated desorption profile, with a monolayer feature separate from the multilayer feature at a higher temperature. The relative difference between the zeroth- and first-order desorption onsets depends on the binding energy differential. Meanwhile, the relative heights of the multilayer desorption curve and the monolayer desorption curve depends on the relative thicknesses of the multilayer relative to the monolayer. The effects of relative thickness and binding energy differential are examined in Figure 2.4. In all four panels of Figure 2.4, the binding energy differential, $\Delta E_B = E_B^{ml} - E_B^{ice}$, is increased from 0, to 200, to 400 K. In Figure 2.4a, we consider a relatively thick ice of 10 ML (i.e. surface of 1 ML, mantle of 8 ML, and monolayer of 1 ML). Due to the relative thickness of the monolayer, the multilayer desorption curve dominates the overall profile across all three binding energy differentials. For a binding energy differential of 0 K, as shown in blue, the desorption of the monolayer occurs at the same temperature of the multilayer. Due to this and the relative thickness of the ice, the monolayer desorption feature is absorbed completely by the multilayer peak. For a binding energy differential of 200 K, we see that the multilayer still dominates the desorption process, but a small monolayer feature is absorbed at approximately 33 K. The peaks are separated relative to the $\Delta E_B = 0$ K peak, and the separation increases as the binding energy differential increases to 400 K, as shown in green. The binding energy differential is now sufficiently large such that the monolayer desorption curve is a completely distinct feature, albeit much smaller than the multilayer desorption curve due to the thickness of the ice. In Figure 2.4b, we decrease the surface coverage to 5 ML (i.e. surface of 1 ML, mantle of 3 ML, and monolayer of 1 ML). Again for a binding energy differential of $\Delta E_B = 0$ K, the monolayer feature is completely absorbed into the multilayer feature. For binding energy differentials of 200 K and 400 K, we see desorption curves similar to those of the 10 ML ice, but the monolayer feature is more prominent due to the thinner ice. In Figure 2.4b, we consider a 2 ML ice (i.e. surface of 1 ML, no mantle, and monolayer of 1 ML). Although the “multilayer” here is 1 ML over the monolayer, we will continue to refer to it as the multilayer for conceptual consistency. Close observation of the $\Delta E_B = 0$ K curve in blue shows that the profile is not completely symmetrical and has a slight right shoulder. Although the binding energies are the same, the monolayer is emerging slightly from the multilayer peak. In the $\Delta E_B = 200$ K and

$\Delta E_B = 400$ K curves, the monolayer peak is prominent in the overall profile and comparable in height to the multilayer peak. Similarly, an increasing binding energy differential results in a greater temperature difference between the onset of the multilayer and the monolayer desorption curves. Lastly, in Figure 2.4d, we consider a 1.25 ML ice, where the multilayer is 0.25 ML on a monolayer (i.e. a sub-monolayer surface of 0.25 ML, no mantle, and a monolayer of 1 ML). Again, we refer to the 0.25 ML surface as a “multilayer” for consistency, even though its actual thickness is less than 1 ML. Across all three binding energy differentials, we see that the multilayer feature is less prominent than the multilayer, reflecting relative thickness. We note that despite a binding energy differential of $\Delta E_B = 0$ K, the blue desorption curve appears to be the blend of a zeroth-order left shoulder and a taller first-order right shoulder. Although the binding energy differential effect here is absent, the relative thickness differential still results in a bifurcated desorption curve. The zeroth-order multilayer and first-order monolayer features become increasingly distinct as the binding energy differential is increased. In contrast with the previous surface coverages, the prominence of the multilayer and monolayer curves are reversed now that the monolayer is relatively thicker.

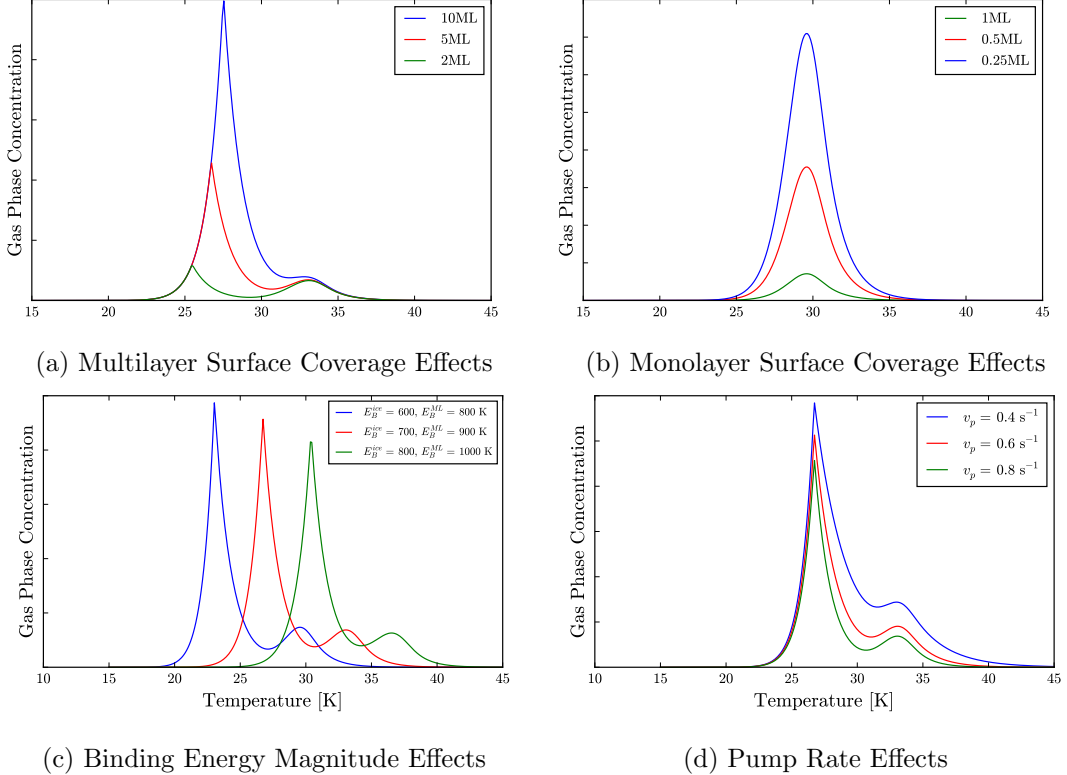


Figure 2.3: *Modeling Multilayer and Monolayer Desorption:* In the upper left panel, the surface coverage is varied between 2, 5, and 10 ML. We see the characteristically aligned leading exponential edges of the multilayer desorption curves, implying independence from solid state concentration, consistent with zeroth-order desorption. We also observe distinct desorption profiles for the monolayer. In the upper right panel, we examine the effects of surface coverage on monolayer desorption by examining sub-monolayer thicknesses. We note that the desorption curves have a different morphology, as the onset of desorption shifts to higher temperatures with decreasing surface coverage, but the peaks align. This implies that the desorption rate is an increasing function of surface coverage, consistent with first-order kinetics. In the lower left panel, we maintain the binding energy differential at $\Delta E_B = 200$ K for a 5 ML ice, but increase the magnitudes of E_B^{ice} and E_B^{ml} . The curves shift to higher temperatures with increasing binding energy values, consistent with our interpretation of the binding energy as a reaction barrier, and the temperature difference between the multilayer and monolayer desorption curves is maintained, consistent with the constant binding energy differential. In the lower right panel, we see how the gas phase concentration of a 5 ML ice responds to increases in the experimental pumping rate.

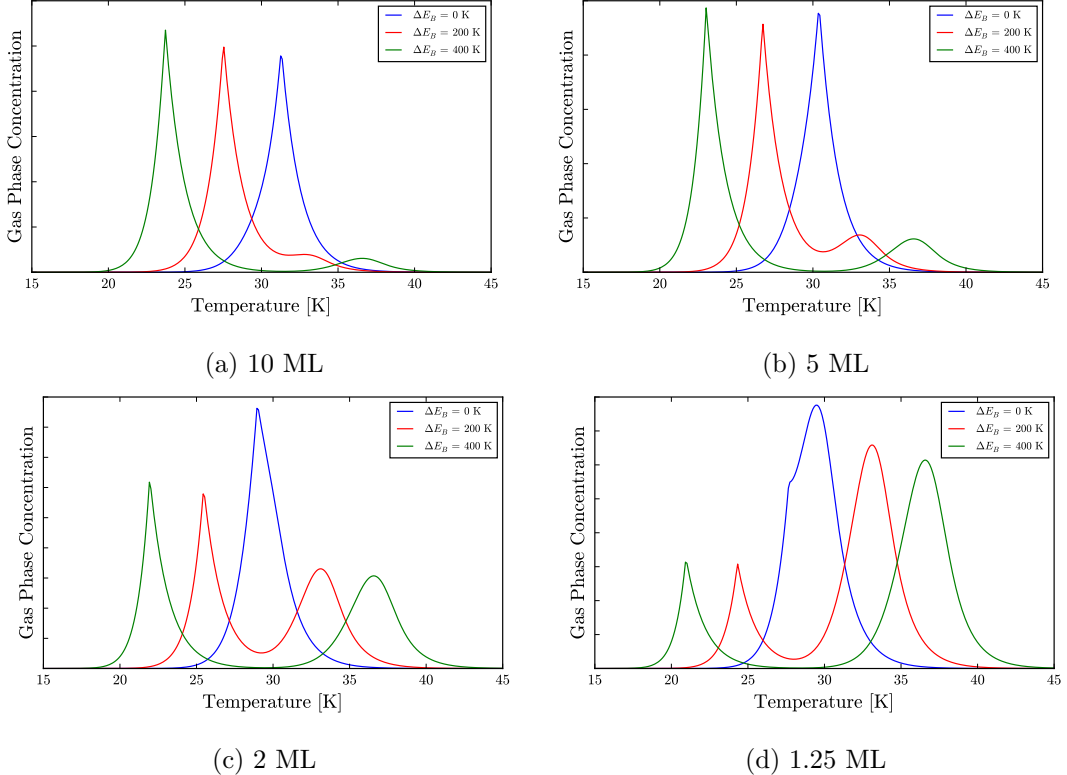


Figure 2.4: *Relative Effects of Surface Coverage and Binding Energy Differentials:* The upper left panel models the desorption of a relatively thick 10 ML ice (i.e. surface of 1 ML, mantle of 8 ML, and a 1 ML monolayer) across binding energy differentials of $\Delta E_B = 0, 200$, and 400 K. With increasing binding energy differential, the monolayer feature becomes more distinct in the overall desorption profile, but is still relatively small due to the thickness of the multilayer. While the monolayer becomes more relatively visible in the 5 ML case (i.e. surface of 1 ML, mantle of 2 ML, and a 1 ML monolayer), the multilayer desorption peak dominates the general desorption process. Meanwhile, in the 2 ML case, we see that the $\Delta E_B = 0$ K curve (blue) develops a slight right shoulder, indicating the monolayer desorption. In the non-zero binding energy differential cases, we see that the multilayer and monolayer features are comparable, reflecting the effect of equal thickness, and their separation increases, reflecting the effect of increasing binding energy differential. For the 1.25 ML case in the lower right panel, we have a multilayer with surface coverage of 0.25 ML over a monolayer, reversing the relative thicknesses from the upper row. For the $\Delta E_B = 0$ K (blue) curve, we see a zeroth-order multilayer left shoulder and a first-order monolayer right shoulder, with the monolayer predominant. For the $\Delta E_B = 200$ K (red) and $\Delta E_B = 400$ K (green) curves, we see that the separation of the multilayer and monolayer features again increases with binding energy differential; however, we see that the relative prominence of the features has reversed, reflecting the effects of relative thickness. In all four surface coverages, we observe the characteristic zeroth-order and first-order desorption morphologies for the multilayer and the monolayer, respectively.

Chapter 3

Ice Desorption Theory

In this chapter, we present new experiments on CO and N₂ desorption from pure ices and different H₂O ices. We vary ice thicknesses, H₂O ice porosity, and ice morphologies. Temperature programmed desorption (TPD) is used to probe the segregation, kinetic, and desorption processes in these ices. The aim of these experiments is to understand and quantify the relative desorption behavior of CO and N₂ ices in situations involving H₂O ice in astrophysically relevant environments.

3.1 Experimental Methods

3.1.1 Experimental Set-Up

The desorption experiments were carried out in a laboratory set-up designed to simulate interstellar ices, illustrated in Figure 3.1 and is described in further detail in Lauck et al. (2014). The apparatus consists of a 13-inch spherical stainless steel ultrahigh vacuum (UHV) chamber (custom-made, Pfeiffer Vacuum), evacuated by a Pfeiffer Turbo HiPac 400 pump backed by a DUO 10M rotary vane pump to a base pressure of $\sim 10^{-10}$ mbars at room temperature. The gases are deposited and grown on a 2 mm thick IR transparent CsI substrate with a 19 mm clear view, mounted on an nickel plated optical ring sample holder at the center of the chamber with silver gaskets for maximum thermal contact. The temperature of the sample holder is controlled via thermal contact with a connected closed cycle He cryostat (Model CS204B, Ad-

vanced Research Systems, Inc.), connected to the CsI by a cold tip. On this cold tip is a 50 ohm thermofoil heater, which allows the temperature of the CsI substrate to vary between 12 – 350 K. The cryostat cold head is installed on the top port of the UHV chamber, held in place by a UHV rotary seal (Thermionics RNN-40), which allows 360 degree rotation of the CsI substrate inside the chamber towards the gas doser or either the infrared system or mass spectrometer. In this study, the experimental temperatures ranged from 14 to 180 K. The substrate temperature is regulated by a temperature controller (Lakeshore Model 335), externally controlled using a calibrated (accuracy of 0.1 K) KP-type silicon diode temperature sensor (0.07% Au in Fe versus chrome) mounted directly onto the face of the CsI substrate.

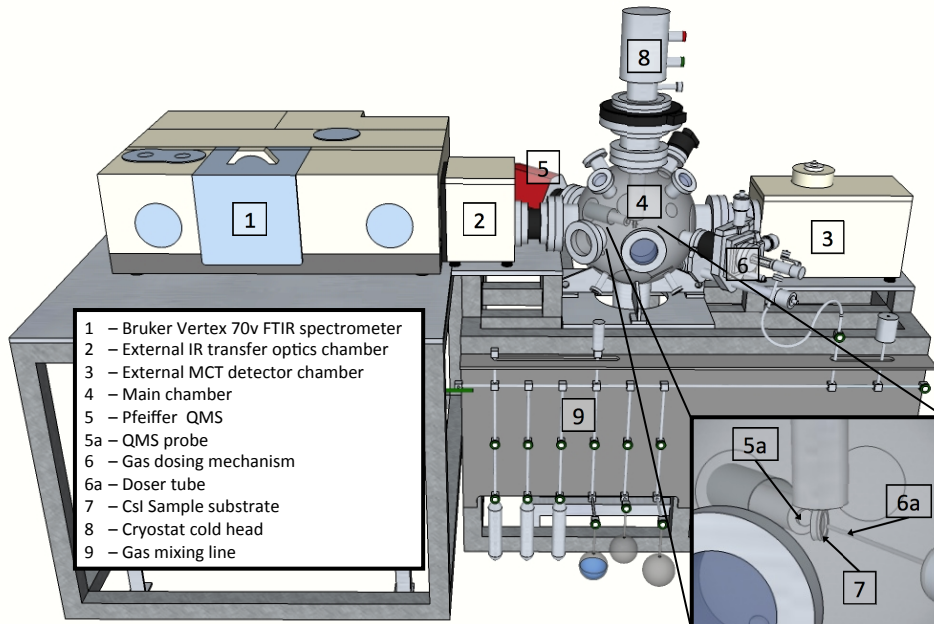


Figure 3.1: *Astrochemistry Laboratory Setup*: The primary experimental apparatus is located in the Öberg group laboratory in the Harvard-Smithsonian Center for Astrophysics. The main chamber (4), is where the gases are deposited and the ices are grown and then desorbed. The quadrupole mass spectrometer (5) measures the gas composition, and the infrared spectra are collected in (3).

Both infrared and mass spectrometry data is collected throughout the TPD experiments. The mass spectrometer, the external interferometer chamber and the MCT detector chamber are evacuated to 2 mbar to avoid atmospheric interference with the ice spectra. The infrared detection system consists of two external chambers, the first being a Bruker Vertex 70v spectrometer which originates the infrared beam, and the second being an external MCT detector

chamber which receives the beam as it exits from the UHV chamber. Ice composition, thickness and morphology are monitored through infrared absorption transmission spectroscopy at $4000 - 400\text{cm}^{-1}$ and is collected with external OPUS software. The infrared beam from the spectrometer is focused onto the CsI chamber and recessed into the MCT detector through KBr ports on each side of the UHV chamber using two sets of transfer optics (flat and off-axis paraboloidal mirrors) in each of the two external chambers. The spectra reported in this thesis have a resolution of 1cm^{-1} and have been background subtracted.

Additionally, a Pfeiffer quadrupole mass spectrometer (QMS 220M1, mass range 1-100 amu, and resolution of 0.5 amu) is positioned 40 mm off the CsI substrate. It is used to continuously monitor the gas composition during ice growth and warm-up of the deposited ices. The mass spectrometer also collects temperature data, which is used to verify the measurements from the temperature controller. As mentioned previously, the CsI substrate is allowed to rotate, enabling face-on detection and measurement by both the IR and mass spectrometers, as schematically represented in Figure 3.2. The UHV rotary seal is differentially pumped, allowing the CsI substrate to rotate without breaking the vacuum.

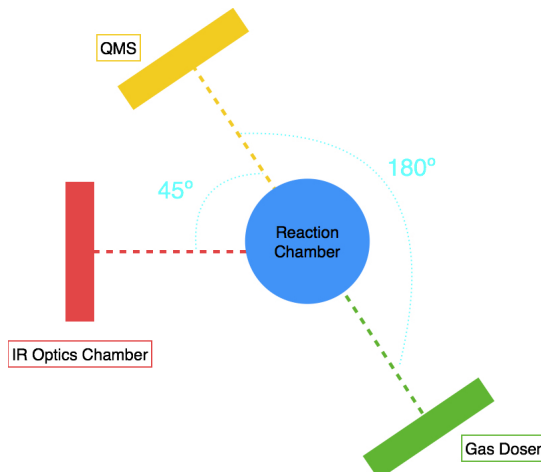


Figure 3.2: *Rotating Experimental Setup:* The substrate is located in a vacuum-sealed chamber mounted on a rotary seal, which allows the chamber to be rotated without chemical contamination. The gas doser is positioned at 0 degrees, the QMS at 180 degrees, and the infrared detector at 225 degrees. With this rotation mechanism, the substrate can be positioned face-on to any of these instruments of interest. During the gas deposition, the substrate is rotated to 0 degrees to face the doser, then during the experiment is rotated 180 degrees to face the QMS. During spectra collection, the substrate is rotated 225 degrees to face the infrared optics chamber.

The ultra-high vacuum is maintained by a system of mechanical and turbomolecular pumps. The mechanical (oil) pumps operate at atmospheric pressures, and consist of non axial rotors. At lower pressures, the turbomolecular pumps reach the ultra-high vacuum level by employing multiple stages of rotor pairs in series.

Ices are grown *in situ* by exposing the cooled CsI substrate to a constant flow of gas along the surface normal from an independently pumped gas-line (base pressure lower than 10^{-5} mbar) using a gas doser consisting of an xyz stage positioned 80mm from the substrate window, a precision leak valve (MDC vacuum), a deposition tube (4.8 mm diameter, 14 inches long). The deposition tube is connected to a gas-mixing line, which is differentially pumped down to 5×10^{-4} Torr, monitored with baratron and pirani gauges. The line contains various ports for glass bulb vessels or stainless steel canisters, which can be interchanged as needed, and several on/off valves, one of which allows the gases to flow to the precision leak valve of the gas doser. Deposition is monitored in real-time with the mass spectrometer, to ensure that residual molecules are not present during ice growth.

3.1.2 Experimental Procedure

To enable CO and N₂ to be discriminated from each other (and the background signal) with mass spectrometry, isotopes of both molecules were used. The experiments were carried out with ¹³CO (Icon Isotopes 99.998% *m/e* = 29), ¹⁵N₂ (Cambridge Isotope Laboratory Inc. 98% *m/e* = 30), and deionized water (99.9%, Cambridge Isotope Laboratory Inc.). This isotopic substitution is simply an experimental asset and does not affect the results presented: ¹²CO and ¹⁴N₂ would behave identically.

Chemical Preparation and Deposition

In the pure and layered morphologies, the gases were used as supplied and were prepared by filling a bulb on the gas-mixing line to a pressure of 10 mbar. A 1:1 ¹³CO:¹⁵N₂ gas mixture were prepared by adding species sequentially to one of the bulbs at the correct proportions, estimated using the pressure gauges and the known volumes of the different bulbs and tubes within the gas mixing line. This mixture preparation procedure enabled deviations less than 15% from target

proportions, based on QMS measurements. The deionized water samples were purified by three freeze-thaw cycles under vacuum. The dosing rate for ice-film growth was set prior to cooling the sample by sequentially backfilling the chamber with the gas(es) of interest, to a pressure of $\sim 1 \times 10^{-8}$ Torr, equivalent to an ion reading on the mass spectrometer of 7.5×10^{-10} A for both $^{15}\text{N}_2$ and ^{13}CO . The flow was then stopped, and the background pressure within the chamber was allowed to recover to $\approx 1 \times 10^{-10}$ Torr, before the sample was cooled to 14 K.

The CsI window was then cooled to the desired deposition temperature, followed by the introduction of a sequence of gases or gas mixtures to build up a layered ice structure. The deposition tube was kept close to the surface to maintain a highly controlled porosity structure of the deposited ices. An H_2O ice substrate was created by cooling the sample to the desired deposition temperature (100, 70, or 14) K, and then liberating the deionized water to grow a comparably thick layer of controlled porosity. The deposition of H_2O was followed by a flash heating sequence to 160 K (5 K/min), followed by cooling to 14 K for the deposition of the subsequent gas(es). The gas ice films were grown by reopening the preset flow valve for exposure times equivalent to the gas dose required per sample gas, according to the morphology of the ice to be grown, assuming 1 L (Langmuir) is $\approx 1 \times 10^{-6}$ Torr s, which roughly corresponds to ~ 1 monolayer per unit area of material on the substrate, assuming 1×10^{15} molecules cm^{-2} . The ice layer thicknesses were quantified using the infrared spectra (acquired normal to the sample) of the deposited ice and band strengths and ice densities from the literature, correlated with the integrated TPD and dosing QMS measurements.

Infrared Spectral Band Analysis

Infrared spectra were obtained to determine the thickness of the ice sample and monitor the ice composition. Pure CO has a distinct Lorentzian band profile centered at 2139 cm^{-1} (Bouwman et al. 2007). Since N_2 has no permanent dipole, it is infrared inactive and can only be monitored via mass spectrometry. Repeated infrared spectral measurements were taken during film growth to record the CO gas uptake on the cold substrate, then a single IR spectrum was acquired immediately after each deposition of a CO ice film to determine the surface coverage of the resulting ice film. These deposition spectra were followed by repeated infrared spectra mea-

Species	IR band	Int. range (cm^{-1})	A_{band} (cm molec^{-1})	ρ (g cm^{-3})
CO	C-O str.	2120 – 2170	1.1×10^{-17}	0.81

Table 3.1: CO ice infrared and density literature values

surements throughout the desorption experiment, taken every two minutes with 128 scans per spectrum, which were combined with QMS measurements to detect residual gas. Background infrared spectra were acquired both prior to ice growth and the start of heating and subtracted from corresponding spectral measurements automatically by the OPUS software. To further reduce the spectra, a second-order polynomial baseline fit was automated using the Python `polyfit` and `polyval` functions and applied to all acquired background and sequential spectra. The fitting procedure worked generally well due to the flat quality of the baseline and high signal-to-noise ratio. Isotope features were occasionally observed and were selectively excluded from the spectral reduction process.

The ice thicknesses were initially estimated from the deposition flow and time as monitored by the QMS, but then precisely calculated with the single spectrum taken normal to the sample collected immediately after deposition. The single infrared spectrum taken immediately following ice deposition is used to determine the surface coverage in monolayers of the resulting ice film. Using literature values of band strength and ice densities (Table 3.1, Gerakines et al. 1995) we could first convert the absorbance units of the infrared spectra output into absorbance in terms of monolayers.

Assuming a surface concentration of 10^{15} molecules cm^{-2} , the infrared absorbance units, N , can be converted into n_{IR} monolayers absorbance by the product of the band strength and surface concentration:

$$n_{IR} = \frac{N}{A_{band} \times 10^{15}}$$

This monolayer absorbance, n_{IR} was then compared to the integrated area of the desorption curve in all pure CO experiments, allowing us to obtain a conversion factor equal to the coefficient of the linear correlation, i.e.:

$$n_{IR} = X \times TPD_{area} + \text{residual}$$

With this conversion factor, X , derived from pure CO infrared spectra, the surface coverage of an ice film can be determined from integrating the area of the resulting TPD curve to obtain TPD_{area} , multiplying by the correlation coefficient, and obtaining a monolayer surface coverage, n_{IR} . This conversion is also applied to the integrated area of the TPD curves from N_2 ice samples, allowing surface coverages to be determined despite the inability to observe N_2 in the infrared. This calculated surface coverage is later inputted into the kinetic model to determine the relative effects of zeroth- and first-order desorption and to provide the initial solid state abundance conditions. The measured infrared spectra and their corresponding surface coverages are shown in Figure 3.3. Additionally, this enables us to calculate the thickness of N_2 ices, since we can calculate the expected surface coverage from the integrated area of the TPD curve despite not being able to take infrared spectra for N_2 , since N_2 and CO have the same molecular mass.

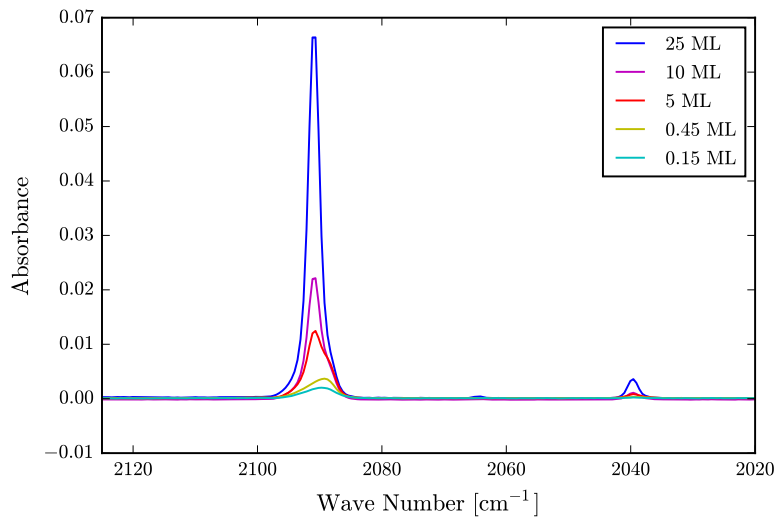


Figure 3.3: *Surface Coverage Calculation:* After the deposition of pure ^{13}CO onto the substrate, an infrared spectrum was taken. The integrated area under the reduced infrared absorbance features was correlated to the integrated area of the corresponding desorption curve, and a linear correlation factor was derived. At approximately 2040 cm^{-1} , we see an isotope absorbance feature, which was excluded from the spectral reduction. The deposition spectra and their corresponding surface coverages are shown above.

Temperature Programmed Desorption

Following the initial ice growth and characterization, desorption is induced by linear heating of the substrate via the temperature controller (1 K/min) to the targeted experimental temperature. In this thesis, experiments were carried out from 15 to 60 K. During each experiment, the gas-phase composition (including possible contaminating molecules) and desorption curves were measured using the QMS. TPD is a well-established experimental method in surface chemistry and predominant astrochemistry method in determining surface-adsorbate binding energies (e.g. Attired & Barnes 1998; Woodruff & Delchar 1994; Menzel 1982). The measured TPD signal traces desorption of both the multilayer and the monolayer, as shown in Figure 3.4. Since the onset, steepness, and height of the experimental curve are functions of the attempt frequency, binding energy, and surface concentration, we can extract the parameter values from the features of the measured desorption features.

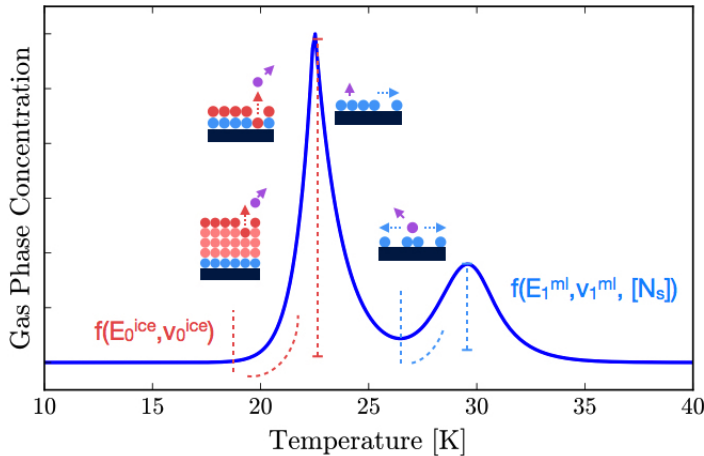


Figure 3.4: *Experimental TPD Signal*: The onset of desorption, the steepness of the desorption curve, and the height of the peak are functions of the attempt frequency, binding energy, and surface concentration, allowing us to extract these parameter values after measuring experimental desorption curves.

3.2 Experimental Design

Desorption experiments were performed for pure ices, layered ices on H₂O, and mixed ices on H₂O with varying surface coverages and H₂O deposition temperatures. Throughout this thesis, the notation X/Y denotes a layered ice morphology with X on top of Y , whereas $X : Y$

denotes a fully mixed ice system of both X and Y molecules. The notation $X - Y$ denotes the interaction between X and Y . In this study of the relative binding energies of CO and N₂, we vary across ice morphologies, H₂O substrate structure, and surface coverage to examine their relative effects on the desorption reaction barrier. In particular, we include the ice scenarios which could induce the greatest possible difference in binding energies between CO and N₂, in other words, would minimize $R_B = E_{B,N_2}/E_{B,CO}$.

3.2.1 Ice Morphologies

Three ice morphologies were included in the experimental suite: ¹ pure ices, ² layered ices on H₂O, and ³ mixed ices on H₂O, schematically shown in Figure 3.5. The pure ices are formed by cooling the chamber to ≈ 14 K, then depositing the gas directly onto the bare CsI window, resulting in a morphology shown in Figures 3.5a and 3.5b. These are the control experiments for our suite, and are comparable to those performed by Öberg et al. (2005) and Bisschop et al. (2006).

In the layered ice morphology, pure gas samples are deposited onto H₂O ice, which in turn has been pre-deposited onto the CsI substrate, resulting in a morphology shown in Figures 3.5c and 3.5d. Layered ices allow us to determine the binding energy values of $E_B(CO - H_2O)$ and $E_B(N_2 - H_2O)$ when the gas is interacting with H₂O in the presence of no other molecules. The layered multilayer ice morphology is indicated in astrophysical contexts by analysis of interstellar solid CO profiles, which reveal a component of pure CO ice of 60 – 90% of the total solid CO abundance clearly separated from the H₂O ice (Tielens et al. 191; Pontoppidan et al. 2003).

Additionally, we consider ice mixtures, where both CO and N₂ are present with H₂O. With ice mixtures, the binding energy values of $E_B(CO - H_2O)$ and $E_B(N_2 - H_2O)$ when both species are simultaneously present and interacting with H₂O can be determined. It is possible that H₂O preferentially binds to CO over N₂ when both are present, which would amplify any binding energy differential. At the multilayer surface coverages, segregation has been observed in CO : N₂ ice mixtures without H₂O ice (Öberg et al. 2005, Bisschop et al. 2006). The CO and N₂ components segregate immediately upon heating, forming layers above (N₂ overlayer) and

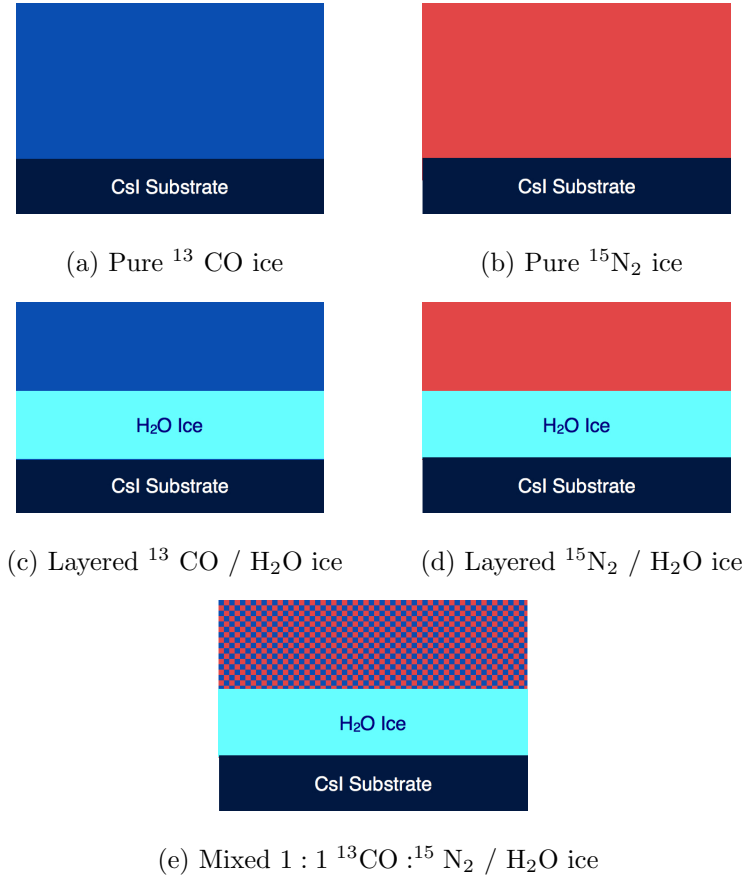


Figure 3.5: *Ice Morphologies*: Three different ice morphologies were included in the experimental suite. Firstly, pure ices were grown at varying coverages, serving as the control experiments for this study. Secondly, layered CO and N₂ ices were deposited onto an H₂O substrate. Lastly, a 1 : 1 CO : N₂ mixture was prepared and then deposited onto the H₂O substrate to examine desorption when both species are present and binding to the H₂O film.

under (CO underlayer) the mixture. As such, N₂ can desorb either from the pure N₂ overlayer or from the mixture, until the mixture has been fully segregated into an N₂/CO ice or desorbed. As the thickness of the ice increases, more of the mixture has segregated during the desorption process, allowing more N₂ to evaporate from the pure N₂ overlayer, effectively resulting in the same behavior as a layered ice. Öberg et al. (2005) found that the binding energy of CO molecules rises, with desorption hindered by N₂ rising to the overlayer, increasing the binding energy differential. However, at low exposures, particularly of sub-monolayer thicknesses, more of the N₂ has been found to desorb from the mixed-ice environment as the ice has not had enough time to fully segregate into layers. Therefore, a sub-monolayer coverage would reflect

true desorption from the mixture before segregation.

3.2.2 Surface Coverages

We examine both multilayer and monolayer ices of varying surface coverages. However, we focus on monolayer and sub-monolayer thicknesses. As discussed previously, the binding energy of the multilayer primarily reflects the binding energy between molecules of the same species since the multilayer surface molecules are in not in direct contact with the substrate, i.e. $E_{B,\text{CO}}^{\text{ice}} = E_{B,\text{CO}}^{\text{ice}}(\text{CO} - \text{CO})$, $E_{B,\text{N}_2}^{\text{ice}} = E_{B,\text{N}_2}^{\text{ice}}(\text{N}_2 - \text{N}_2)$. Alternatively, the binding energy of the CO multilayer to the N₂ multilayer is the pure ice binding energy ratio. Therefore, we want to examine relatively thick pure ice samples in order to obtain the pure ice binding energy ratio $R_B^{\text{ice}} = E_{B,\text{N}_2}^{\text{ice}}(\text{N}_2 - \text{N}_2) / E_{B,\text{CO}}^{\text{ice}}(\text{CO} - \text{CO})$. The monolayer desorption in the pure ice case would just yield the binding energy of the molecule to the CsI substrate, which is not of interest. As such, we want to look at high coverage pure ices in order to well-constrain the multilayer binding energy without interference from the pure ice monolayer.

Meanwhile, for the layered and mixture ice samples, we are more interested examining low coverage ices, since the binding energy of the monolayer is the binding energy of the molecule to H₂O, i.e. $E_{B,\text{CO}}^{\text{ml}} = E_{B,\text{CO}}^{\text{ml}}(\text{CO} - \text{H}_2\text{O})$, $E_{B,\text{N}_2}^{\text{ml}} = E_{B,\text{N}_2}^{\text{ml}}(\text{N}_2 - \text{H}_2\text{O})$. Therefore, we want to examine thin ices in these cases to clearly distinguish the monolayer peak, isolating the effects of the H₂O substrate on desorption to determine $R_B^{\text{ml}} = E_{B,\text{N}_2}^{\text{ml}}(\text{N}_2 - \text{H}_2\text{O}) / E_{B,\text{CO}}^{\text{ml}}(\text{CO} - \text{H}_2\text{O})$. Additionally, sub-monolayer exposures allow characterization of the shift to first-order desorption behavior with lower coverages.

3.2.3 H₂O Substrate Structures

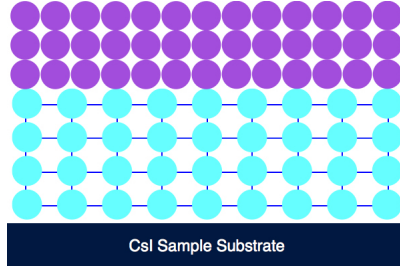
The total desorption barrier is proportional to the number of interactions between the molecules and the substrate; therefore, if CO binds more strongly to H₂O than N₂, increasing the number of interactions with H₂O should increase the measured binding energy differential between CO and N₂. The density of interactions between the molecules and H₂O can be increased with more porous H₂O films since more porous substrates offer more surface adsorption sites due to their uneven surface. Additionally, previous laboratory studies have demonstrated that

adsorbed molecules can diffuse through porous H₂O films, hindering desorption into the gas phase (Collings et al. 2002). Consequently, we expect any binding energy differential to be amplified with more porous substrates as shown in Figure 3.6.

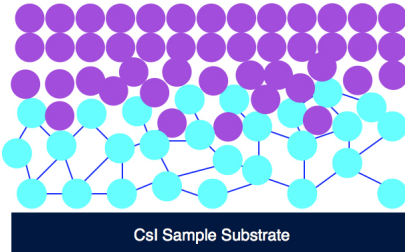
To grow H₂O ice films of increasing porosity, we vary the deposition temperatures of H₂O in the layered and mixed ice experiments to create three different H₂O substrate structures. In order to identify the critical deposition temperatures to grow these amorphous and crystalline ices, we consider three phases of H₂O ice evolution. Previous laboratory experiments have shown that H₂O accreted under the chemical conditions of cold dark clouds - namely temperatures of approximately 10 K, low adsorption rates, and random trajectories of adsorbate molecules - will result in a highly porous, amorphous ice structure (Collings et al. 2002). As such, these amorphous ices are of particular astrophysical relevance. To grow ices characteristic of this first, highly porous phase, we grow H₂O ice substrates at a deposition temperature of $T_{dep} = 14$ K. Next, this highly porous structure undergo an irreversible phase change to a lower density, less porous, yet still amorphous structure between 38–68 K (Jenniskens et al. 1995). Therefore, this second phase transition to a less porous structure is represented by H₂O ice substrates grown at $T_{dep} = 70$ K. Lastly, we grow H₂O ice at $T_{dep} = 100$ K to examine the effects of a flat, compact amorphous ice substrate. In conclusion, we chose three H₂O deposition temperatures in light of the phase changes of H₂O to examine the effects of increasing porosity: ¹ flat, least amorphous H₂O ice ($T_{dep} = 100$ K), ² less porous, less dense yet still amorphous H₂O ice ($T_{dep} = 70$ K), and ³ highly porous, amorphous H₂O ice ($T_{dep} = 14$ K).

In summary, by increasing the number of interactions between molecules and the H₂O substrate due to the diffusion of adsorbed molecules and greater density of binding sites, we expect that the binding energy differential would increase with more porous H₂O substrate structures.

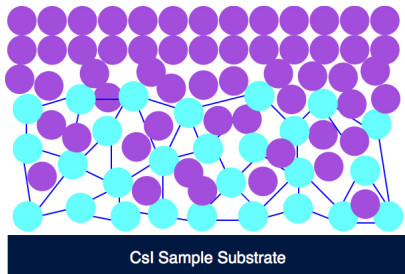
In light of these experimental design considerations, the ice sample suite is summarized in Table 3.2. We examine a range of astrophysically relevant ice samples, including “extreme case” ice samples believed to maximize the binding energy differential between CO and N₂. In particular, we pay attention to monolayer and sub-monolayer coverages, amorphous H₂O ices, and mixed-ice scenarios to isolate the binding energy of the molecules to the H₂O substrate.



(a) Crystalline H_2O ice, $T_{dep} = 100$ K



(b) Less porous H_2O amorphous ice, $T_{dep} = 70$ K



(c) Highly porous H_2O amorphous ice, $T_{dep} = 14$ K

Figure 3.6: *Structure of H_2O substrate:* The three H_2O structures grown at $T_{dep} = 100$, 70, and 14 K are shown, with the deposition temperatures chosen to represent each H_2O ice phase. With increasing porosity, adsorbate molecules (shown in purple, not to scale) can diffuse through the ice film (shown in blue), increasing the number of available binding sites, hindering desorption further and increasing the reaction barrier. Consequently, any binding energy differential between CO and N_2 ice should be amplified in the amorphous H_2O substrates.

With the effects of surface coverage, ice morphology, and H_2O ice structure taken together, we hypothesize that the mixed CO : N_2 ice morphology in the monolayer coverage regime deposited on highly porous H_2O ice grown at $T_{dep} = 14$ K would result in the greatest difference in binding energies between CO and N_2 .

Experimental Suite						
Scenario	Morphology	T_{dep} , H ₂ O	Coverage (ML)			
Pure ices	CO	-	0.15	0.45	5.00	10.0
	N ₂	-	0.75	1.50	10.0	17.0
Layered ices	CO/H ₂ O	100	0.15	1.50	10.0	15.0
		70	-	1.25	-	-
		14	0.25	-	-	-
	N ₂ /H ₂ O	100	0.50	2.00	-	-
		70	-	1.25	-	-
		14	0.25	-	-	-
Mixture ices	CO : N ₂ /H ₂ O	100	-	-	4.0	-
		14	-	0.5	-	-

Table 3.2: *Experimental Suite*: TPD experiments were carried out across three scenarios in varying morphologies, H₂O deposition temperatures, and surface coverages to examine a range of astrochemical contexts.

3.3 Experimental Results

3.3.1 Pure CO and N₂ Ices

In Figure 3.7, the TPD spectra for several ice exposures for pure CO and N₂ ices are shown. These pure ice experiments, with gas deposited on a bare CsI window, without H₂O, are the control experiments in this study.

The pure CO TPD curves, shown in Figure 3.7, indicate that the onset for desorption is approximately 28 K, in agreement with Öberg et al. (2005) and Bisschop et al. (2006). We observe that the leading edges of the TPD curves align, particularly for the thickest ices. This overlap suggests that desorption occurs at a rate that is independent of the surface coverage, consistent with zeroth-order kinetics of the multilayer. Consequently, the desorption curve peak shifts to higher temperatures for increasing ice coverages, peaking at approximately 31 K for the 25 ML exposure. Furthermore, we see that the 25, 10, and 5 ML desorption curves have a right shoulder, suggesting the monolayer desorption. The onset of monolayer desorption at higher temperatures indicates that the binding energy of the CO molecules to the CsI substrate is greater than the CO – CO interactions of the multilayer. Additionally, for the sub-monolayer, 0.45, 0.15 curves, the leading edges do not align, but instead seem to center on the curve peak at approximately 30 K, implying the shift to first-order kinetics.

The onset of N₂ desorption occurs at a slightly earlier temperature than CO, at approximately 26 K. This earlier onset of desorption is consistent with Bisschop et al. (2006). Similarly to CO, we observe again that the leading edges of the TPD curves overlap for multilayer coverages and that the peaks align, implying that the desorption rate is constant, i.e. zeroth-order kinetics. We also note the right shoulder on the 30, 17, and 10 ML desorption curves, suggesting the desorption of the monolayer. Again, the substrate appears to bind more strongly to the N₂ than the other N₂ molecules. The desorption substructures at approximately 33 K on the 30 ML curve reflects the higher sensitivity of the monolayer to any site with any stronger binding energy than average, or any experimental artifact (e.g. residual molecules on the CsI). At the 1.5 and 0.75 exposures, the leading edges shift away from those of the multilayers as the desorption rate becomes dependent on how many molecules there are left on the surface.

3.3.2 Layered CO/H₂O and N₂/H₂O Ices

In the layered ice experiments, we varied not only the surface coverages but also the temperature at which the initial H₂O was deposited, T_{dep} , resulting in H₂O ices of increasing porosity. As discussed previously, we are interested in comparing the monolayer peaks from experiments involving H₂O ices to the pure ice multilayer peaks to examine the effects of an H₂O substrate, since desorption from the monolayer in direct contact with the H₂O reflects the strength of the CO – H₂O and N₂ – H₂O interactions. We are also interested in comparing the monolayer peaks from experiments involving H₂O ices with each other to examine how changing the H₂O substrate structure influences desorption from its surface.

The results for these low coverage layered ices are shown in Figure 3.8. Firstly, CO and N₂ were deposited at various multilayer and monolayer thicknesses onto H₂O deposited at 100 K. We see that both CO – H₂O and N₂ – H₂O desorption profiles from the H₂O surface, as traced by the monolayer peaks, are shifted to higher temperatures than CO – CO and N₂ – N₂ desorption profiles, as traced by the pure CO and N₂ ice multilayer peaks. The CO – H₂O monolayer peak occurs at \approx 37 K, a significant increase from the pure ice CO – CO multilayer peak at \approx 31 K. Similarly, the N₂ – H₂O monolayer peak occurs at \approx 37 K, also significantly increasing from the pure ice N₂ – N₂ peak at \approx 27 K.

Subsequently, H₂O ice was grown at 70 and 14 K to examine cases of intermediate and high porosity. In Figure , we see that CO desorbs at increasingly higher temperatures with decreasing T_{dep} , or with more porous H₂O ices. Specifically, we see that the CO – H₂O $T_{dep} = 70$ K curve peaks at ≈ 41 K, a shift by ≈ 5 K from the CO – H₂O $T_{dep} = 100$ K case, and by ≈ 11 K from the pure CO – CO multilayer peak. Furthermore, the CO – H₂O $T_{dep} = 14$ K curve peaks at ≈ 50 K, reflecting an even higher reaction barrier with the most porous H₂O substrate structure.

In Figure , we examine the effects of changing the H₂O ice structure on N₂ desorption and observe a similar trend with CO layered ices. The monolayer peaks shift to higher temperatures with increasing substrate porosity, indicating higher reaction barriers. The N₂ – H₂O $T_{dep} = 70$ K monolayer peaks at ≈ 39 K, and the N₂ – H₂O $T_{dep} = 14$ K peaks at approximately ≈ 45 K.

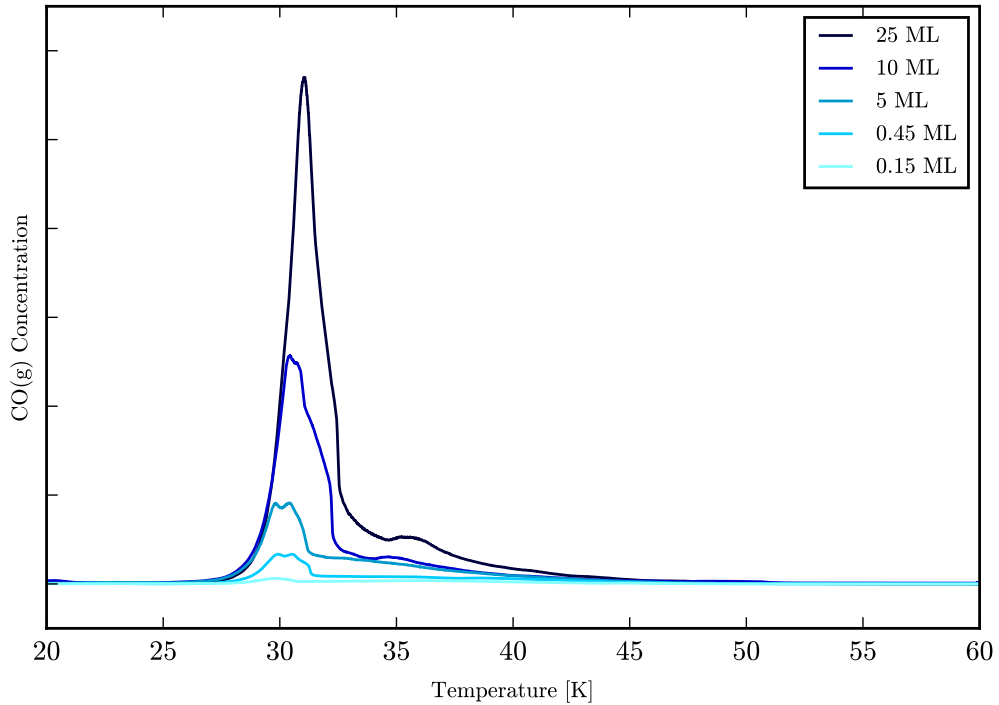
From visual examination of the desorption curves, we immediately see that both layered CO and N₂ ices experience an increase in desorption barrier with more porous H₂O substrates. However, a binding energy differential would require CO to react more strongly to changes in the H₂O substrate than N₂; i.e. the relative increase in the desorption barrier should be greater for CO layered ices than N₂ layered ices.

3.3.3 Mixed CO : N₂/H₂O Ices

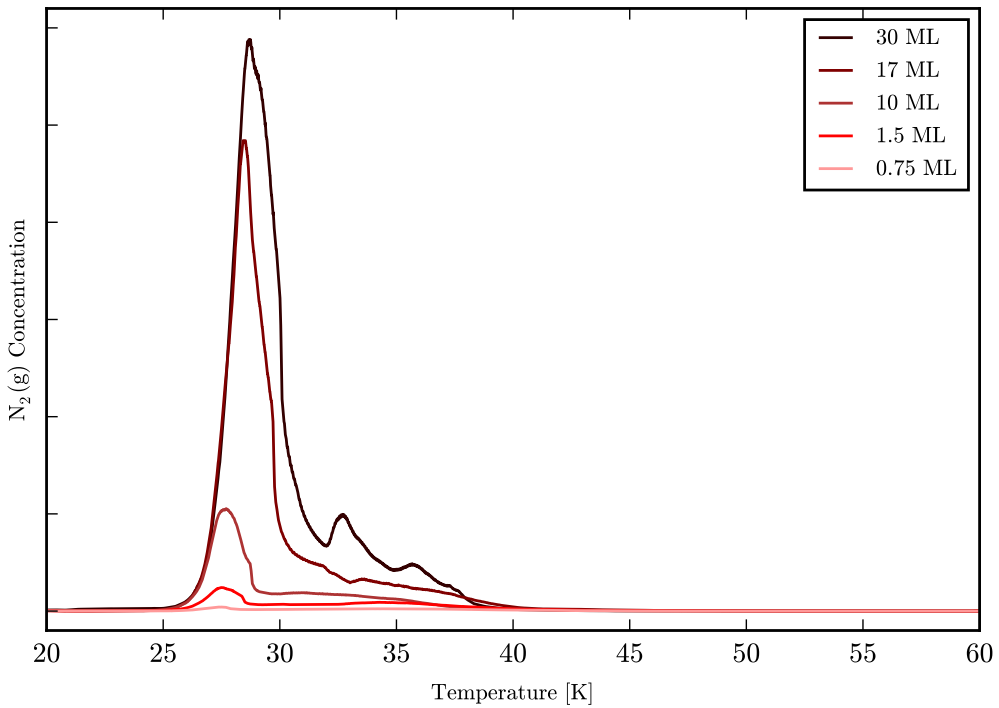
We examine mixed CO : N₂/H₂O ice samples to examine any preferential binding effects when both CO and N₂ are desorbing from H₂O. The mixed 1 : 1 CO : N₂ ice was prepared in advance, then deposited onto H₂O in the same manner as the layered ices. We performed the mixture experiment twice, layered on crystalline H₂O ice ($T_{dep} = 100$ K), and highly porous H₂O ice ($T_{dep} = 14$ K). We deposited the CO : N₂ mixture over the highly porous case at a sub-monolayer coverage, to examine when CO and N₂ are interacting with H₂O ice simultaneously and co-desorbing, rather than desorbing from the segregated pure layers that form at higher coverages. While the desorption curves do not significantly differ from the layered morphology in the $T_{dep} = 100$ K ice structure case, we are particularly interested in the highly porous H₂O ice structure in the monolayer regime. The low coverage layered CO/H₂O and N₂/H₂O ice desorption curves are shown in Figure 3.9 with the desorption curves from the CO : N₂/H₂O

ice mixture, deposited onto a highly amorphous, porous H₂O ice structure grown at $T_{dep} = 14$ K.

In examining both the layered and mixed ice samples deposited on highly porous H₂O ice films, we see that CO desorption peak is shifted to a higher temperature than the corresponding N₂ desorption peak. In addition to quantifying this as a binding energy differential, we are interested in which ice morphology yields the greatest difference in desorption behavior.

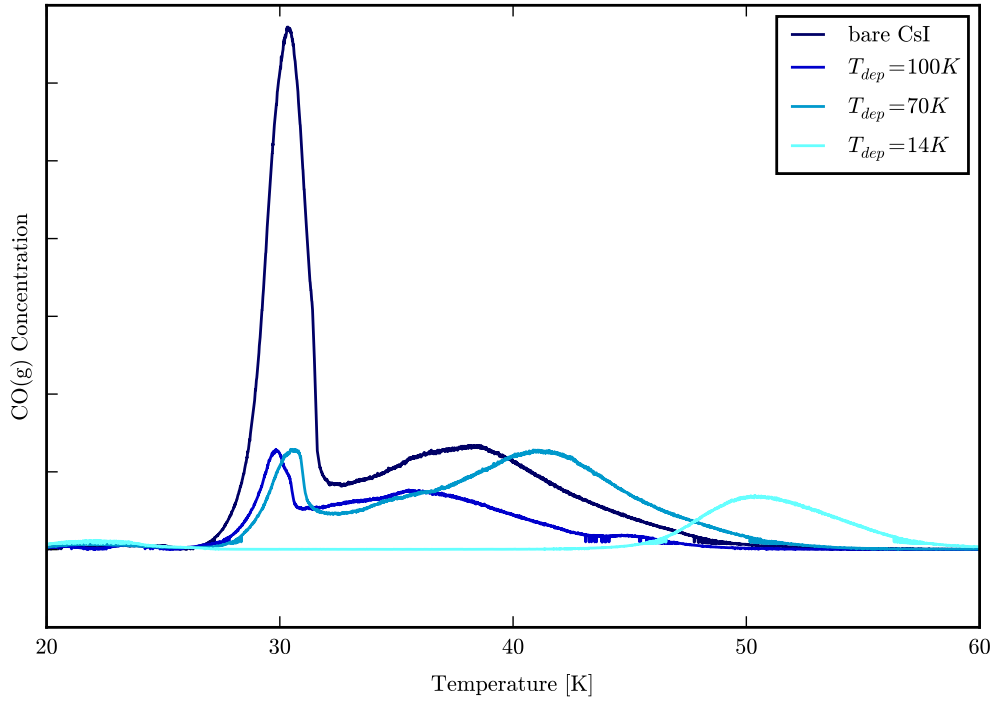


(a) Pure CO ice

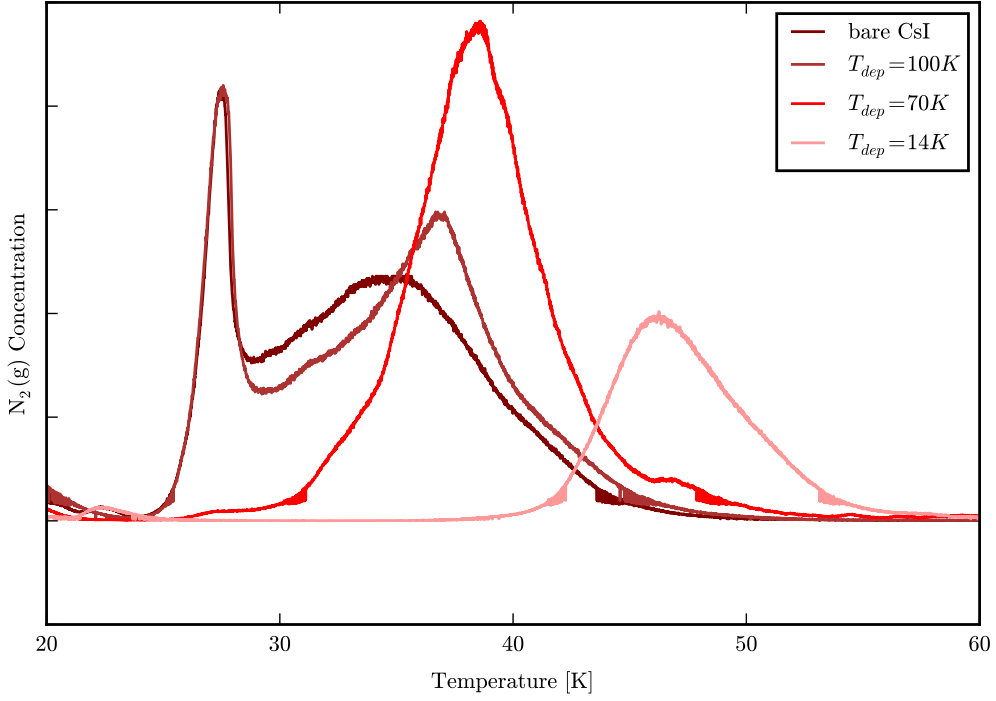


(b) Pure N₂ ice

Figure 3.7: *Pure ices*: For both pure CO and N₂, the multilayers exhibit zeroth-order desorption behavior, characterized by overlapping leading edges and peaks shifted to higher temperatures with higher coverages. For the lower coverages ices, we observe convergence to first-order kinetics, with non-coinciding leading edges and peak alignment, implying that the desorption rate is dependent on the number of molecules left on the surface.



(a) CO/H₂O ice



(b) N₂/H₂O ice

Figure 3.8: *Layered ices*: In comparing the CO – H₂O monolayers to the pure CO – CO multilayer and the N₂ – H₂O monolayers to the pure N₂ – N₂ multilayer, we see that desorption from H₂O is shifted to a higher temperature. Additionally, we see that desorption shifts to higher temperatures with increasing H₂O porosity, as traced by the CO – H₂O and N₂ – H₂O monolayers.

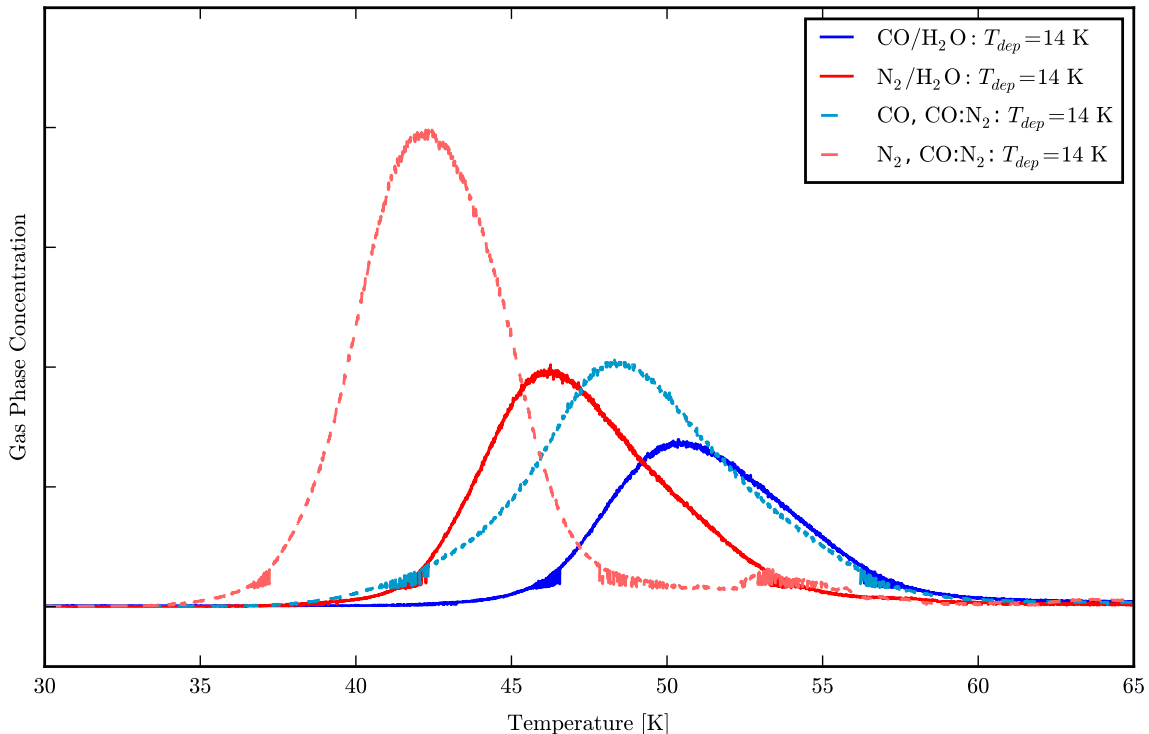


Figure 3.9: *Layered and Mixed Ices on Highly Porous Substrate*: The monolayer desorption curves of both layered $\text{CO}/\text{H}_2\text{O}$ and $\text{N}_2/\text{H}_2\text{O}$ are shown alongside the curves from the $\text{CO} : \text{N}_2/\text{H}_2\text{O}$ ice mixture. For both ice morphologies, we see that there is a difference in peak temperatures between CO and N_2 curves. As such, we are interested in identifying which scenario yields the greatest quantitative binding energy difference.

Chapter 4

Model Parameter Estimation

With the kinetic model constructed in Chapter 2, we can reproduce each experimental desorption curve as the temporal evolution of the coupled differential equation system as the temperature is raised in a linear manner. Using the numerical best fit of the model to the data, the parameter values, namely the binding energies, of the desorption process can be extracted.

4.1 Model Parameters

The parameters of the desorption process model are the pre-exponential factors for both the zeroth-order multilayer v_0^{ice} and the first-order monolayer v_1^{ml} , the initial concentration of adsorbed molecules on the multilayer substrate $[N_{(s)}]$, the temperature range T , the pump rate v_p , the reaction order i , and the binding energies of each desorption reaction, E_B^{ml} and E_B^{ice} . As discussed previously in Chapter 2, we do not require that desorption occur in a single step, and allow the binding energy and pre-exponential factors to vary with the surface coverage of the ice film. In particular, the desorption behavior is much more likely to have first-order character at the monolayer and sub-monolayer level when evaporated molecules cannot be readily replaced at the surface. Most importantly, the binding energy of the multilayer, E_B^{ice} , is primarily the binding energy of the molecule to other molecules of the same species, whereas the binding energy of the monolayer E_B^{ml} specifically reflects the binding energy of the molecule to the substrate. As such, we calculate the binding energies and attempt frequencies of the zeroth-order

multilayer and the first-order monolayer desorption processes separately.

The temperature range of the model T , extends from 15 to 60 K to match the temperature range of the desorption experiments. The value of v_p is experimentally determined for both CO and N₂, and consequently fixed for the iterations of the kinetic model. The reaction order i , is determined by the measured thickness of the ice film (see Chapter 3 for a discussion of surface coverage calculation from IR spectra). For all layers besides the monolayer, $i = 0$, and for the monolayer (or any sub-monolayer ice samples), $i = 1$. The initial concentration of molecules in the multilayer [$N_{(s)}$] is inputted as an initial condition to the differential equation system, and is obtained as the product of the multilayer surface coverage and the surface density (of order 10¹⁵ molecules cm⁻²).

In this experimental application, an observation, $D = N_{(g)}$, is the desorption curve measured in a TPD experiment. This desorption curve can be predicted from the theoretical model constructed in Chapter 2, with two model parameters, the binding energies, and two nuisance parameters, the pre-exponential factors. Additionally, we add another tuning nuisance factor, denoted X , to our fitting of sub-monolayer regime curves. As discussed in Chapter 3, the surface coverage is determined via a linear correlation factor between the integrated area of the infrared absorption peaks and the desorption curves. However, any residuals to this direct fit can have significant effect on low exposure ices, due to their initial thinness. In particular, the surface coverage is particularly vulnerable to underestimation for the more porous ices (i.e. $T_{dep} = 70, 14$ K). Since the molecules diffuse within the ice and are exposed to a greater density of binding sites, the infrared beam straight through the adsorbed ice may not account for the uneven surface of these amorphous ices. Therefore, we scale the solid state concentration with X to address this surface coverage underestimation risk with low exposure ice samples. Meanwhile, we do not need to include the multilayer parameters in our monolayer model since multilayer desorption does not occur. The four remaining physical parameters that must be fit to the data are the pre-exponential factors and the binding energies: v_0^{ice} , v_1^{ml} , E_B^{ice} , and E_B^{ml} .

In summary, for multilayer ices, we have a we have a four dimensional problem, with model parameters $\Theta_{ice} = E_B^{ice}, E_B^{ml}$, and nuisance parameters $\alpha_{ice} = v_0^{ice}, v_1^{ml}$. For monolayer ices, we have a three dimensional problem, with model parameter $\Theta_{ml} = E_B^{ml}$, and nuisance

Parameter	Notation	Constraint
Temperature	T	Experiment parameter
Reaction order	i	Calculated from surface coverage
Initial surface concentration	$[N_{(s)}]$	Calculated from surface coverage
Pump rate	v_p	Experimental parameter
Zeroth-order pre-exponential factor	v_0^{ice}	Numerical model fit
First-order pre-exponential factor	v_1^{ml}	Numerical model fit
Zeroth-order binding energy	E_B^{ice}	Numerical model fit
First-order binding energy	E_B^{ml}	Numerical model fit
Monolayer turning	X	Numerical model fit

Table 4.1: *Model parameters*: The multilayer model is four-dimensional, with model parameters $\Theta_{ice} = E_B^{ice}, E_B^{ml}$, and nuisance parameters $\alpha_{ice} = v_0^{ice}, v_1^{ml}$. For monolayer ices, we include a tuning parameter to mitigate risks of surface coverage underestimation, particularly in porous ices, to result in the three-dimensional problem $\Theta_{ml} = E_B^{ml}$, and nuisance parameters $\alpha_{ice} = v_1^{ml}, X$.

parameters $\alpha_{ice} = v_1^{ml}, X$. The coupled differential equation system can be iterated using a Python integrator, namely `odeint`.

To optimize the parameter fitting, we implemented a numerical fitting method to the kinetic model constructed for the desorption process, described below. The parameters and their pre-existing constraints are summarized in Table 4.1.

4.2 Markov Chain Monte Carlo (MCMC) Numerical Fitting

Since there are four physical undetermined parameters, we are seeking the *set* of best-fit values that yields the most accurate fit rather than the individual best-fit values. Therefore, in astrochemical model fitting both sets of parameters need to be used in combination to accurately reproduce the behavior of CO and N₂. To ensure that we optimize the model fit across the combination of these four parameters, we apply Markov chain Monte Carlo (MCMC) numerical method of Bayesian inference.

Bayesian inference is a standard procedure in probabilistic data analysis when measurement results are compared to predictions of a multiple parameter-dependent model. MCMC methods are useful in fitting problems involving several free parameters and coupled systems such as this one. Furthermore, Bayesian data analysis enables us to marginalize over nuisance parameters, or a parameter that is required in order to model the process that generates the data, but is otherwise of little interest. In this scenario, the pre-exponential factors are necessary

model parameters, but are not of astrochemical interest to us. Marginalization is the process of integrating over all possible values of the parameter, and hence propagating the effects of uncertainty about its value into the final result. The final result is the marginalized probability function $p(\Theta|D)$ of the set of model parameters $\Theta = E_B^{ice}, E_B^{ml}$ given the set of experimental observations D :

$$p(\Theta|D) = \int p(\Theta, \alpha|D) d\alpha \quad (4.1)$$

where $\alpha = v_{ice}^0, v_{ml}^1$ is the set of nuisance parameters. A critical advantage of an MCMC-generated sampling of values (Θ, α) of the model and nuisance parameters from the joint distribution $p(\Theta, \alpha|D)$ automatically provides a sampling of values of the model parameters of interest Θ , from the marginalized probability distribution function $p(\Theta|D)$. Due to this advantage in treatment of nuisance parameters, in this case the pre-exponential factors, the MCMC process provides the most rigorous method of parameter fitting to obtain binding energy estimates.

4.2.1 Bayesian Inference Overview

The *likelihood function* $p(D|\Theta, \alpha)$ is defined as the conditional probability of a measurement outcome D given the model parameters (binding energies) fixed to θ and nuisance parameters (pre-exponential factors, tuning factor) fixed to α . Bayesian inference hinges on the concept of conditional probability to revise knowledge of a parameter distribution with additional information. Initially, we have a *prior distribution* $p(\Theta, \alpha)$ based on some information on Θ . Then combining the likelihood function with the prior distribution via Bayes theorem, we can obtain the *posterior probability density* $p(\Theta, \alpha|D)$, or the conditional density of Θ given the data:

$$p(\Theta, \alpha|D) = p(\Theta, \alpha) p(D|\Theta, \alpha). \quad (4.2)$$

MCMC algorithms draw M samples from the posterior probability density, then approximate the marginalized constraints on Θ by projecting the histogram of samples into the parameter subspace spanned by Θ . This yields the expectation value of a model outcome of the

model parameters $f(\Theta)$:

$$\langle f(\Theta) \rangle = \int p(\Theta|D) f(\Theta) d\Theta \approx \frac{1}{M} \sum_{i=1}^M f(\Theta_i). \quad (4.3)$$

The generation of the samples Θ_i is non-trivial for an unknown distribution $p(\Theta, \alpha, D)$. As such, MCMC is a sample generation procedure that generates a random walk in the parameter space that, over iterations, draws a representative set of samples from the distribution. Each point in a Markov chain $X(t_i) = [\Theta_i, \alpha_i]$ depends only on the position of the previous step.

4.2.2 Choice of MCMC Algorithm

Metropolis-Hastings (M-H) Algorithm

The most common MCMC algorithm is the Metropolis-Hastings (M-H) algorithm (MacKay 2003) and is the basis of most computational MCMC packages. However, as discussed later, the M-H algorithm has inherent limitations addressed by derivative algorithms. The iterative procedure is initialized at position $X(t)$, then a proposal next step position Y is sampled from the transition distribution $Q(Y; X(t))$. This proposal is accepted with probability:

$$\min \left(1, \frac{p(Y|D)}{p(X(t)|D)} \frac{Q(X(t); Y)}{Q(Y; X(t))} \right) \quad (4.4)$$

The transition distribution is typically an easily sampled probability distribution for the proposal Y given a position $X(t)$, most commonly a Gaussian. If this step is accepted $X(t+1) = Y$; otherwise, the new position is set to the previous one $X(t+1) = X$. The M-H algorithm then converges with time to a stationary set of samples from the target distribution. However, the efficiency of sampling and conversation crucially depends on the chosen transition distribution. If the transition distribution mainly proposes positions in the relevant parts of the parameter space where the target distribution is large, the chain converges quickly to a sample of the target distribution. Conversely, if the transition distribution tends towards positions where the target distribution has low probability, most of the steps are rejected and the samples will

be heavily correlated and unrepresentative of the parameter space.

Metropolis-Hastings Algorithm Application to Desorption Modeling

The likelihood function $p_{ice}(D|\Theta_{ice}, \alpha_{ice}) = p(N_{(g)}|E_B^{ice}, E_B^{ml}, v_0^{ice}, v_1^{ml})$ or $p_{ml}(D|\Theta_{ml}, \alpha_{ml}) = p(N_{(g)}|E_B^{ml}, v_1^{ml}, X)$ of the parameters in the model arises from the conditional probability of the experimental result given a particular set of parameters. However, since the model itself depends on the numerical `odeint` integrator and is not an analytical function of Θ and α , the likelihood function, and in turn the posterior probability distribution (as the product of the likelihood and the prior distribution), are also not available as analytical functions of the parameters of interest. Consequently, the M-H algorithm critically suffers from the fact that calling the likelihood function through the integrator is computationally costly in terms of algorithm stability, time, and efficiency in terms of likelihood function calls per converged sample.

Affine Invariant Ensemble Sampling Algorithm

To increase the computational efficiency of MCMC sampling in this astrochemical application where the likelihood function is difficult to evaluate numerically, we turn to a more recent MCMC algorithm proposed by Goodman and Weare (2010). This algorithm is an affine-invariant ensemble sampling method that produces independent samples from non-analytical models with much shorter convergence times. By *affine invariant*, we mean that the algorithm is invariant under linear transformations of the target probability function. Thus for X with a probability distribution $p(x)$, then the affine transformation $Y = AX + b$ has probability density:

$$p_{A,b}(y) = p_{A,b}(Ax + b) \propto p(x). \quad (4.5)$$

This implies specifically that the sampler is not sensitive to the scales of the parameter distributions and does not depend on the covariances of the target distribution. For an MCMC algorithm R , affine invariance holds if:

$$R(Ax + b, p_{A,b}) = AR(x(t), p) + b, \quad (4.6)$$

for all x .

Instead of initializing at a single position $X(t)$ which is updated at each time step of the sampling, this algorithm involves simultaneously evolving an *ensemble* \vec{S} of size K of *walkers*, $\vec{S} = \{\vec{X}_k\}$, which are spread on the parameter space of the target distribution, as shown in Figure 4.1. Therefore, for an N -dimensional problem, the ensemble $\vec{S} = (X_1, \dots, X_K)$ is in state space of dimension $N \times K$. The target probability distribution for the ensemble of walkers is such that the walkers are independent and drawn from p :

$$P(\vec{s}) = P(x_1, \dots, x_K) = p(x_1)p(x_2) \dots p(x_K). \quad (4.7)$$

Therefore, an ensemble MCMC algorithm is a Markov chain, but applied to the state spaces of the walkers to produce a sequence $X(t)$. Therefore, an MCMC ensemble algorithm is affine invariant if affine invariance holds when applied to each walker:

$$\vec{S} = (X_1, \dots, X_K) \rightarrow A, b(AX_1 + b, \dots, AX_K + b) = (Y_1, \dots, Y_K) = \vec{Y}. \quad (4.8)$$

Each step of the Markov chain for the ensemble sample $\vec{S}(t) \rightarrow \vec{S}(t+1)$ is one cycle through all K walkers in the ensemble. In pseudo-code, a cycle would be:

```

for  $k = 1, \dots, K$ 
{
    update:  $X_k(t) \rightarrow X_k(t+1)$ 
}

```

The proposal distribution for one walker k is based on the current position of the $K - 1$ walkers in the *complementary ensemble* $S_{[k]} = \{X_j, \forall j \neq k\}$. In this case, position refers to a vector in the N -dimensional parameter space.

The algorithm used moves walkers with the *stretch move*. To evolve a walker at position X_k , a walker X_j is drawn randomly from the remaining walkers $S_{[k]}$ and a new position is

proposed of the form below:

$$X_k(t) \rightarrow Y = X_j + Z [X_k(t) - X_j], \quad (4.9)$$

where Z is a random variable drawn from a distribution $g(Z = z)$. If we have that $g(z^{-1}) = zg(z)$, then the proposal is symmetric:

$$P(X_k(t) \rightarrow Y) = P(Y \rightarrow X_k(t)). \quad (4.10)$$

The proposal value lies on the line:

$$\{y - X_j = \lambda(X_k(t) - X_j), \lambda > 0\},$$

so the conditional density along this ray is proportional to:

$$|y - X_j|^{n-1} p(y).$$

Therefore, the proposal $X_k(t+1) = Y$ is accepted with probability

$$q = \min \left(1, \frac{|Y - X_j|^{n-1} p(Y)}{|X_k(t) - X_j|^{n-1} p(X_k(t))} \right) = \min \left(1, Z^{N-1} \frac{p(Y)}{p(X_k(t))} \right), \quad (4.11)$$

where N is the dimension of the parameter space. If rejected, $X_k(t+1) = X_k$. This procedure is then iterated for each walker. In pseudo-code, a stretch move is expressed as:

```

for  $k = 1, \dots, K$ 
{
    choose  $X_j \in \vec{S}_{[k]}(t)$  randomly
    generate  $Y = X_j + Z(X_k(t) - X_j)$  with all  $Z$  independent
    accept, set  $X_k(t+1) = Y$  with probability  $q$ 
    otherwise reject, set  $X_k(t+1) = X_k(t)$ 
}

```

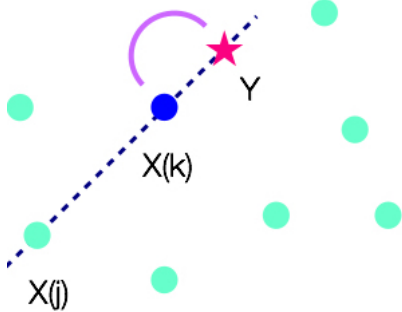


Figure 4.1: *Affine Invariant Ensemble Sampling*: A stretch move generates a proposal (purple) for walker X_k by choosing another walker X_j and generating a position that is a random linear combination of the current positions of both walkers. Therefore, as one walker converges to the mode of the posterior probability distribution, the other walkers are also pulled to convergence. Furthermore, the sequence $\vec{S}(t)$ is still Markov since the path only depends on the current, not historical, positions of the walkers, thus is not biased.

Affine Invariant Ensemble Sampling Algorithm Application to Desorption Modeling

Our model includes parameters of varying scales: the pre-exponential factor of the multilayer is on the order of $\sim 10^{25} - 10^{27}$, the pre-exponential factor for the monolayer is on the order of $\sim 10^{11} - 10^{13}$, the binding energies are on the order of $\sim 10^2 - 10^3$, and X is between 1.0 and 2.0. Due to the wide spread of the parameter scales, the model can be unwieldy and covariances difficult to analyze. However, the affine invariance, or invariant sampling under linear transformations, of the algorithm improves the stability of a model and improves selection of a comprehensive sample. Additionally, as mentioned previously, the computational efficiency of this algorithm in the case of the kinetic model used in this thesis is much higher with the affine invariant ensemble sampling algorithm than with the M-H algorithm. The desorption model involves intensive computational integration, and adding the integration of the likelihood function results in an undesirable computational cost. Meanwhile, implementing a system of walkers minimizes the integrations of the likelihood function, increasing computational efficiency.

4.2.3 Comparison to Previous Methods

Previous laboratory desorption experiments have implemented varying methods of determining the values of the binding energies and the pre-exponential factors. Firstly, several studies have used analytical approximations of the surface binding energy. Öberg et al. (2005) assumes that

the enthalpy of the adsorption and desorption are equal in the experimental system, enabling the mean desorption energies to be equivalent to the mean binding energy, and can be approximately estimated from the TPD peak position (Attard & Barnes 1998) as:

$$E_B = T_{peak} \times 30.068. \quad (4.12)$$

Similarly, Fraser et al. (2001) estimate the surface binding energy by assuming a known pre-exponential factor, v , and analytically deriving E_B . As shown in Chapter 2, in our case the first derivative of the gas concentration yields the maximum peak position, which in turn gives us:

$$E_B/T_{peak}^2 = (v/\beta)iN_{ice}^{i-1}\exp(-E_B/T_{peak}) \quad (4.13)$$

where T_{peak} is the temperature at the peak of the desorption curve, v is the assumed pre-exponential factor, β is the heating rate, and i is the reaction order. However, both of these methods of approximation do not account for how desorption does not occur in one step, the surface binding energies vary in value across the binding sites, and the pre-exponential factors cannot be assumed but can actually vary on the scales of orders of magnitude.

Meanwhile, the predominant numerical fitting method of laboratory desorption experiments (Bisschop et al. 2006, Fayolle et al. 2011) is χ^2 analysis. A grid of pre-exponential factors and binding energies is constructed, and the maximum likelihood is obtained. While χ^2 analysis is rigorous relative to the approximation methods, the parameter values critically depend on the constructed grid and can only be affixed to grid values. In contrast, MCMC convergence ensures that the global optimum of parameter value set is chosen.

4.2.4 MCMC Sampling Implementation

Python Module `emcee`

The affine invariant ensemble sampling algorithm described above was implemented as the Python module `emcee` by Foreman-Mackey et al. (2012). In this adapted implementation, the

algorithm does not update the walkers serially but instead divides them into two subgroups and updates all the walkers with stretch moves from one subgroup at a time, using the other half of the walker as their references. While the Python module `pymc`, based on the M-H algorithm, has been more widely used, we chose to implement the `emcee` module due to the relative advantages of affine invariant ensemble sampling over the M-H algorithm.

Firstly, we mentioned previously that the efficiency of the M-H algorithm is critically dependent on the transition distribution between positions $Q(Y; X(t))$. If we consider Q to be an m -dimensional Gaussian distribution with unknown covariance matrix, we find that $m - H$ has $m(m + 1)/2$ tuning parameters. When the scales of variances and covariances of the probability distributions are well-correlated before the sampling, the tuning parameters can be appropriately chosen, the M-H algorithm supplied with an appropriate covariance matrix, the parameter space efficiently explored, and convergence achieved quickly. However, in the case of an unknown probability distribution, the efficiency of the M-H algorithm decreases. Furthermore, if the probability distribution is non-Gaussian, the transition distribution may not accurately match the target probability distribution, resulting in low convergence efficiency. Since we do not have much prior knowledge on the probability distribution of the parameters, the efficiency of M-H algorithm implementation is undermined. Conversely, the property of affine-invariance ensures that the algorithm is not sensitive to the scales of the target distribution. As such, the efficiency of the sampling process does not depend on having a good estimate of the target distribution before sampling, and the algorithm does not need to be significantly and repeatedly tuned.

Secondly, the implementation of walkers instead of a single chain is particularly well suited for the numerically integrated character of our kinetic model. Since the `emcee` module updates a large number of positions simultaneously, the demands for repeated numerical integrations in the likelihood and posterior probability functions are reduced, reducing the instability of the sampling process and decreasing computational cost.

Computational Considerations

As mentioned previously, for multilayer desorption experiments, we consider:

$$\Theta_{ice} = E_B^{ice}, E_B^{ml}$$

$$\alpha_{ice} = v_0^{ice}, v_1^{ml}$$

and for monolayer desorption experiments, we are interested in:

$$\Theta_{ml} = E_B^{ml}$$

$$\alpha_{ml} = v_1^{ml}, X$$

where Θ denotes the model parameters and α denotes the nuisance parameters. A model is fit to each desorption curve over the temperature range of the experiment. The likelihood function integrates the kinetic model constructed in Chapter 2, then compares the model to the imported experimental data of the measured gas phase concentration while propagating the experimental error. The likelihood function is then maximized using the `scipy.optimize` module, allowing us to obtain maximum likelihood estimates for all four parameters. The full posterior probability distribution is then obtained through the product of the likelihood functions and priors, which are informed by previous literature values, and this distribution is then sampled with `emcee`. The walkers are initialized in a random array around the maximum likelihood result, and we call on an ensemble of $K = 1000 \times$ dimension walkers. In other words, $K_{ice} = 1000 \times 4 = 4000$ and $K_{ml} = 1000 \times 3 = 3000$. Since the walkers start in small distributions around the maximum likelihood values, then take time to fully explore the parameter space and reach the mode of the posterior distribution, we allowed a burn-in time of 500 steps, which was obtained from the walker convergence time. The sampler is then reset such that the walkers “forget” their previous steps (first 500 steps are discarded). MCMC sampling is run for either 10,000 or 15,000 additional steps. For the monolayer samples, the desorption curve was often “clean” enough such that only 10,000 iterations were needed to comprehensively explore the parameter space. However, for some of the noisier desorption curves, particularly the multilayer curves, 15,000

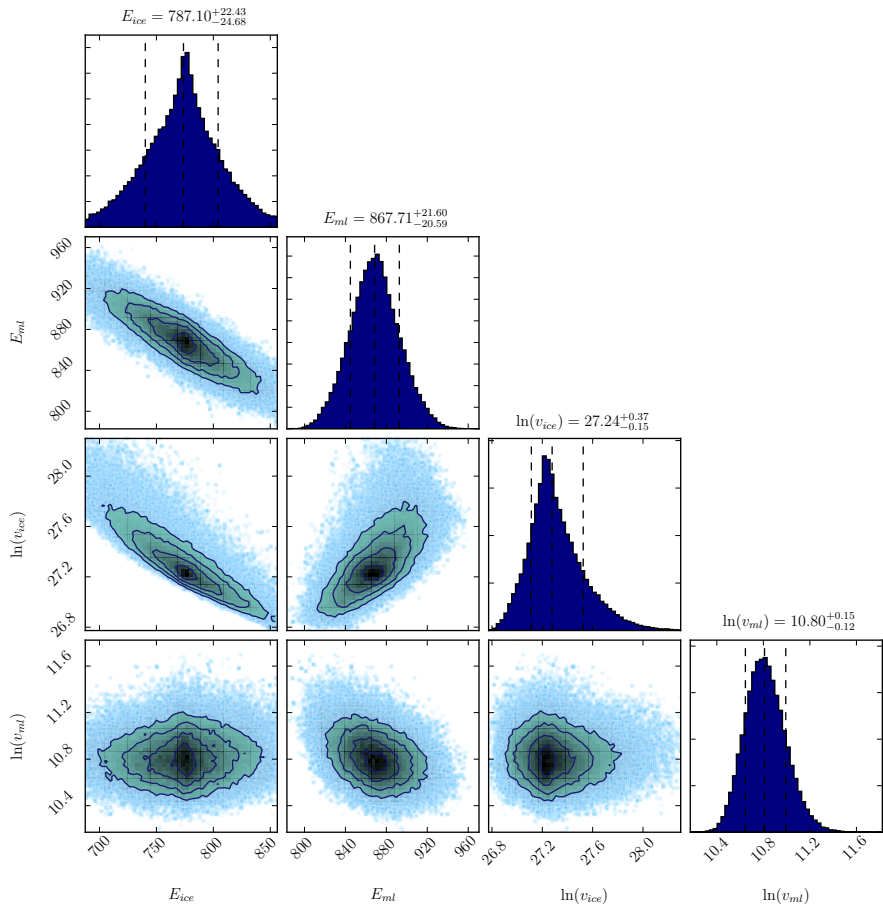
iterations were needed. As a result, we obtain a list of samples yielding parameter probability distributions for each of the parameters.

4.3 Parameter Estimation Results

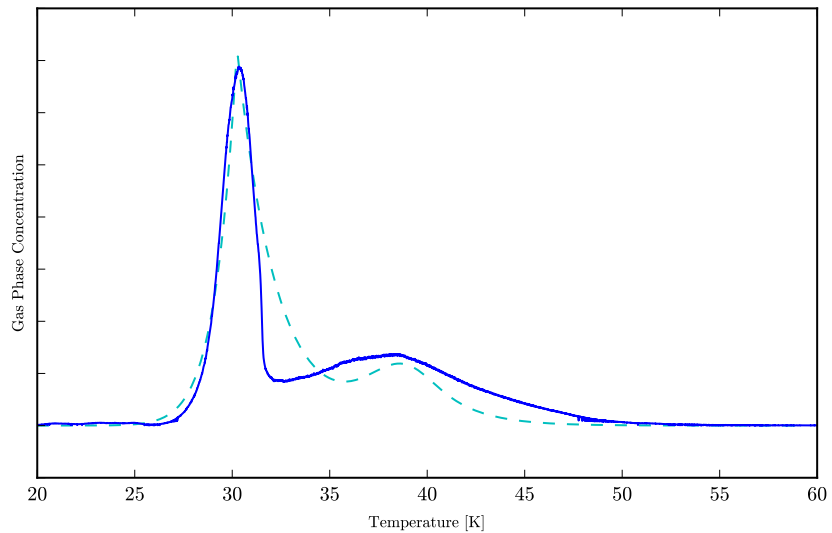
The MCMC triangle plots and the fits to data are visualized in the Figures 4.2 to 4.11. Additionally, Table 4.2 gives the parameter values derived from MCMC fitting to the experimental desorption curves.

Binding Energy Results						
Morphology	Species	$T_{dep}, \text{H}_2\text{O}$	$\ln(v_0^{ice})$	$\ln(v_1^{ml})$	E_B^{ice}	E_B^{ml}
Pure ices	CO	-	$27.24^{+0.37}_{-0.15}$	$10.80^{+0.15}_{-0.12}$	$787.10^{+22.43}_{-24.68}$	$876.71^{+21.60}_{-20.59}$
	N ₂	-	$26.98^{+2.16}_{-1.68}$	$10.81^{+0.23}_{-0.22}$	$786.84^{+21.64}_{-24.89}$	$833.56^{+20.33}_{-18.28}$
Layered ices	CO/H ₂ O	100	$26.14^{+3.58}_{-2.67}$	$10.81^{+0.11}_{-0.11}$	$822.24^{+28.12}_{-24.17}$	$884.27^{+20.42}_{-19.46}$
		70	$25.66^{+0.23}_{-0.34}$	$10.82^{+0.12}_{-0.11}$	$852.49^{+21.15}_{-22.25}$	$1052.71^{+9.21}_{-9.12}$
		14	-	$12.93^{+0.25}_{-0.28}$	-	$1461.12^{+26.19}_{-31.12}$
	N ₂ /H ₂ O	100	$27.11^{+0.40}_{-0.35}$	$10.41^{+0.13}_{-0.12}$	$813.35^{+34.25}_{-36.23}$	$852.65^{+22.44}_{-21.43}$
		70	-	$10.97^{+0.29}_{-0.28}$	-	$942.07^{+25.05}_{-26.64}$
		14	-	$11.03^{+0.19}_{-0.13}$	-	$1293.32^{+33.19}_{-39.12}$
Mixture ices	CO, CO : N ₂ /H ₂ O	14	-	$10.74^{+0.24}_{-0.22}$	-	$1388.67^{+25.05}_{-26.64}$
	N ₂ , CO : N ₂ /H ₂ O	14	-	$11.18^{+0.27}_{-0.26}$	-	$1052.87^{+21.24}_{-19.83}$

Table 4.2: *Parameter Estimates from Numerical Model Fitting of Desorption Experiments*

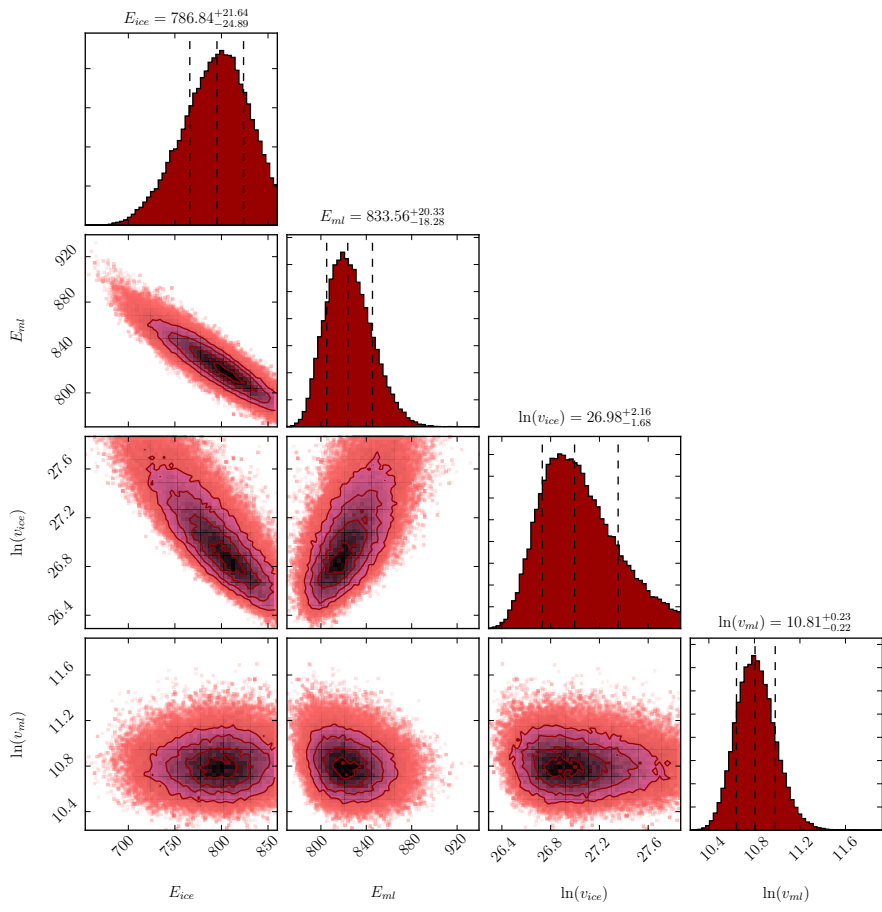


(a) Posterior Probability Distribution Projections

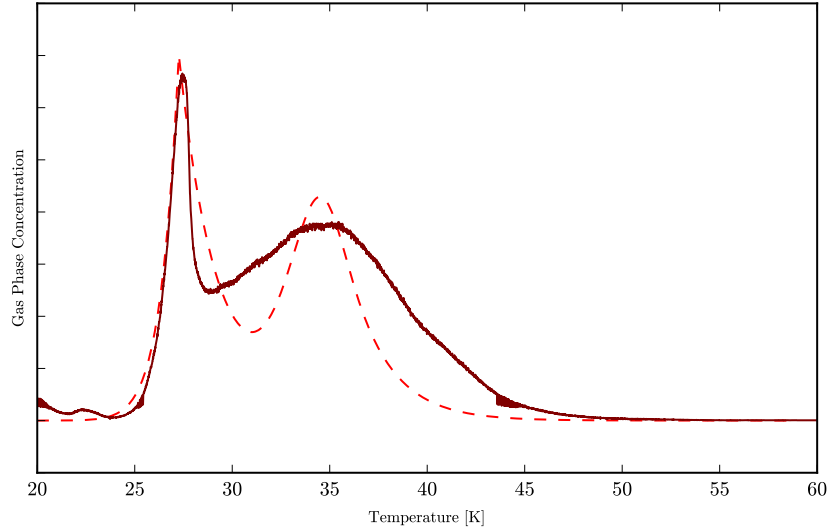


(b) Model Fit to Experimental Curve

Figure 4.2: Pure ^{13}CO Ice, Multilayer

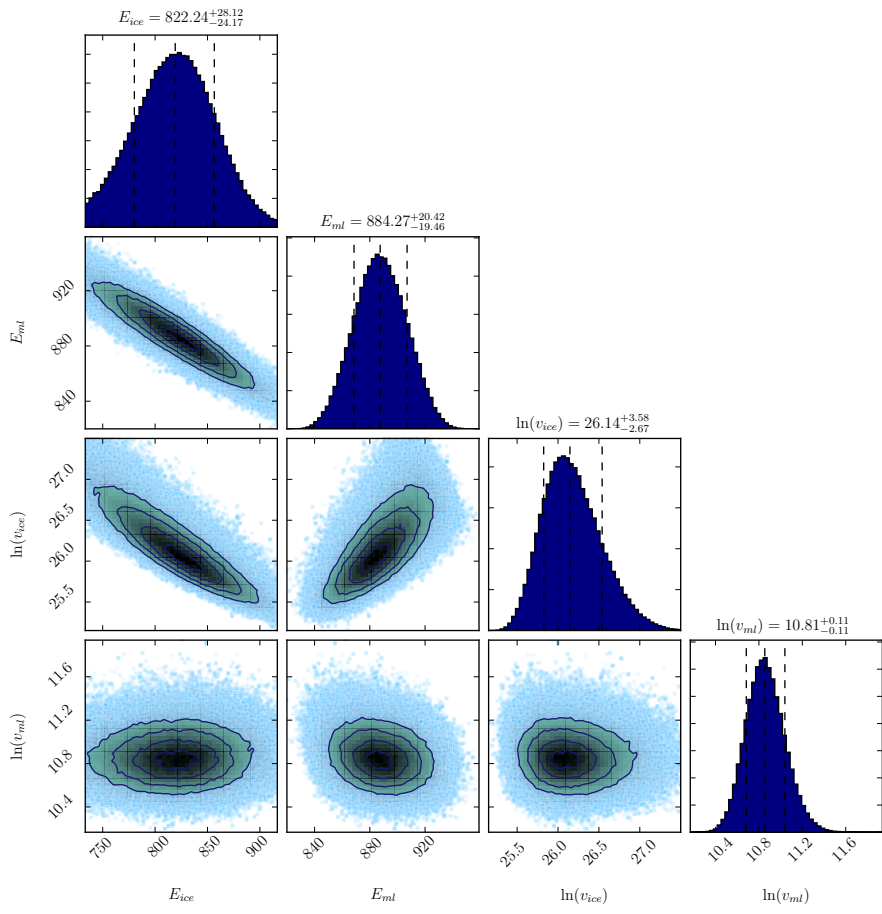


(a) Posterior Probability Distribution Projections

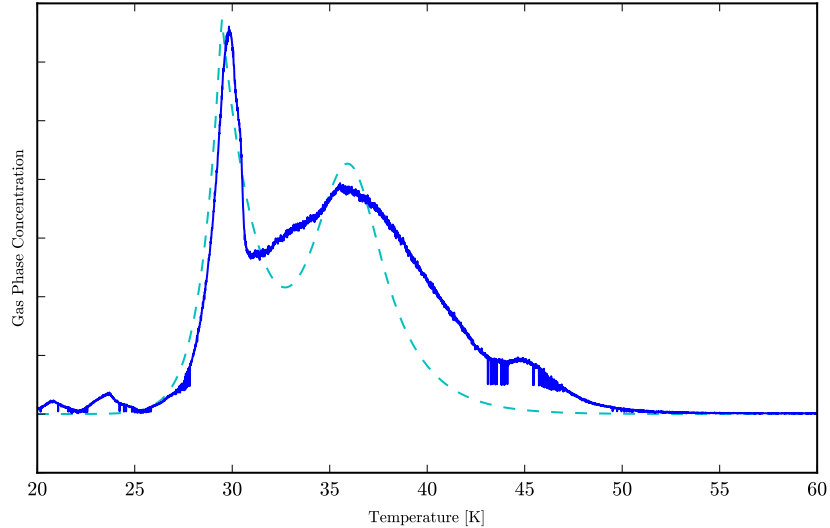


(b) Model Fit to Experimental Curve

Figure 4.3: Pure $^{15}\text{N}_2$ Ice, Multilayer

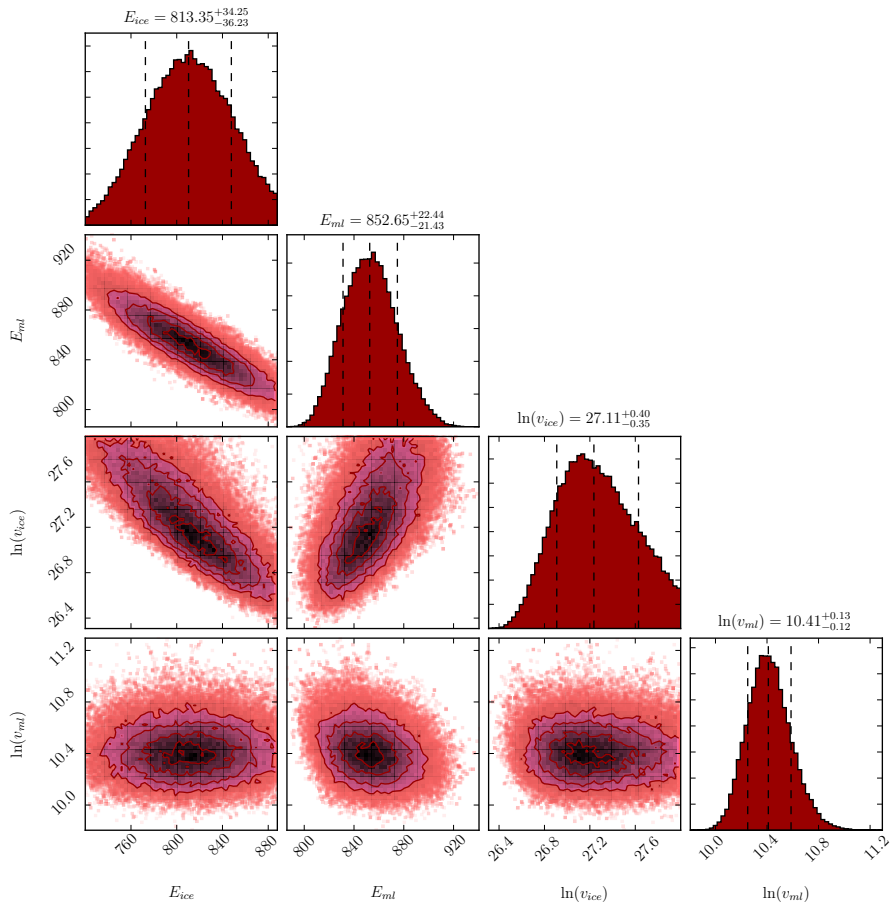


(a) Posterior Probability Distribution Projections

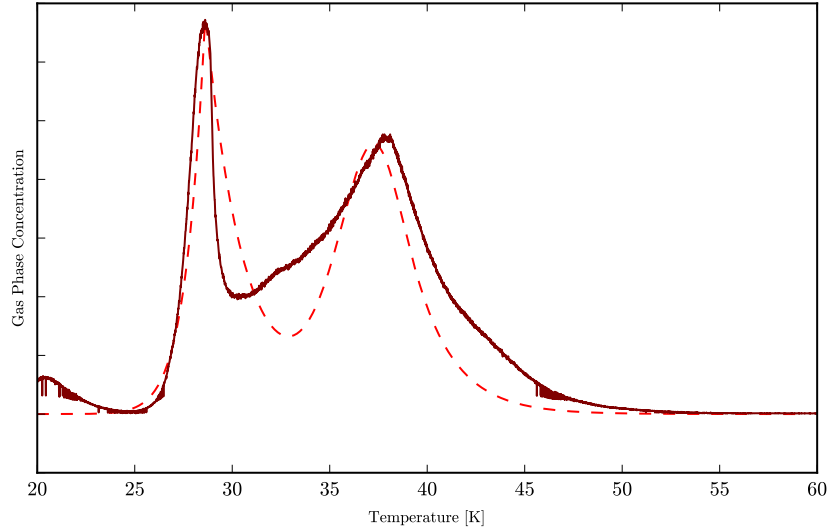


(b) Model Fit to Experimental Curve

Figure 4.4: $^{13}\text{CO}/\text{H}_2\text{O}$ Ice ($T_{dep} = 100$ K), Multilayer

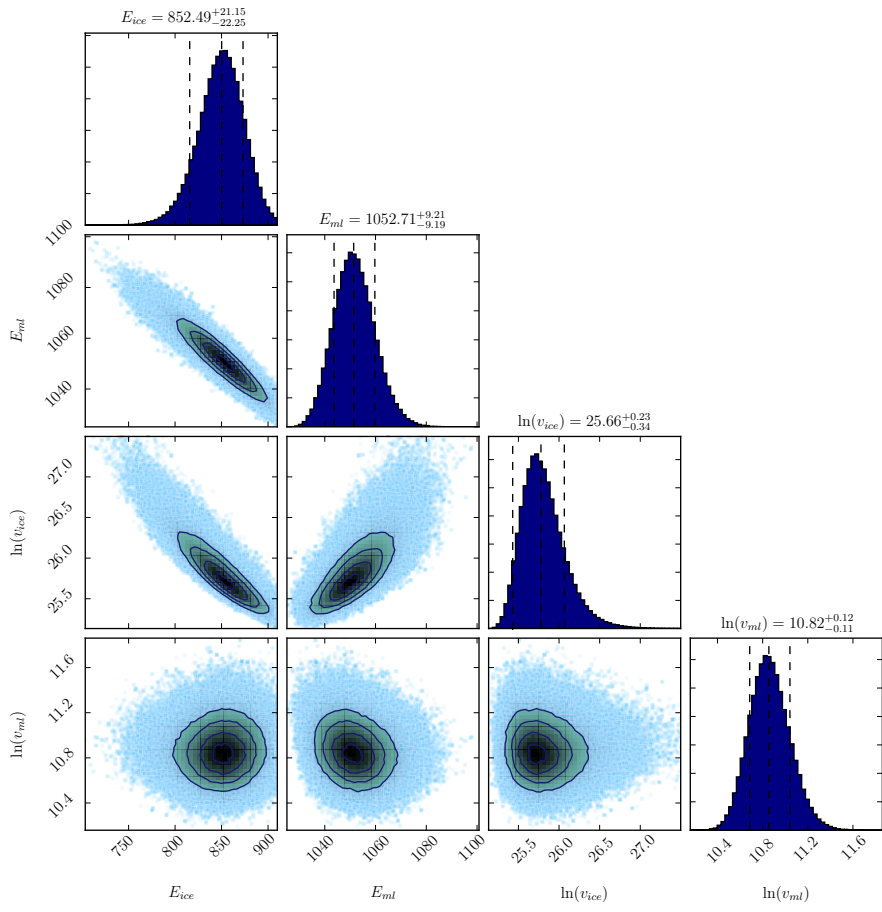


(a) Posterior Probability Distribution Projections

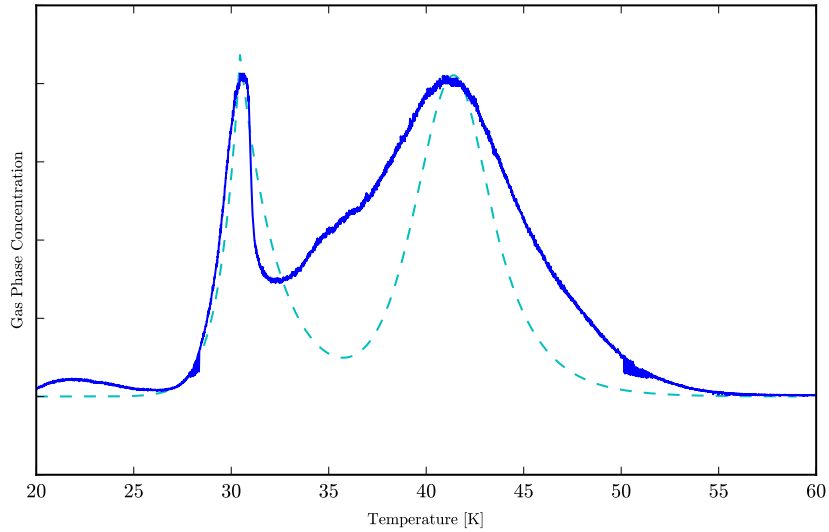


(b) Model Fit to Experimental Curve

Figure 4.5: $^{15}\text{N}_2/\text{H}_2\text{O}$ Ice ($T_{dep} = 100$ K), Multilayer

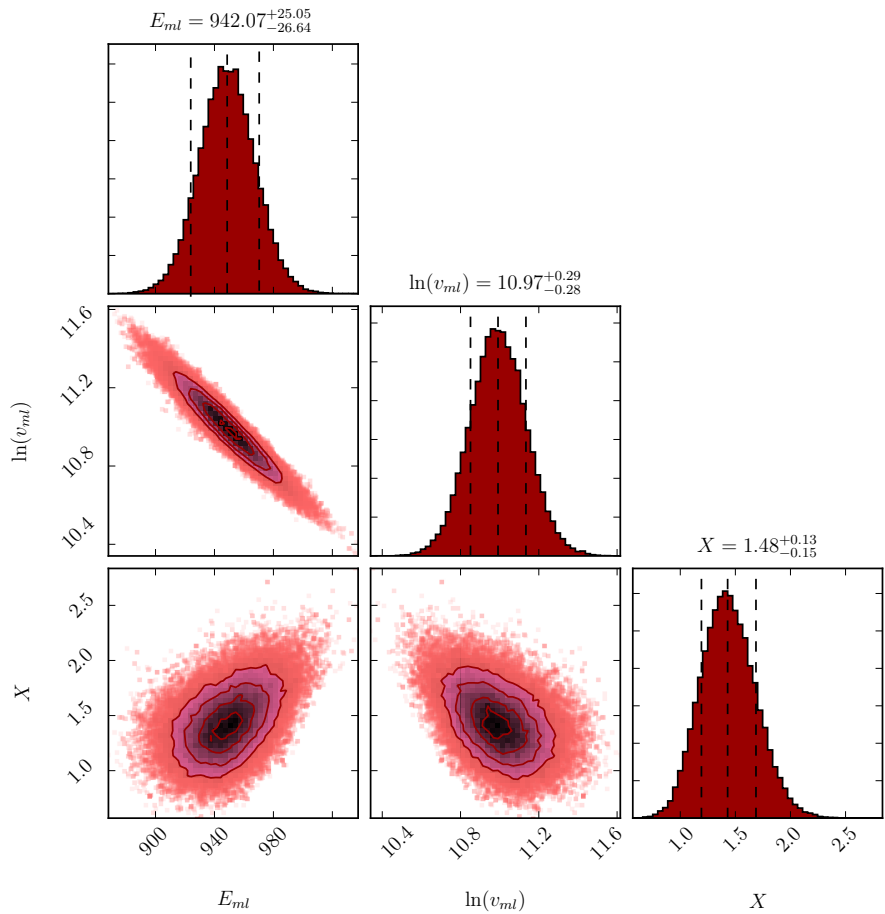


(a) Posterior Probability Distribution Projections

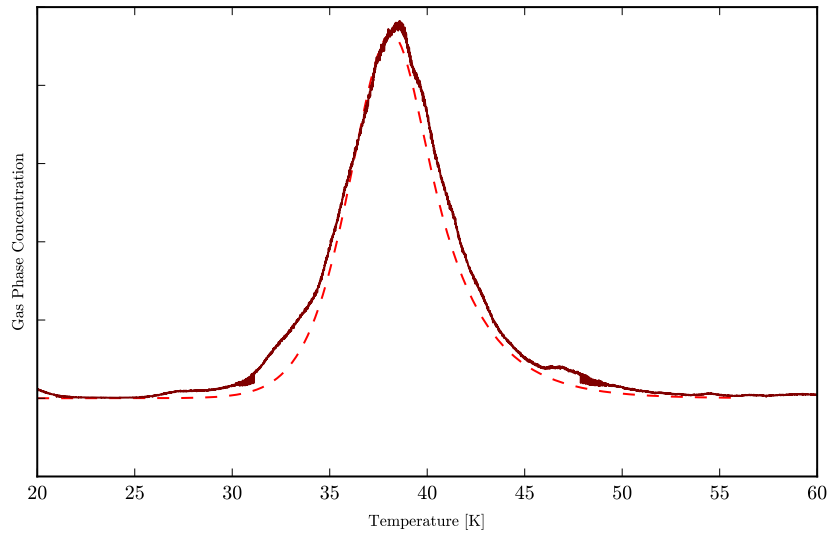


(b) Model Fit to Experimental Curve

Figure 4.6: $^{13}\text{CO}/\text{H}_2\text{O}$ Ice ($T_{dep} = 70$ K), Multilayer

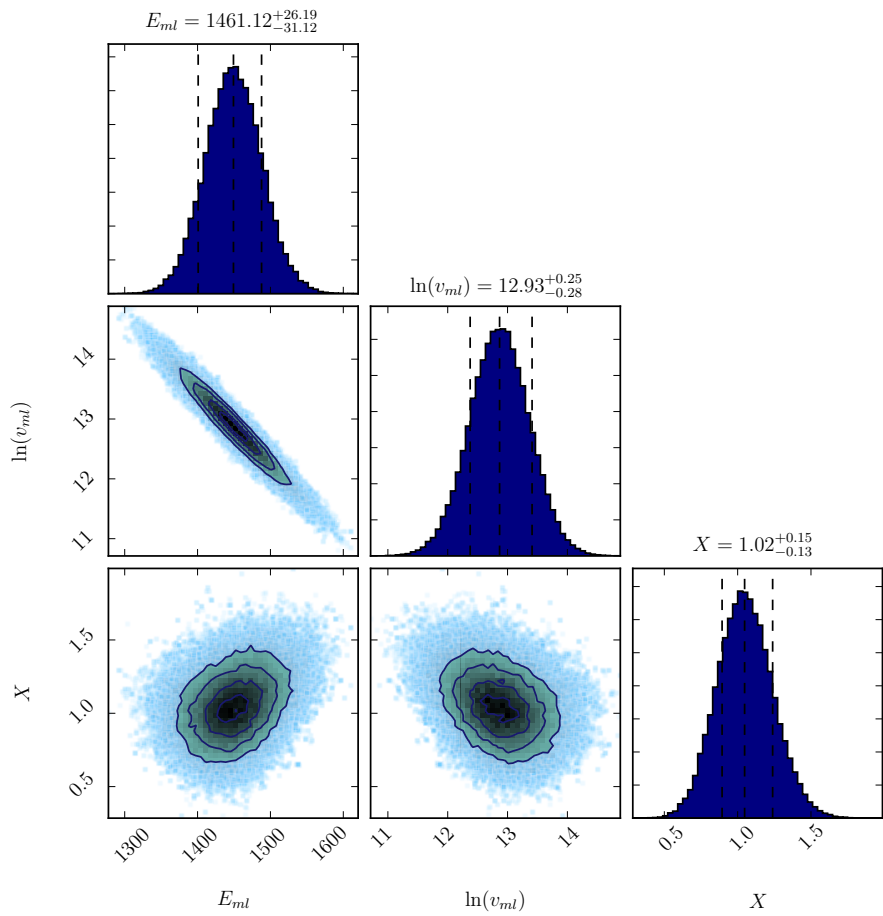


(a) Posterior Probability Distribution Projections

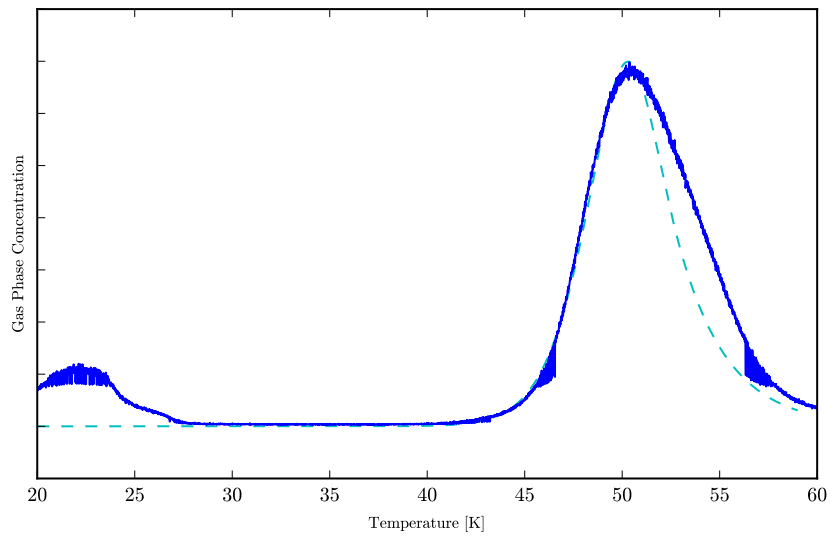


(b) Model Fit to Experimental Curve

Figure 4.7: $^{15}\text{N}_2/\text{H}_2\text{O}$ Ice ($T_{dep} = 70$ K), Monolayer

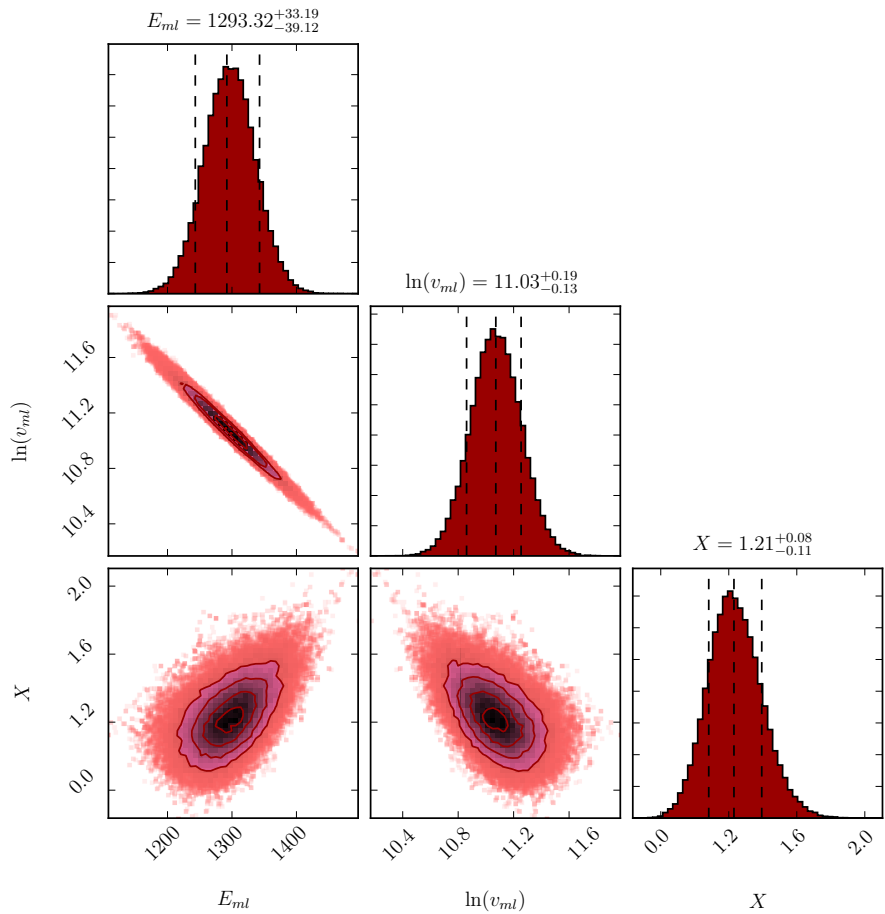


(a) Posterior Probability Distribution Projections

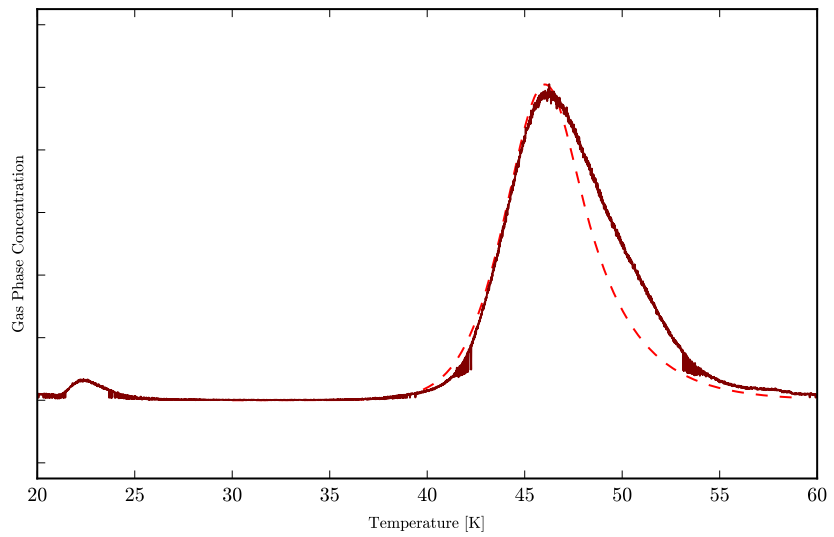


(b) Model Fit to Experimental Curve

Figure 4.8: $^{13}\text{CO}/\text{H}_2\text{O}$ Ice ($T_{dep} = 14$ K), Monolayer

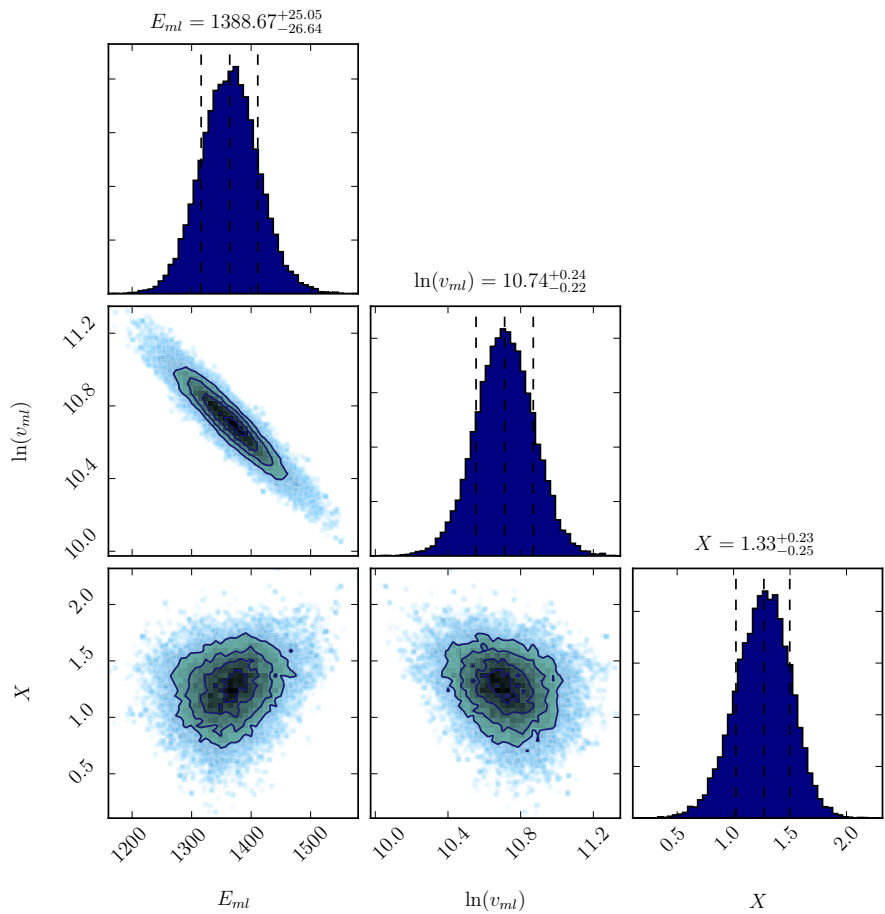


(a) Posterior Probability Distribution Projections

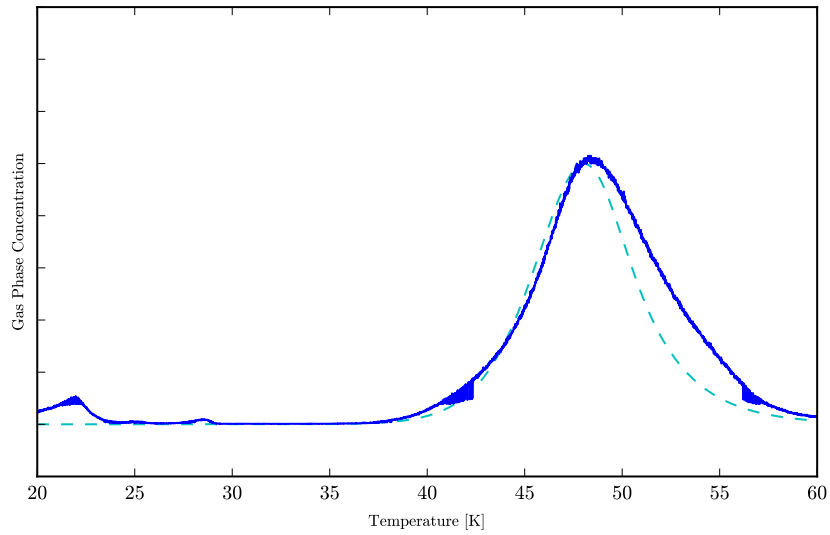


(b) Model Fit to Experimental Curve

Figure 4.9: $^{15}\text{N}_2/\text{H}_2\text{O}$ Ice ($T_{dep} = 14$ K), Monolayer

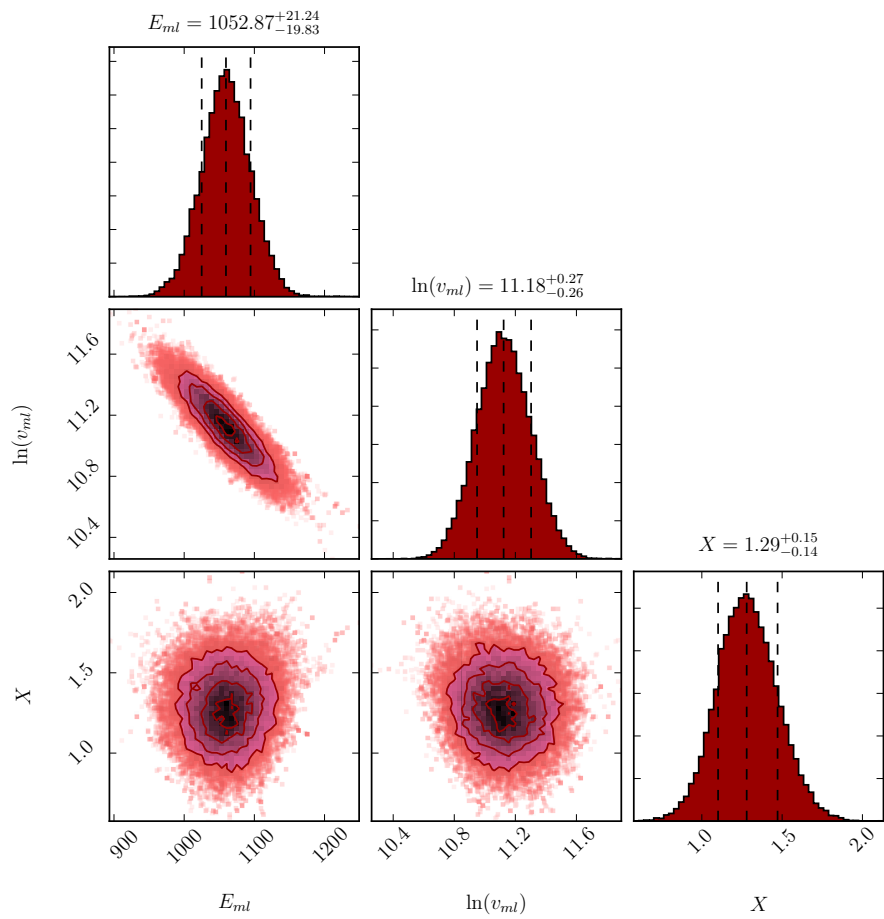


(a) Posterior Probability Distribution Projections

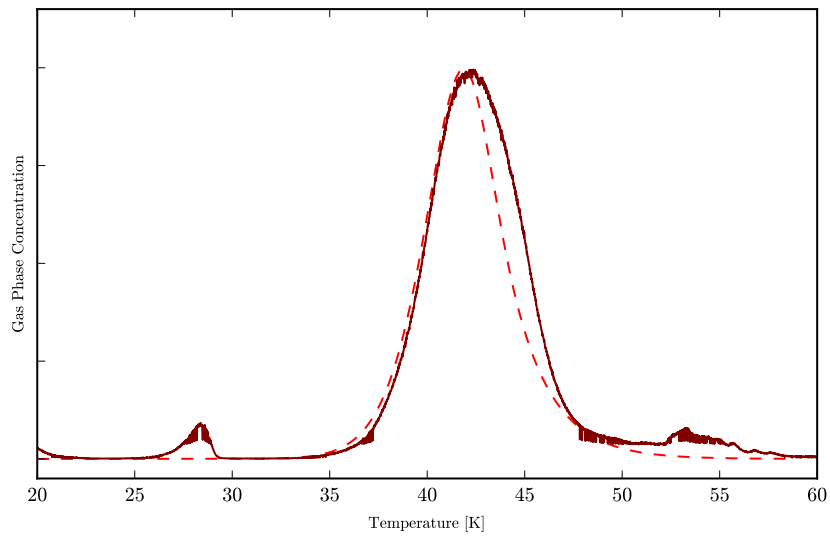


(b) Model Fit to Experimental Curve

Figure 4.10: ^{13}CO from 1 : 1 $^{13}\text{CO} : ^{15}\text{N}_2/\text{H}_2\text{O}$ Ice ($T_{dep} = 14$ K), Monolayer



(a) Posterior Probability Distribution Projections



(b) Model Fit to Experimental Curve

Figure 4.11: $^{15}\text{N}_2$ from 1 : 1 $^{13}\text{CO} : ^{15}\text{N}_2/\text{H}_2\text{O}$ Ice ($T_{dep} = 14$ K), Monolayer

4.3.1 Binding Energy Ratio Calculation

From the best-fit parameter values, we can calculate the binding energy ratio $R_B = E_{B, \text{N}_2}/E_{B, \text{CO}}$. To calculate the pure ice binding energy ratio, or $R_B = E_{B, \text{N}_2}(\text{N}_2 - \text{N}_2)/E_{B, \text{CO}}(\text{CO} - \text{CO})$, we divide the binding energies from the pure ice multilayer curves. To calculate the binding energy ratio for experiments involving H_2O ices, or $R_B = E_{B, \text{N}_2}(\text{N}_2 - \text{H}_2\text{O})/E_{B, \text{CO}}(\text{CO} - c\text{eH}_2\text{O})$, we divide the binding energies from the corresponding monolayer curves. The exact ratio values are given in Table 4.3, and plotted against literature values (Bisschop et al. 2006) in Figure 4.12.

$R_B = E_{B, \text{N}_2}/E_{B, \text{CO}}$			
Morphology	$T_{dep}, \text{H}_2\text{O}$	R_B^{ice}	R_B^{ml}
Pure ices	-	$0.999^{+0.040}_{-0.044}$	$0.951^{+0.035}_{-0.032}$
Layered ices	100	$0.989^{+0.054}_{-0.053}$	$0.964^{+0.035}_{-0.033}$
	70	-	$0.895^{+0.028}_{-0.030}$
	14	-	$0.885^{+0.031}_{-0.037}$
Mixture ices	14	-	$0.758^{+0.027}_{-0.027}$

Table 4.3: *Binding Energy Ratio between $^{15}\text{N}_2$ and ^{13}CO*

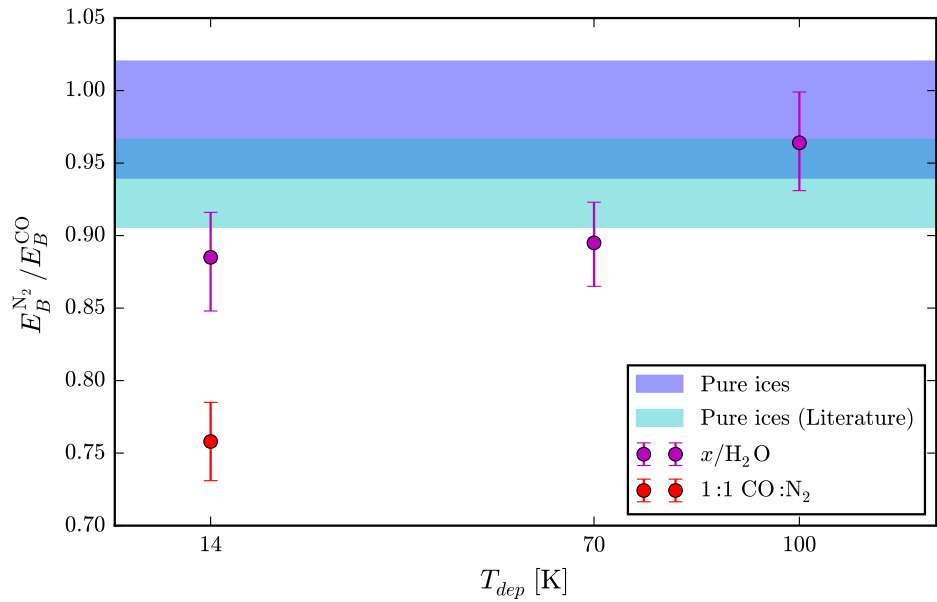


Figure 4.12: *Binding Energy Ratio:* $R_B = E_{B, N_2} / E_{B, CO}$. We plot the binding energy ratio as calculated for monolayer coverages since monolayer binding energies were available for all experiments, whereas multilayer binding energies were only available for ice samples with sufficiently high coverages.

Chapter 5

Conclusion

5.1 Binding Energy Ratio Results

From the model fitting in the previous chapter, the ratio of the binding energies between N₂ and CO, defined as $R_B = E_{B,N_2}(N_2 - H_2O)/E_{B,CO}(CO - H_2O)$, ranges from 0.758 ± 0.027 to 0.964 ± 0.035 . As discussed previously, we compare the binding energies extracted from the monolayer peak to each other in experiments involving H₂O, since these reflect the interactions of the molecules and the H₂O ice substrate, i.e. N₂ – H₂O and CO – H₂O. Additionally, we compare these monolayer binding energies from H₂O experiments with the multilayer binding energy extracted from the pure ice experiment, since the multilayers reflect the interactions of molecules with its own species, i.e. N₂ – N₂ and CO – CO.

The hypotheses proposed in Chapter 3 regarding the changes in binding energy differential over ice morphology and substrate structure are supported by the experimental data. The binding energy ratio is lowest for the 1 : 1 CO : N₂ ice mixture relative to all of the layered ice and pure ice morphologies, with $R_B = 0.758 \pm 0.027$. This suggests that H₂O does preferentially bind to CO over N₂ when both are present, possibly due to the polarity of CO while N₂ has no permanent dipole moment. This mixed ice binding energy ratio is lower than the previously reported mixed ice binding energy ratios of $R_B = 0.893 \pm 0.003$ in experiments involving pure ice mixtures, i.e. CO : N₂ not deposited over H₂O, (Öberg et al. 2005) and $R_B = 1.0$ (Bisschop et al. 2006), suggesting that the presence of H₂O increases the desorption barrier and hinders

CO desorption further.

Furthermore, we find that the binding energy differential increases with increasingly porous H₂O substrates. Since the total desorption barrier increases with the number of interactions between the molecule and the substrate, and since increasing the porosity increases the number of interaction sites (via diffusion and uneven surface structure), the total binding energy differential should be maximized in the porous H₂O scenarios when the density of binding sites is maximized. The lowest binding energy ratio, $R_B = 0.758 \pm 0.027$ was found in the case of a sub-monolayer mixed ice sample on highly porous H₂O ice deposited at 14 K.

5.2 Astrophysical Implications

5.2.1 Desorption Kinetics

To reproduce the experimental data, we constructed a four-phase chemical model of desorption behavior consisting of a zeroth-order multilayer desorption process and a first-order monolayer desorption process. This diverges from previous chemical models, particularly the three-phase family of models which does not consider the monolayer separately. We find that the four-phase model reproduces the experimental data when the multilayer and monolayer differ in reaction order.

Previous studies have considered CO desorption to be a zeroth-order process while considering N₂ desorption to be a first-order process (Bisschop et al. 2006). We do not find experimental evidence to support that the reaction order of desorption should differ *between species*, i.e. both CO and N₂ were well-fit by the same four-phase model. The only change in reaction order found in this study is between the multilayer and the monolayer, and this shift from zeroth-order to first-order kinetics occurs across both species.

5.2.2 Protoplanetary Disk Chemistry

Using the midplane temperature data of the protoplanetary disk around TW Hya (Qi et al. 2013) acquired by ALMA, we localize the CO and N₂ snowlines in this solar nebular analog, as shown in Figure 5.1. TW Hya, an $\approx 3 - 10 \times 10^6$ year old, 0.8 M_⊕ T Tauri star conforms to

solar nebular estimates, hence its circumstellar disk has been extensively studied as a template for nascent planetary systems similar to the Solar System (Andrews et al. 2012, Rosenfeld et al. 2012, Qi et al. 2013, Bergin et al. 2013). The circumstellar disk around TW Hya has been shown to be gas-rich, Kastner et al. 1997, Qi et al. 2008), and is observationally accessible due to its nearly face on inclination ($\sim 6^\circ$) and relatively close distance (54 ± 6 pc) (Qi et al. 2008, Qi et al. 2013). The use of N_2H^+ as a tracer for the CO snowline is contingent on a difference in the relative desorption behavior of the two molecules species, i.e. a binding energy ratio $R_B < 1$, enabling the abundance of N_2H^+ to increase rapidly beyond the CO snowline. However, if the binding energies of CO and N₂ are relatively similar, as found by previously laboratory studies, the use of the N_2H^+ tracer is limited as the CO and N₂ snowiness should occur at similar disk radii. The convergence of the CO and N₂ snowlines is found using the desorption peak temperatures observed in the pure ice experiments, as the CO snowline at ≈ 20 AU is only separated by ≈ 1 AU from the N₂ snowline at ≈ 21 AU. However, using the desorption peak temperatures from the CO : N₂ ice mixture on the most porous H₂O ice deposited at 14 K, we find that the extracted binding energy differential pushes apart the CO and N₂ snowlines. In the case where $R_B = 0.758 \pm 0.027$, we see that the CO snowline occurs at ≈ 7 AU, whereas the N₂ snowline is separated by ≈ 5 AU and occurs at ≈ 12 AU. The difference in desorption behavior from the binding energy differential supports the use of N_2H^+ as a tracer of the CO snowline, as N_2H^+ should trace a ring, with an inner edge at the CO snowline as its primary gas phase destroyer freezes out. As discussed in Chapter 1, snowlines are critical in understanding of radial molecular distributions throughout protoplanetary disks, which in turn constrain the elemental compositions of young planetary systems and planetesimals formed therein. Importantly, the CO snowline is particularly interesting, as it may boost planet formation in the outer ring by providing solid mass when frozen out onto grains. Furthermore, since CO is the parent molecule of many organic species, including methanol, understanding its evolution from gas phase to cold state chemistry constrains the subsequent organic distributions in young planetary systems and planetesimals.

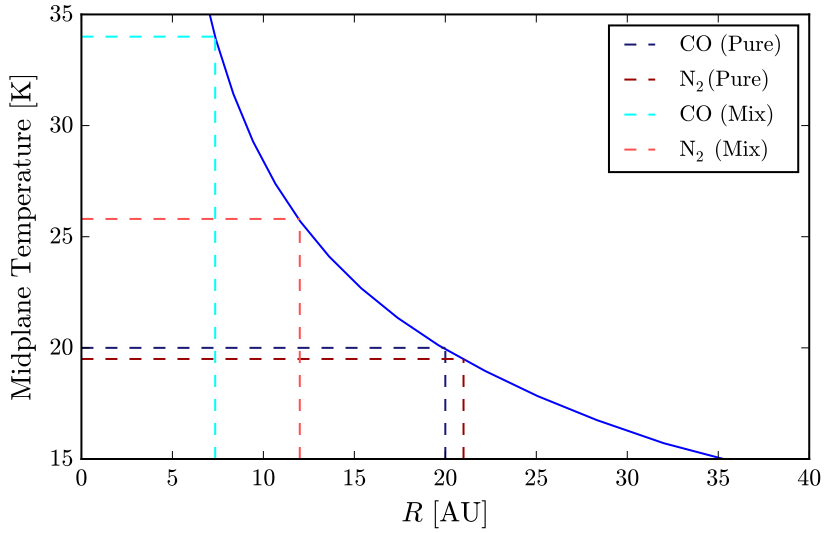


Figure 5.1: *CO and N₂ Snowlines in Tw Hya Disk:* The difference in relative desorption behavior observed in the ice mixture experiment pushes apart the CO and N₂ snowlines relative to the similar desorption behavior observed in the pure ice experiments. This divergence in snowlines supports the use of N₂H⁺ as a tracer for the CO snowline, as its abundance structure should follow a ring with an inner edge along the CO snowline and outer ring along the N₂ snowline.

5.2.3 Molecular Probes of Young Stellar and Planetary Systems

The lowest binding energy ratio of $R_B = 0.758 \pm 0.027$ represents a binding energy ratio significantly lower than existing literature ratios. As previously noted, this ratio was observed in an experimental scenario designed to maximize the binding energy differential. Before the laboratory experiments done by Öberg et al. (2005) and Bisschop et al. (2006), the binding energy ratio range was assumed to be within $R_B = 0.50 - 0.75$, but laboratory experiments tightly increased and constrained this ratio to be $R_B \geq 0.93$. Importantly, a lower bound of $R_B = 0.758 \pm 0.027$ eases the constraints on R_B and increases the range of the parameter. Consequently, the anti-correlation between N₂H⁺ and CO can be better explained with this lower bound by current disk chemistry and star formation models.

Furthermore, interstellar ices could contain contaminating molecules besides H₂O, such as methanol or other carbon compounds. However, since H₂O has a stronger dipole moment than other interstellar ice contaminants, it should bind the strongest to the polar CO relative to N₂. The effects of additional contaminants in interstellar ices should only mitigate, or decrease,

any binding energy differential between CO and N₂ since they are of weaker polarity.

5.3 Summary

In this study, new experimental data have been presented for the desorption of CO and N₂ ices on H₂O ice substrates. A four-phase ice desorption model was constructed that allows for simulation of desorption events in addition to the extraction of critical parameter values. Additionally, numerical fitting of the generative coupled differential system model to the experimental data was done via the affine invariant ensemble sampling Markov Chain Monte Carlo (MCMC) algorithm, which enabled marginalization of nuisance parameters while finding the global optimum set of best-fit parameters. The key results are as follows:

1. The ratio for the binding energies for N₂ and CO on H₂O ices, or $R_B = E_{B,N_2}(N_2 - H_2O)/E_{B,CO}(CO - H_2O)$ ranges from 0.758 ± 0.027 to 0.964 ± 0.035 .
2. A greater binding energy differential was found in mixed rather than layered or pure ice samples; and with highly porous, highly dense amorphous H₂O substrates. The lowest binding energy ratio was found in the case of a sub-monolayer ice mixture on highly porous H₂O deposited at 14 K, representing an extreme chemical context that would maximize any binding energy difference between N₂ and CO.
3. Desorption kinetics of the multilayer for both N₂ and CO was found to be zeroth-order, or independent of the surface concentration of solid state molecules. Meanwhile, desorption kinetics of the monolayer for both N₂ and CO was found to be first-order, reflecting how the number of molecules left on the surface constrains the rate of evaporation.
4. Bayesian inference methods enabled extraction of binding energies and pre-exponential factors that accurately reproduced experimental desorption events.
5. The difference in relative desorption behavior in the presence of H₂O ices would push apart the snowlines of CO and N₂H⁺ in protoplanetary disks, and was localized in the case of TW Hya. The divergence in the snowlines would support the use of N₂H⁺ as a tracer of the CO snowline in protoplanetary disks.

- The lower bound of the binding energy ratio was significantly lowered from previous laboratory experiments, increasing the range of values the parameter can take in astrochemical models. Consequently, current models will be to explain the observed anti-correlation in CO and N₂H⁺ in young stellar and planetary systems with this difference in relative desorption behavior.

In summary, these results suggest that the presence of H₂O in interstellar ices does affect the binding energy ratio between N₂ and CO. The lowest binding energy ratio observed was $R_B = E_{B,N_2}(N_2 - H_2O)/E_{B,CO}(CO - H_2O) = 0.758 \pm 0.027$. The resulting difference in desorption behavior supports the use of N₂H⁺ as a tracer of the CO snowline, and suggests that N₂ should remain in the gas phase at greater distances from the central star in protoplanetary disks. Additionally, this difference in desorption behavior suggests that N₂H⁺ could probe cold, dense regions of young stellar objects and protoplanetary disks more deeply than CO. In general, the utility of these species as chemical tracers critically depends on understanding of evolution, and the binding energy differential found in this thesis between CO and N₂ suggests that the two molecules have different desorption behavior. In turn, this implies that gas-phase and solid-state processes of CO and N₂ will be different in astrophysical environments; in particular, in star and planet forming regions.

Chapter 6

References

- Aikawa, Y., Herbst, E., Roberts, H., & Caselli, P. 2005, ApJ, 620, 330
- Aikawa, Y., Ohashi, N., & Herbst, E. 2003., ApJ. 593, 906
- Aikawa, Y., Umebayashi, T., Nakano, T., & Miyama, S.M., 1999, ApJ, 519, 705
- Alves, J., Lada, C.J., & Lada, E.A. 2001, Nature, 409, 159
- Andrews, S.M. Wilner, D.J., Espaillat, C., Hughes, A.M., Dullemond, C.P., McClure, M.K., Qi., C. & Brown, J.M. 2012, ApJ 732, 42
- Attard, G., & Barnes, C. 1998, Surfaces (Oxford: Oxford Univ. Press)
- Belloche, A., & Andre, P. 2004. A&A, 419, L35
- Bergin, E.A., Alves, J., Huard, T., & Lada, C.J. 2002, ApJ, 570, L101
- Bergin, E.A., Ciardi, D.R. Lada, C.J. Alves., & Lada, C.J. 2002, ApJ, 570, L101
- Bergin, E. A., & Langer, W.D., 1997, ApJ, 486, 316
- Bergin, E. A., Langer, W.D., & Goldsmith, P.F. 1995, ApJ, 441, 222
- Bisschop, S.E., Fraser, H.J., Öberg, K.I., van Dischoeck, E.F., & Schlemmer, S. 2005, A&A, 449, 1297.
- Bolina, A.S., Wolff, A.J., & Brown, W.A. 2005, J. Chem. Phys., 122, 4713
- Bouwman, J., Ludwig, W., Awad, Z., et al 2007, A&A, 476, 995
- Caselli, P., Walmsley, C.M., Tafalla, M., Dore, L., & Myers, P.C. 1999, ApJ, 523, L165
- Ceccarelli, C., & Dominik, C., 2005, A&A, 440, 583

- Collings, M.P., Dever, J.W., Fraser, H.J., & McCoustra, M.R.S. 2003, Ap&SS, 285, 633
- Collings, M.P., Anderson, M.A., Chen, R., et al. 2004, MNRAS, 354, 1133.
- Crovisier, J. 1998. Faraday 109, 437.
- Fayolle., E.C., Öberg, K.I., Cuppen, H.M., Visser, R., & Linnartz., H. 2011, A&A, 529, A74
- Foreman-Mackey, D., Hogg, D.W., Lang, D., Goodman, J., 2012. emcee: The MCMC Hammer.
- Fraser, H.J., Collings, M.P., Dever, J.W., & McCoustra, M.R.S. 2004, MNRAS, 327, 1165.
- Fraser, H.J., & van Dishoeck, E.F. 2004, ApJ, 609, 459
- Gerakines, P.A., Schutte, W. A., Greenberg, J.M., & van Dishoeck, E.F. 1995, A&A, 296, 810
- Goodman, J., & Weare, J., 2010. Comm. App. Math. Comp. Sci. 5, 65
- Hasegawa, T.I., & Herbst, E., 1993, MNRAS, 263, 589
- Hasegawa, T.I., Herbst, E., & Leung, C.M. 1992, ApJS, 82, 167
- Hastings, W.K., 1970. Biometrika 57, 97
- Jenniskens, P., & Blake, D.F. 1994, Science, 265, 753
- Jenniskens, P., Blake, D.R., Wilson, M.A., & Pohorille, A. 1995, ApJ, 455, 389
- Smith, R.S., Huang, C., Wong, E.K.L. & Kay, B.D. 1997, Phys. Rev. Lett., 79, 909
- Jørgensen, J.K. 2004, A&A, 424, 589
- Jørgensen , J.K., Hogerheijde, M.R., van Dishoeck, E.F., Black, G.A., & Schöier, F.L. 2004, A&A, 413, 993
- Jørgensen, J.K., Schöier, F.L., & van Dishoeck, E.F. 2005, A&A, 435, 177
- Lacy, J.H., Knacke, R., Geballe, T.R., & Tokunaga, A. T. 1994, ApJ, 428, L69.
- Lauck, T., Karseemeijer, L., Shulenberger, K., Rajappan, M., Öberg, K.I., & Cuppen, H.M. 2015, ApJ in press.
- MacKay, D., 2003. Information theory, inference, and learning algorithms. (3rd ed: Cambridge Univ. Press)
- Maret, S., Bergin, E.A., & Lada, C.J. 2006, Nature Lett., 442, 27
- Maret, S., Bergin, E.A., & Tafalla, M., 2013, A&A, 235, 214
- Menzel, D. 1982, Chemistry and Physics and Solid Surfaces IV, ed. R. Vanselow & R. Howe (Spring-Verlag), 389

- Öberg, K.I., van Broekhuizen, F., Fraser, H.J., et al. 2005, ApJ, 621, L33
- Metropolis, N., Rosenbluth, A.W., Teller, A.H., & Teller, E. 1953. J. Chem. Phys. 21, 1087
- Mumma, M.J., & Charnley, S.B. 2011, ARA&A, 46, 471.
- Pontoppidan, K.M., Fraser, H.J., Dartois, E., et al. 2003, A&A, 408, 981
- Pontoppidan, K.M., Dullemond, C.P., van Dishoeck, E.F., et al. 2005, ApJ, 622, 463
- Qi., C., Wilner, D.J., Aikawa, Y., Blake, G.A., Melnick, G.J., 2009, ApJ, 690, 1497
- Qi, C., Öberg, K.I., & Wilner, D.J. 2013, ApJ, 765, 34
- Qi, C., Öberg, K.I., Wilner, D.J., d'Alessio, P., Bergin, E., Andrews, S.M., Blake, G., Hogerheijde, M.R., van Dishoeck, E.F. 2013. Science, 2013, 341, 6146, 630
- Rosenfeld, K.A., Qi., C., Andrews, S.M., Wilner, D.J., Corder, S.A., Dullemond, C.P., Lin, S-Y., Hughes, A.M., d'Alessio, P., & Ho, P.T.P. 2012, ApJ 757, 129
- Sadlej, J., Rowland, B., Devlin, J.P., & Bich, V. 1995. J. Chem. Phys., 102, 4804
- van Dishoeck, E.F., Phillips, T.G., Keene, J., & Blake, G.A. 1992, A&A, 261, L13.
- Woodruff, D.P., & Delchar, T.A. 1994, Modern Techniques of Surface Science (2nd ed: Cambridge Univ. Press), chap. 9